UNIVERSITY OF OKLAHOMA

GRADUATE COLLEGE

BUOYANCY EFFECTS ON FLOW STRUCTURE AND INSTABILITY OF LOW-DENSITY GAS JETS

A Dissertation

SUBMITTED TO THE GRADUATE FACULTY

in partial fulfillment of the requirements for the

degree of

Doctor of Philosophy

By

Kasyap Sriramachandra Pasumarthi
Norman, Oklahoma
2004

Downloaded from SHAREOK. Persistent Handle URL: https://hdl.handle.net/11244/754

UMI Number: 3135693

INFORMATION TO USERS

The quality of this reproduction is dependent upon the quality of the copy submitted. Broken or indistinct print, colored or poor quality illustrations and photographs, print bleed-through, substandard margins, and improper alignment can adversely affect reproduction.

In the unlikely event that the author did not send a complete manuscript and there are missing pages, these will be noted. Also, if unauthorized copyright material had to be removed, a note will indicate the deletion.

UMI®

UMI Microform 3135693

Copyright 2004 by ProQuest Information and Learning Company.

All rights reserved. This microform edition is protected against unauthorized copying under Title 17, United States Code.

ProQuest Information and Learning Company
300 North Zeeb Road
P.O. Box 1346
Ann Arbor, MI 48106-1346

©Copyright by Kasyap Sriramachandra Pasumarthi 2004
All Rights Reserved

BUOYANCY EFFECTS ON FLOW STRUCTURE
AND INSTABILITY OF LOW-DENSITY GAS JETS

A DISSERTATION APPROVED FOR THE
SCHOOL OF AEROSPACE AND MECHANICAL ENGINEERING

BY

Dr. R. N. Parthasarathy (Co-Chair)

Dr. A. K. Agrawal (Co-Chair)

Dr. S. R. Gollahalli (Member)

Dr. F. C. Lai (Member)

Dr. D. V. Papavassiliou (Member)

ACKNOWLEDGEMENTS

The author wishes to thank his parents, Narasimha Rao and Subbalakshmi, for their unwavering love, blessings and support, to thank his sister Santhi for her encouragement and affection. The author wishes to thank all his friends and well wishers for their encouragement in every walk of his life.

It is with deep gratitude and sincere appreciation that the author acknowledges the tremendous guidance, patience, inspiration and understanding of his advisors, Dr. Ajay Agrawal and Dr. Ramkumar Parthasarathy. The author wishes to record his gratitude to other members of the graduate committee Dr. Gollahalli, Dr. Lai and Dr. Papavassiliou for their patience, understanding and suggestions during this research. The author wishes to thank Dr. DeVon Griffin of NASA Glenn Research Center for his encouragement and direction. The author owes a deep sense of gratitude to the kind staff of School of AME and AME machine shop.

Finally, the author wishes to thank his wife Akila for her patience, sacrifice and great support throughout this work.

Table of Contents

LIST OF TABLES viii

LIST OF FIGURES ix

NOMENCLATURE xv

ABSTRACT xviii

CHAPTER 1: INTRODUCTION 1

1.1 Background 1

1.2 Literature Review 2

1.2.1 Experimental Studies in Laminar Flow Regime 3

1.2.2 Experimental Studies in Transitional Flow Regime 8

1.2.3 Computational Studies 9

1.2.4 Stability Analysis 10

1.3 Objectives 17

CHAPTER 2: EXPERIMENTAL METHOD 20

2.1 Experimental Setup 20

2.1.1 Test Rig 20

2.1.2 Flow System 21

2.1.3 Quantitative Rainbow Schlieren Deflectometry 22

2.1.4 Image Acquisition 23

2.2 Test Procedure 24

2.2.1 Drop Tower 24

2.2.2 Drop Procedure 24

2.3 Rainbow Schlieren Analysis 26

2.4 Image Processing 30

2.4.1 Time Dependent Technique 31

2.4.1.1 Frequency Spectrum 31

2.4.1.2 Temporal Evolution 31

2.5 Uncertainty Analysis 32

CHAPTER 3: NUMERICAL PROCEDURE 43

3.1 Governing Equations 43

3.2 Model Formulation 45

3.3 Flow Formulation 45
3.4 Solution Procedure 46
CHAPTER 4: EXPERIMENTAL RESULTS 48
4.1 Buoyancy-Dominated Flow Regime 48
4.1.1 Rainbow Schlieren Visualization 49
4.1.2 Time-Resolved Concentration Distributions 50
4.1.3 Vortex Structure and Evolution 53
4.1.4 Oscillating Flow Characteristics 55
4.1.5 Effects of Richardson Number 57
4.1.6 Summary 59
4.2 Buoyancy effects in the near field laminar region of low density jets 80
4.2.1 Schlieren Visualization 80
4.2.2 Temporal Evolution 82
4.2.3 Power Spectra 84
4.2.4 Peak Power Plots 87
4.2.5 Summary 89
4.3 Buoyancy effects in the transitional region of low density jets 115
4.3.1 Flow Visualization 115
4.3.2 Space-Time Images 116
4.3.3 Oscillating Flow Characteristics 116
CHAPTER 5: LINEAR STABILITY ANALYSIS 122
5.1 Theory 122
5.2 Formulation 122
5.3 Method of Solution 130
5.4 Results of Stability Analysis 133
5.4.1 Temporal stability analysis 134
5.4.1.1 Effect of density ratio 134
5.4.1.2 Effect of buoyancy 135
5.4.2 Absolute stability analysis 136
5.4.2.1 Effect of density ratio 137
5.4.2.2 Effect of buoyancy 138

5.5 Comparison with experimental data 138
CHAPTER 6: CONCLUSIONS 155
CHAPTER 7: RECOMMENDATIONS 157
REFERENCES 158
APPENDIX A: EXPERIMENTAL DATA 164
APPENDIX B: UNCERTAINTY ANALYSIS 165
APPENDIX C: PLC LADDER LOGIC PROGRAM 168

LIST OF TABLES

TABLE		PAGE
4.1	Experimental test matrix	61

LIST OF FIGURES

FIGURE		PAGE
1.1	Rainbow schlieren images of helium jet for (a) Re = 1500, Ri = 0.002, (b) Re = 800, Ri = 0.02, (c)Re = 200, Ri = 0.72.	19
2.1	A photograph of the experimental test rig.	34
2.2	Optical layout	35
2.3	A cutaway drawing of the 2.2s Drop Tower, showing the levels on which an experiment package is prepared for drop, released and captured.	36
2.4	A photograph of the vertical shaft of the drop tower.	37
2.5	The air shield being suspended by drop-release mechanism	38
2.6	The air shield with the rig after the drop process	39
2.7	Rainbow color filter	40
2.8	Filter calibration curve	41
2.9	A sample space-time image	42
3.1	Computational domain of the numerical model of helium jet ejecting vertically into ambient air.	47
4.1	Rainbow schlieren images during an oscillation cycle (Case I).	62
4.2	Contours of helium mole percentage during an oscillation cycle (Case I).	63
4.3	Contours of helium mole percentage during an oscillation cycle (Computational case, Case I).	64
4.4	Contours of vorticity during an oscillation cycle (Computational case, Case I).	65
4.5	Contours of velocity magnitude during an oscillation cycle (Computational case, Case I).	66
4.6	Schematic of the vortex and a typical helium concentration profile.	67

4.7	Profiles of helium mole percentage in the vortex region at t=16.7ms.	68
4.8	Profiles of helium mole percentage at the mid-radial plane of the vortex.	69
4.9	Radial profiles of helium mole percentage at the mid-axial plane of the vortex.	70
4.10	The shape and evolutionary path of the vortex.	71
4.11	Variation of vortex (Trailing edge) convection velocity with axial coordinate (Case I).	72
4.12	Mean and RMS helium mole percentage profiles at various axial locations (Case I).	73
4.13	Temporal evolution of helium mole percentage at various axial locations; z/d=0.05, (2) z/d=0.2, (3) z/d=0.6, and (4) z/d=1.0.	74
4.14	Temporal evolution of helium mole percentage at various axial locations; z/d=0.05, (2) z/d=0.2, (3) z/d=0.6, and (4) z/d=1.0.	75
4.15	Variation of concentration wave velocity with axial coordinate	76
4.16	Contours of helium mole percentage during an oscillation cycle (Case II).	77
4.17	Variation of vortex convection velocity with axial coordinate (Case II).	78
4.18	Mean and RMS helium mole percentage profiles at various axial locations (Case II).	79
4.19	Rainbow schlieren images in Earth gravity (left) and microgravity (right) for, (a) Re = 200, Ri = 0.72 (bottom), (b) Re = 800, Ri = 0.05 (top).	90
4.20	Instantaneous helium mole percentage contours in Earth gravity and microgravity for, (1) Re = 200, Ri = 0.72 (bottom) and (2) Re = 800, Ri = 0.05 (top) at (a) T = -0.1s, (b) T = 0.1s, (c) T= 1.1s, (d) T = 2.1s. T= 0.0s denotes the initiation of microgravity.	91
4.21	Change from Earth gravity to microgravity for varying Ri at z/d = 1.0 for, (a) Re = 200, Ri = 0.72, (b) Re = 800, Ri = 0.18, (c) Re =1200, Ri = 0.03 and (d) Re = 800, Ri = 0.008.T= 0.0s denotes the initiation of microgravity.	92

4.22 Change from Earth gravity to microgravity for varying Ri at z/d = 2.0 for, (a) Re = 200, Ri = 0.72, (b) Re = 800, Ri = 0.18, (c) Re =1200, Ri = 0.03 and (d) Re = 800, Ri = 0.008. T= 0.0s denotes the initiation of microgravity. 93

4.23 Temporal evolution of the helium mole percentage in Earth gravity (bottom) and microgravity (top) at z/d = 0.5 for, (a) Re = 200, Ri = 0.72, (b) Re = 800, Ri = 0.05, (c) Re =600, Ri = 0.04 and (d) Re = 1200, Ri = 0.008. T= 0.0s denotes the initiation of microgravity. 94

4.24 Temporal evolution of the helium mole percentage in Earth gravity (bottom) and microgravity (top) at z/d = 1.0 for, (a) Re = 200, Ri = 0.72, (b) Re = 800, Ri = 0.05, (c) Re =600, Ri = 0.04 and (d) Re = 1200, Ri = 0.008. T= 0.0s denotes the initiation of microgravity. 95

4.25 Temporal evolution of the helium mole percentage in Earth gravity (bottom) and microgravity (top) at z/d = 2.0 for, (a) Re = 200, Ri = 0.72, (b) Re = 800, Ri = 0.05, (c) Re =600, Ri = 0.04 and (d) Re = 1200, Ri = 0.008. T= 0.0s denotes the initiation of microgravity. 96

4.26 Temporal evolution of the helium mole percentage in Earth gravity (left) and microgravity (right) at z/d = 0.5 for different Ri at (1) r/d = 0.3, (2) r/d =0.5, (3) r/d = 0.6 for, (a) Re = 200, Ri = 0.72, (b) Re = 800, Ri = 0.05, (c) Re =600, Ri = 0.04 and (d) Re = 800, Ri = 0.008. T= 0.0s denotes the initiation of microgravity. 97

4.27 Temporal evolution of the helium mole percentage in Earth gravity (left) and microgravity (right) at z/d = 1.0 for different Ri at (1) r/d = 0.3, (2) r/d =0.5, (3) r/d = 0.6 for, (a) Re = 200, Ri = 0.72, (b) Re = 800, Ri = 0.05, (c) Re =600, Ri = 0.04 and (d) Re = 800, Ri = 0.008. T= 0.0s denotes the initiation of microgravity. 98

4.28 Temporal evolution of the helium mole percentage in Earth gravity (left) and microgravity (right) at z/d = 2.0 for different Ri at (1) r/d = 0.3, (2) r/d =0.5, (3) r/d = 0.6 for, (a) Re = 200, Ri = 0.72, (b) Re = 800, Ri = 0.05, (c) Re =600, Ri = 0.04 and (d) Re = 800, Ri = 0.008. T= 0.0s denotes the initiation of microgravity. 99

4.29 Power spectra for various locations throughout the flow field in Earth gravity (left) and microgravity (right) for Re = 200, Ri = 0.72 at (a) z/d = 0.02, r/d = 0.1 (b) z/d = 1.0, r/d = 0.3, (c) z/d = 1.5, r/d = 0.4 and (d) z/d = 2.0, r/d = 0.5. 100

4.30 Evolution of power spectra with Richardson number in Earth gravity (left) and microgravity (right) for, (a) Re = 200, Ri = 0.72, r/d = 0.47,

(b) Re = 400, Ri = 0.18, r/d = 0.53, (c) Re = 600, Ri = 0.08, r/d = 0.57 and (d) Re = 800, Ri = 0.05, r/d = 0.59. 101

4.31 Evolution of power spectra with Richardson number in Earth gravity (left) and microgravity (right) at z/d = 0.5 for, (a) Re = 600, Ri = 0.04, r/d = 0.64, (b) Re =800, Ri = 0.02, r/d = 0.54, (c) Re = 1000, Ri = 0.02, r/d = 0.6 and (d) Re = 1200, Ri = 0.008, r/d = 0.5. 102

4.32 Evolution of power spectra with Richardson number in Earth gravity (left) and microgravity (right) at z/d = 1.5 for, (a) Re = 600, Ri = 0.04, r/d = 0.64, (b) Re =800, Ri = 0.02, r/d = 0.54, (c) Re = 1000, Ri = 0.02, r/d = 0.6 and (d) Re = 1200, Ri = 0.008, r/d = 0.5. 103

4.33 Evolution of power spectra with Richardson number in Earth gravity (left) and microgravity (right) for, (a) Re = 800, Ri = 0.008, r/d = 0.53, (b) Re =1000, Ri = 0.005, r/d = 0.49, (c) Re = 1200, Ri = 0.003, r/d = 0.53 and (d) Re = 1500, Ri = 0.002, r/d = 0.56. 104

4.34 Spatial evolution of power spectra in the jet shear layer (r/d = 0.52) in Earth gravity (left) and microgravity (right), Re = 800, Ri = 0.008 at (a) z/d = 0.5, (b) z/d =1.0, (c) z/d = 1.5 and (d) z/d = 1.7. 105

4.35 Spatial evolution of power spectra in the jet shear layer (r/d = 0.52) in Earth gravity (left) and microgravity (right), Re = 1200, Ri = 0.003 at (a) z/d = 0.5, (b) z/d =1.0, (c) z/d = 1.5 and (d) z/d = 1.7. 106

4.36 Spatial evolution of power spectra in the jet shear layer (r/d = 0.52) in Earth gravity (left) and microgravity (right), Re = 1500, Ri = 0.002 at (a) z/d = 0.5, (b) z/d =1.0, (c) z/d = 1.5 and (d) z/d = 1.7. 107

4.37 Peak power plots (Logscales) for varying Richardson number in Earth gravity and microgravity, d = 19.05mm at (1) Earth gravity (T=-0.1s), (2) Microgravity (T=1.1-1.35s), (3) Microgravity (T=1.9-2.15s) for, (a) Re = 200, Ri = 0.72, (b) Re =400, Ri = 0.18, (c) Re = 600, Ri = 0.08 and (d) Re = 800, Ri = 0.05. 108

4.38 Peak power plots (Logscales) for varying Richardson number in Earth gravity and microgravity, d = 19.05mm at (1) Earth gravity (T=-0.1s), (2) Microgravity (T=1.1-1.35s), (3) Microgravity (T=1.9-2.15s) for, (a) Re = 200, Ri = 0.72, (b) Re =400, Ri = 0.18, (c) Re = 600, Ri = 0.08 and (d) Re = 800, Ri = 0.05. 109

4.39 Peak power (Logscales) plots for varying Richardson number in Earth gravity and microgravity, at (1) Earth gravity (T=-0.1s), (2) Microgravity (T=1.1-1.35s), (3) Microgravity (T=1.9-2.15s) for, (a) Re = 600, Ri = 0.04, (b) Re =800, Ri = 0.02, (c) Re = 1000, Ri = 0.02

and (d) Re = 1200, Ri = 0.008. 110

4.40 Peak power (Logscales) plots for varying Richardson number in Earth gravity and microgravity, at (1) Earth gravity (T=-0.1s), (2) Microgravity (T=1.1-1.35s), (3) Microgravity (T=1.9-2.15s) for, (a) Re = 600, Ri = 0.04, (b) Re =800, Ri = 0.02, (c) Re = 1000, Ri = 0.02 and (d) Re = 1200, Ri = 0.008. 111

4.41 Peak power plots for varying Richardson number in Earth gravity and microgravity, at (1) Earth gravity (T=-0.1s), (2) Microgravity (T=1.1-1.35s), (3) Microgravity (T=1.9-2.15s) for, (a) Re = 800, Ri = 0.008, (b) Re = 1000, Ri = 0.005, (c) Re =1200, Ri = 0.003 and (d) Re = 1500, Ri = 0.002. 112

4.42 Peak power plots for varying Richardson number in Earth gravity and microgravity, at (1) Earth gravity (T=-0.1s), (2) Microgravity (T=1.1-1.35s), (3) Microgravity (T=1.9-2.15s) for, (a) Re = 800, Ri = 0.008, (b) Re = 1000, Ri = 0.005, (c) Re =1200, Ri = 0.003 and (d) Re = 1500, Ri = 0.002. 113

4.43 Spatial evolution of peak power in Earth gravity and microgravity, Re = 1500, Ri = 0.002 at (a) z/d = 0.5, (b) z/d = 1.0, (c) z/d = 1.5, (d) z/d = 1.7 for (1) Earth gravity (T=-0.1s), (2) Microgravity (T=1.1-1.35s) and (3) Microgravity (T=1.9-2.15s). 114

4.44 Rainbow schlieren images in Earth gravity (left) and microgravity (right) 1(a)-(b): Case 1 (Ri=0.02); 2(a)-(b): Case 2 (Ri=0.008). 119

4.45 Spatio-temporal images in Earth gravity (left) and microgravity (right).1(a)-(b):Case1 (Ri=0.02), z/d=4.4; 2(a)-(b): Case 2, z/d=5.4 (Ri=0.008). 120

4.46 Power spectra of angular deflection data in Earth gravity (left) and microgravity (right) for r/d=0.5. 1-2: Case 1 (Ri=0.02); 3-4: Case 2 (Ri=0.008). 121

5.1 Non-dimensionalized basic jet velocity profile for S = 1 at x/2R = 1.0 and 2.67. 140

5.2 Non-dimensionalized basic jet density profiles for S = 0.14 at different axial locations. 141

5.3 Comparison of experimental and assumed hyper-tan density profiles at z/d = 2.0. 142

5.4 Variation of temporal growth rate Ω_i with wave number k for

different density ratios at x/2R = 1, Fr = 10. 143

5.5 Variation of temporal growth rate Ω_i with wave number k for different density ratios at x/2R = 1, Fr $\rightarrow\infty$. 144

5.6 Variation of temporal growth rate Ω_i with wave number k for different density ratios at x/2R = 2.67, Fr = 10. 145

5.7 Variation of temporal growth rate Ω_i with wave number k for different density ratios at x/2R = 2.67, Fr $\rightarrow\infty$. 146

5.8 Variation of temporal growth rate Ω_i with wave number k for different Fr at x/2R = 1.0, S = 0.14. 147

5.9 Variation of temporal growth rate Ω_i with wave number k for different Fr at x/2R = 2.67, S = 0.14. 148

5.10 Variation of absolute temporal growth rate Ω_i with density ratio for different Fr at x/2R = 1.0. 149

5.11 Variation of absolute spatial growth rate Ω_i with density ratio for different Fr at x/2R = 1.0. 150

5.12 Variation of absolute spatial growth rate Ω_i with density ratio as Fr$\rightarrow\infty$ at x/2R = 1.0 and 2.67. 151

5.13 Variation of absolute temporal growth rate Ω_i with density ratio as Fr$\rightarrow\infty$ at x/2R = 1.0 and 2.67. 152

5.14 Variation of absolute temporal growth rate Ω_i with Fr for S = 0.14 at x/2R = 1.0 and 2.67. 153

5.15 Variation of absolute temporal growth rate Ω_i with axial location as Fr$\rightarrow\infty$ for S = 0.14 and at x/2R = 1.0 and 2.67. 154

NOMENCLATURE

English Symbols

D	jet diameter
D_b	binary diffusivity coefficient
Fr	Froude number; $Fr^2 = \frac{U_j^2}{gR}\frac{\rho_j}{(\rho_\infty - \rho_j)}$
g	acceleration due to gravity
k	wavenumber
r	radial coordinate
r_o	low-density jet exit radius
R	radius of the jet shear layer
Ri	Richardson number; $Ri = \frac{gD}{U_j^2}\frac{(\rho_\infty - \rho_j)}{\rho_j}$
S	Density ratio
t	time
T	temperature
u	jet axial velocity component
U	jet base velocity
U_c	jet base centerline velocity
v	jet radial velocity component
x	axial coordinate
Y_j	local mass fraction of injected gas

Greek Symbols

δ_{ij} Kronecker delta

∇ del operator

ϕ azimuthal coordinate

λ wavelength

Λ velocity ratio in Monkewitz and Sohn (1988); $\Lambda = \frac{U_j - U_\infty}{U_j + U_\infty}$

μ fluid viscosity

υ fluid kinematic viscosity

ρ fluid mass density

ρ_j fluid mass density of low-density gas

ρ_∞ fluid mass density of high-density ambient gas

Ω angular frequency

κ Dale-Gladstone constant

ε Deflection angle

δ Instantaneous refractive index difference

η Refractive index difference

Superscripts

$(\,)'$ fluctuations

$(\bar{\ })$ averaged variable

$(\hat{\ })$ amplitude of variable

$(\tilde{\ })$ dimensional variable

Subscripts

∞	ambient gas property
j	low-density gas property

ABSTRACT

A low-density gas jet injected into a high-density ambient gas is known to exhibit self-excited global oscillations accompanied by large vortical structures interacting with the flow field. The primary objective of the proposed research is to study buoyancy effects on the origin and nature of the flow instability and structure in the near-field of low-density gas jets. Quantitative rainbow schlieren deflectometry, Computational fluid dynamics (CFD) and Linear stability analysis were the techniques employed to scale the buoyancy effects.

The formation and evolution of vortices and scalar structure of the flow field are investigated in buoyant helium jets discharged from a vertical tube into quiescent air. Oscillations at identical frequency were observed throughout the flow field. The evolving flow structure is described by helium mole percentage contours during an oscillation cycle. Instantaneous, mean, and RMS concentration profiles are presented to describe interactions of the vortex with the jet flow. Oscillations in a narrow wake region near the jet exit are shown to spread through the jet core near the downstream location of the vortex formation. The effects of jet Richardson number on characteristics of vortex and flow field are investigated and discussed.

The laminar, axisymmetric, unsteady jet flow of helium injected into air was simulated using CFD. Global oscillations were observed in the flow field. The computed oscillation frequency agreed qualitatively with the experimentally measured frequency. Contours of helium concentration, vorticity and velocity provided information about the evolution and propagation of vortices in the oscillating flow field.

Buoyancy effects on the instability mode were evaluated by rainbow schlieren flow visualization and concentration measurements in the near-field of self-excited helium jets undergoing gravitational change in the microgravity environment of 2.2s drop tower at NASA John H. Glenn Research Center. The jet Reynolds number was varied from 200 to 1500 and jet Richardson number was varied from 0.72 to 0.002. Power spectra plots generated from Fast Fourier Transform (FFT) analysis of angular deflection data acquired at a temporal resolution of 1000Hz reveal substantial damping of the oscillation amplitude in microgravity at low Richardson numbers (~0.002). Quantitative concentration data in the form of spatial and temporal evolutions of the instability data in Earth gravity and microgravity reveal significant variations in the jet flow structure upon removal of buoyancy forces. Radial variation of the frequency spectra and time traces of helium concentration revealed the importance of gravitational effects in the jet shear layer region.

Linear temporal and spatio-temporal stability analyses of a low-density round gas jet injected into a high-density ambient gas were performed by assuming hyper-tan mean velocity and density profiles. The flow was assumed to be non parallel. Viscous and diffusive effects were ignored. The mean flow parameters were represented as the sum of the mean value and a small normal-mode fluctuation. A second order differential equation governing the pressure disturbance amplitude was derived from the basic conservation equations. The effects of the inhomogeneous shear layer and the Froude number (signifying the effects of gravity) on the temporal and spatio-temporal results were delineated.

A decrease in the density ratio (ratio of the density of the jet to the density of the

ambient gas) resulted in an increase in the temporal amplification rate of the disturbances. The temporal growth rate of the disturbances increased as the Froude number was reduced. The spatio-temporal analysis performed to determine the absolute instability characteristics of the jet yield positive absolute temporal growth rates at all Fr and different axial locations. As buoyancy was removed ($Fr \rightarrow \infty$), the previously existing absolute instability disappeared at all locations establishing buoyancy as the primary instability mechanism in self-excited low-density jets.

CHAPTER 1: INTRODUCTION

1.1 Background

In fluid flow processes, such as jets, flames, and boundary layers, where many physical processes are at work, buoyancy often masks, and at a minimum complicates, the relevant flow physics. Low-density gas jets injected into a high-density ambient are known to exhibit self-excited global oscillations, accompanied by the formation of large vortical structures that interact with the jet flow under certain operating conditions. Owing to the large density differences, low-density jet flow processes are strongly affected by buoyancy. In addition to the fundamental scientific value, the analysis of buoyancy effects in such jets is relevant to phenomena such as submerged jet exhausts, volcanic eruptions and fuel leaks.

The prominent parameters useful in analyzing the instability in low-density jets include the jet Reynolds number ($Re = U_j d / \nu$ where U_j is the mean jet exit velocity, d is the injector inside diameter, ν is the kinematic viscosity), jet Richardson number ($Ri = [gd(\rho_\infty - \rho_j)/\rho_j U_j^2]$ where g is the gravitational acceleration, ρ_∞ and ρ_j are, the free-stream and jet densities respectively), the jet Froude number ($Fr^2 = \frac{1}{Ri}$), the momentum thickness ($\theta = \int_0^\infty \left[\frac{U-U_\infty}{U_j-U_\infty}\right]\left[1 - \frac{U-U_\infty}{U_j-U_\infty}\right] dr$, U_∞ is the jet co-flow velocity) and the density ratio ($S = \rho_j/\rho_\infty$). The instability, in several cases periodic, has been characterized by flow-oscillation frequency (f) or the Strouhal number ($St = fd/U_j$). Past studies were centered in two regimes: momentum- dominated ($Ri << 0.1$) and buoyancy-dominated ($Ri > 0.1$).

To facilitate visual understanding of the oscillating instability, flow visualization is presented in the form of instantaneous rainbow schlieren images for three cases in Figure 1.1. The range of flow conditions of the three cases encompasses the buoyancy-dominated and momentum-dominated regimes. The tube exit and outer surface are visible in the field of view as black regions in the images. In a color schlieren image, the background color (red) corresponds to zero density gradients and colors with increasing departure from the background correspond to increasing density gradients along the line of sight. Accordingly, the blue color signifies the region with high-density gradients. Both the images exhibit good symmetry about the centerline in the laminar region of the jet flow. For the cases with higher Re, transition from laminar to turbulent flow is visible in the field of view. The flow structure is repeatable for the cases shown and an oscillating instability is observed in the near field. It is plausible that this periodicity observed in low-density gas jets injected into a high-density medium is related to buoyancy effects. To understand the dynamics of the oscillating instability with buoyancy removed, experimental and analytical studies of the low-density jets under microgravity conditions are needed in all flow regimes.

1.2 Literature Review

In this section, existing literature on low-density jets is reviewed. First, experimental studies of low-density jets in different flow regimes are presented. Also, a review of the existing experimental work of buoyancy effects on flow instability is presented. The computational studies and stability analysis in low-density jets are presented later.

1.2.1 Experimental Studies in Laminar Flow Regime

A review of past investigations of mixing in gas jets with temperature and compositional changes is provided by Gouldin et al. (1986). Later studies by So et al. (1990), Richards and Pitts (1993), Panchapakesan and Lumley (1993) focused on the far-field behavior of low-density jets using helium as the jet fluid.

Studies in the buoyancy-dominated regime focused on the near-field oscillatory behavior of low-density jets using helium as the jet fluid for Ri ranging between 0.5 and 700. Subbarao and Cantwell (1992) carried out stroboscopic schlieren experiments in buoyant helium jets (S = 0.14) discharged from a circular tube into a co-flow of air. The Reynolds number was varied from 300 to 1500 and the Richardson numbers ranged between 0.5 and 6.0. Richardson number was independently controlled in a variable-pressure facility as Re was varied during the experiments. Schlieren visualization revealed that the transition to turbulence in the jet was sudden and the breakdown process was repeated precisely between oscillation cycles. The measured Strouhal number was independent of the Reynolds number. For Ri < 0.50, the Strouhal number was also independent of the Richardson number. However, for Ri > 1.0, St scaled with Ri, suggesting a buoyancy-dependent instability mode. Hamins et al (1992) performed shadowgraph experiments in self-excited buoyant helium jets for Ri = 7 to 700. Oscillations in the flow were not observed until a minimum jet flow rate was attained; these oscillations were similar to those observed in laminar diffusion flames. However, the minimum flow rate for the non-reacting plumes was much greater than the flow rate required to initiate pulsations in the flames. The Strouhal number correlation with Ri was a power law, similar to that obtained by Subbarao and Cantwell (1992).

Cetegen and Kasper (1996) extended the operating regime of Richardson numbers to those corresponding to pool fires and buoyant plumes. The oscillation frequency was represented by power law correlations between St and Ri for Richardson numbers varying from 1.5 to 5.0 x 10^4. Phase-resolved laser-Doppler velocity measurements revealed cyclic formation of a toroidal vortex ring near the jet exit. The toroidal vortex affected the surrounding flow field as it convected downstream. Flow-measurements were made using digital particle image velocimetry (DPIV) to depict the formation and convection of the vortex. Subsequent to the DPIV measurements, Cetegen (1997) found that the oscillations originating at the buoyant helium plume (Ri = 42) tip propagated upstream to contaminate the near-nozzle region. The size of the vortex formed was dependent on the forcing frequency. The frequency spectrum of the jet centerline velocity showed that the jet predominantly responded to the imposed flow excitation. As the excitation frequency approached the natural frequency of the jet, a chaotic behavior of the vortical structures was observed. This was in contrast to the behavior of the momentum-dominated jets, where spatial and temporal coherence of the flow was attained when the flow was excited at natural frequency. As the flow evolved downstream, the spectra exhibited a broadband mode with some of the frequencies other than the imposed one or its harmonics.

Pasumarthi (2000) performed an experimental investigation of the flow structure and oscillation characteristics of a pulsating helium jet injected into air using quantitative rainbow schlieren deflectometry (RSD). The jet structure was characterized by the frequency spectra, temporal evolution of the oscillations and mean and root-mean-square profiles of the helium mole fraction. The oscillations were stronger in inner flow and with

increase in jet exit diameter, became stronger in outer flow as well. Angular deflection data were obtained across full field of color images taken at a temporal resolution of 60Hz. Full-field concentration measurements were made for Richardson numbers between 0.5 and 6.5. A linear relationship was observed between the Strouhal number and the square root of Richardson number. The above-mentioned experimental studies were mainly concentrated in the buoyancy-dominated regime (Ri > 1.0).

Experiments in pure helium jets from a contoured nozzle by Richards et al. (1995) for Ri = 0.3 to 8 x 10^{-3} bridging the gap between buoyant and momentum-dominated flow regimes highlighted a global or self-excited behavior characterized by intense vortex interaction. Concentration measurements at several radial locations obtained by an aspirating probe indicated the presence of 'side jet' behavior with substantially increased levels of mixing. Flow visualization by Mie scattering showed that the substantial mixing occurred due to the expulsion of side-jets from the potential core region. Vortex pairing was observed at downstream locations with the appearance of a subharmonic component in the power spectra plots of density fluctuations. This signaled the location where the jet started to lose its coherent structure and began the transition to turbulence. It was also found that the power spectra of velocity and density were the same.

Sreenivasan et al. (1989) examined the near field of momentum-dominated helium/air jets from contoured nozzles and found a global oscillatory instability when the jet to ambient fluid density ratio (S) was less than 0.5. The Richardson number at the jet exit was less than 10^{-3}. The jet oscillatory instability was classified into two types, absolute and convective. The absolute instability identified by a sharp peak in the power spectral density of the velocity fluctuations dominated the flow in the entire near field of

the jet, and affected entrainment and mixing rates significantly. Less prominent peaks characterized the convective instability. When the density ratio was varied, the peaks in the power spectral density at harmonics of the oscillating frequency became more prominent. The most amplified disturbances downstream were at different frequencies (harmonics) showing the generation of strong side jets. Subsequent to their study of the global oscillating instability in low-density jets, Kyle and Sreenivasan (1993) performed extensive experiments in axisymmetric helium/air jets emerging into ambient air in momentum-dominated regime. The oscillating behavior was shown to depend upon density ratio, jet diameter and jet momentum thickness, and it was independent of the jet Reynolds number within the wide range covered ($1{,}500 < Re < 12{,}500$). Buoyancy was considered negligible in this range of the experiments. The flow structure repeated itself with extreme regularity for density ratio less then 0.6. The high degree of repeatability of the oscillating mode, coupled with the strong vortex interaction led to large centerline velocity fluctuations. Even though the oscillating mode had a high degree of repeatability, it did not exhibit a large spatial growth rate. Spatio-temporal measurements at different streamwise locations were deemed necessary before explaining this unusual instability occurring in these momentum-dominated flows.

To date, there have been few studies of the buoyancy effects on the oscillating instability in low-density jets. Also, the existing experimental studies of buoyancy effects have dealt specifically with the buoyancy-dominated regime. Yep et al. (2003) demonstrated the disappearance of density gradients in the absence of buoyancy (micro gravity) using RSD for helium jet with $Ri = 1.44$. The oscillations present in earth gravity disappeared in microgravity. Also, a significant widening of the jet was observed in

microgravity. These results provided direct physical evidence that the oscillating instability in buoyant helium jets was buoyancy-induced. Leptuch and Agrawal (2002) made significant improvements to the setup used by Yep et al. (2003) by incorporating a high-speed camera with a maximum frame rate of 0.5 ms. Also, power spectra of angular deflection data in unstable helium-air jet flows for much smaller Ri = 0.11 showed the disappearance of the oscillatory instability in microgravity signifying the buoyancy affects on the jet oscillations.

In the preceding experimental studies, buoyancy effects were neglected in the momentum-dominated flow regime because Ri was small. Although the assumption that buoyancy effects are small is justified in the jet core, buoyancy becomes locally significant in the jet shear layer where density and velocity gradients are significant. The exact nature of buoyancy effects on the oscillating flow structure in momentum-dominated jets can be determined from experimental studies of equivalent jets under microgravity conditions. The existing literature also lacks time-resolved measurements of density (or species concentration) distributions in the near field of low-density gas jets. Density measurements are important because the flow instability in momentum-dominated jets has been shown to depend on the jet density ratio (Kyle and Sreenivasan, 1993, Monkewitz et al., 1990). Transient responses of velocity or density spectra at different streamwise locations were deemed necessary to explain the instability and breakdown characteristics in momentum-dominated flows (Kyle and Sreenivasan, 1993). Detailed measurements of density or species concentration are needed not only to understand the dynamics of the oscillating flow field but also to provide quantitative data in the whole field. In this regard, techniques such as an aspirating probe are inadequate

because probe intrusion could alter the stability of the oscillating mode (Sreenivasan et al., 1989).

1.2.2 Experimental Studies in Transitional Flow Regime

Transition from laminar to turbulent flow in gas jets is a subject of considerable interest. Transitional jet consists of a laminar potential core near the injector, separated from a downstream turbulent region at the transition point as shown in Figure 1(a)-(b). The distance from the injector exit to the transition point or transition length decreases asymptotically with an increase in the jet exit velocity or the jet Reynolds number. Subbarao and Cantwell (1992) found that the flow transition in a helium jet injected into a co-flow of air was also affected by the jet Richardson number. For a given Re, the transition length decreased asymptotically with increasing jet Richardson number. This effect was attributed to buoyancy-induced acceleration of the jet fluid giving rise to faster core velocities and hence, a more unstable flow, at higher jet Richardson numbers. They proposed that the sudden breakdown to turbulence was governed by the highly structured and repeatable vortical structures formed in the upstream laminar region. Later studies by Cetegen (1996) and Yep et al. (2003) have confirmed that the vortical structures causing periodic oscillations in the jet flow originate by buoyant acceleration of the low-density jet fluid.

Periodic oscillations resulting in the breakdown to turbulence have also been observed in low-density gas jets at $Ri \ll 1.0$ (Kyle and Sreenivasan, 1993; Richards et al., 1995). Because of the small jet Richardson number, the buoyancy effects were considered negligible in these inertial jets. However, the buoyancy may be important locally, for example, in the low momentum region of the jet shear layer. Thus, buoyant

acceleration of the low-density fluid in localized regions of the jet may trigger the instability causing periodic flow oscillations and eventually, the breakdown to turbulence. This explanation is supported by the recent experiments of Yildirim and Agrawal (2004), who found that the oscillation frequency normalized by the buoyancy time scale correlated with the jet Richardson number in inertial low-density jets ($Ri<0.1$). For a given Re, the transition length (Z) normalized by 'd' correlated with the jet Richardson number, an observation also made by Subbarao and Cantwell (1992) in buoyant jets. Yildirim and Agrawal (2004) utilized different diameter injector tubes to vary the jet Richardson number for a given jet Reynolds number. Besides the limited range of the jet Richardson number achieved, the similarity parameters are not perfectly matched using this approach.

1.2.3 Computational Studies

Recent advances in computational fluid dynamics (CFD) tools have generated significant interest in analyzing a variety of fluid flow configurations. One of the earliest works was that of Laskey et al. (1989), who numerically studied unsteady diffusion flame of H_2/N_2. The computed flame flicker frequency matched with experiments. Shenoy et al. (1999) performed computations to simulate steady helium jets discharged vertically into air. The Reynolds number and Froude number based on jet exit conditions were, respectively, 150 and 80. The jet was laminar and the temperature and pressure variations were considered negligible. The computed helium concentration profiles agreed well with experimental measurements. Computational study of unsteady helium jets was undertaken by Mell et al. (1996). The computed oscillation frequency matched with experimental value obtained by Hamins et al. (1995). Soteriou et al. (2002) investigated

unsteady vortex dynamics of planar plumes numerically with emphasis on pulsating instability in the near field. The vortex shedding mechanism was explained by a Lagrangian transport element method. Strouhal number-Richardson number correlations showed that the pulsatile frequency was dependent on the gravitational acceleration and nozzle width.

1.2.4 Stability Analysis

Several researchers (Batchelor and Gill, 1962; Crow, 1972; Moore, 1977; Ffowcs-Williams and Kempton, 1978) have applied linear stability analysis to understand the stability characteristics of round jets with homogeneous shear layers and model the large-scale structures of the near-injector region.

Becker and Massaro (1968) analyzed the varicose instability characteristics of an axisymmetric jet with a radially uniform velocity distribution. The authors identified the vortex-shedding regimes in constant density jets with and without external acoustic forcing. The Strouhal number was found to scale with the square root of the jet exit Reynolds number. The ratio of the most highly amplified disturbance wavelength to the boundary layer thickness remained constant. Crow and Champagne (1971) found that the near-injector large-scale structure of jet turbulence was modeled well using linear stability analysis.

Crighton and Gaster (1976) modeled the coherent axisymmetric structures in a turbulent slowly diverging jet as inviscid linear instability modes of the mean velocity profile using multiple-scales expansion. For the first time, the effect of shear layer divergence was incorporated into the jet stability theory in a rational manner. The stability characteristics of the axisymmetric wave modes with prescribed real frequency

were explained by downstream growth rates, peak amplitude variations of the centerline axial velocity and the centerline pressure fluctuations. The results of these theoretical studies were in good agreement with the experimental results of Crow and Champagne (1971). A relation between the jet momentum shear layer thickness and the axial distance from the jet exit was developed incorporating the shear layer divergence, and was given by

$$\frac{R}{\theta} = \frac{100}{3\frac{x}{R}+4} \tag{1.2.1}$$

where R is the radius of the jet shear layer, θ is the jet momentum thickness and x is the axial distance along the centerline from the jet exit.

Michalke (1984) reviewed the early theoretical studies concerning the instability of axisymmetric jets. In addition to the laminar-turbulent transition, Michalke (1984) in his review discussed the evolution of large-scale coherent structures, as a consequence of jet instability, in the near-injector region of a turbulent jet. Inviscid locally parallel jet flow was considered and the study was restricted to axisymmetric homogeneous jets. A linearized pressure disturbance equation was derived by solving the conservation equations for the inviscid flow and by introducing normal mode disturbances. Mean temperature and velocity profiles were specified and the disturbance equation was solved by calculating the complex wavenumber eigenvalues for specified real wave frequency and azimuthal wavenumber. Four different forms of velocity profiles were used and the corresponding variations in the solution were reviewed. For higher frequencies, with increase in Mach number, the disturbance growth rate of the wave decreased and hence the flow became less unstable; whereas for lower frequencies, due to the insensitivity of

the phase velocity to the Mach number, the growth rates became independent of Mach number. The critical Reynolds number at which the jet became unstable was determined. For the axisymmetric disturbance mode (m =0), the critical Reynolds number was 68.3 for $R/\theta = 50$ and 110.6 for $R/\theta = 6.25$. For m = 1, the critical Reynolds number was in the range of 43 to 49 and was nearly independent of the jet parameter R/θ.

Michalke and Hermann (1982) investigated the influence of co-flow velocity on the instability of a circular jet using inviscid linear stability theory. The flow was assumed to be isothermal and viscous, diffusive and buoyancy effects were ignored. A basic mean jet velocity was assumed as shown by

$$U(r) = \frac{1}{2}\left(U_j + U_\infty\right) - \frac{1}{2}\left(U_j - U_\infty\right)\mathrm{Tanh}\left[\frac{1}{4}\frac{R}{\theta}\left(\frac{r}{R} - \frac{R}{r}\right)\right] \qquad (1.2.2)$$

where U_j is the jet core velocity, U_∞ is the external co-flow velocity and θ is the momentum boundary layer thickness of the jet shear layer. The radius R denotes the center of the shear layer where the velocity is the average velocity. The jet parameter R/θ characterizes jet velocity profiles at different axial positions. When no co-flow velocity was present, equation (1.2.1) proposed by Crighton and Gaster (1976) was used to relate the jet parameter R/θ and the normalized axial distance x/R. It was found that the spatial growth rate of the axisymmetric and azimuthal disturbances was dampened by the external flow.

Monkewitz and Sohn (1988) studied the linear impulse response of the flow by re-examining the linear inviscid stability of heated compressible axisymmetric jets. Locally parallel mean velocity and density profiles, infinite Froude number and zero

Eckert number were assumed. Buoyancy effects were neglected. A two-parameter family of velocity profiles was defined as

$$\bar{u}(r) = 1 - \Lambda + \frac{2\Lambda}{1 + \left(e^{r^2 \ln 2} - 1\right)^N} \tag{1.2.3}$$

where N was prescribed as a function of normalized axial distance x/L with L being the potential core length and Λ is the velocity ratio defined by equation (1.2.4), as the ratio of difference in velocities at the center of the jet and the ambient to the sum of velocities at the same locations.

$$\Lambda = \frac{U_c - U_\infty}{U_c + U_\infty} \tag{1.2.4}$$

where U_c was the jet centerline velocity, U_∞ was the velocity of the ambient gas. A turbulent Prandtl number was used to specify a relation between the mean flow velocity and density profiles as given by

$$\frac{1/\rho - 1}{1/S - 1} = \left(\frac{u - \Lambda - 1}{2\Lambda}\right)^P \tag{1.2.5}$$

where S was the local density ratio of jet centerline to the ambient gas and P was the turbulent Prandtl number. A pressure disturbance equation was derived and solved along the lines of Michalke and Hermann (1982). The linear impulse response of the flow was examined in detail and two different responses were identified. The first case was termed "absolutely unstable" where a locally generated small-amplitude disturbance grew exponentially at the location where it was generated and then eventually spread both upstream and downstream contaminating the entire flow field. The other response was termed "convectively unstable" in which the disturbance was convected downstream finally leaving the flow undisturbed. The density ratio that demarcated between absolute

and convective instabilities, for the helical mode was found to be 0.35, which was considerably lower than transition density ratio of 0.66 for the axisymmetric mode. A conclusion was made that the heated jet would become absolutely unstable for an exit density ratio less than 0.72. Both the axisymmetric and first spinning modes were investigated and the influence of mean flow profiles, exit Mach number, exit temperature and velocity ratio was discussed.

Yu and Monkewitz (1990) performed a linear stability analysis of two-dimensional inertial jets and wakes. The flow was assumed locally parallel and gravitational effects were neglected. It was found that the absolute frequencies scaled with the jet/wake widths and not the thickness of individual mixing layers. This theoretical approach indicated the presence of an absolute instability for density ratios less than 0.94 for plane jets, which was different from the value of 0.72 obtained by Monkewitz and Sohn (1998).

Jendoubi and Strykowski (1994) studied the spatio-temporal stability of axisymmetric jets with external co-flow and counterflow. The regions of absolute and convective instabilities were demarcated in the parameter space of velocity ratio, density ratio, Mach number and the shear layer thickness. Raynal et al. (1996) conducted an experimental investigation of instability of inhomogeneous plane jets issuing into ambient air. The experiment was conducted for three different values of nozzle width for a wide range of Reynolds number (250-3000) and density ratio (0.14-1.0). The jet exhibited self-excited sinusoidal oscillations with absolute instability features. It was shown that the Reynolds number was the better scaling parameter, for the frequency and amplitudes of these oscillations, than the ratio of jet width to momentum thickness. The

instability was characterized by sharp peaks in the power spectral density measured in the near field of the jet. The critical density ratio of 0.7, above which the instabilities disappeared, did not agree with the theoretical or experimental results of Yu and Monkewitz (1990). This discrepancy was accounted for by the differences in shape and relative positions of the inflection points of velocity and density profiles existing between the heated air jets and the helium/air jets.

Lawson (2001) investigated buoyancy effects on the stability of variable density jets using hyperbolic tangent velocity and density profiles to solve the pressure-disturbance equation. A similar hyperbolic tangent density profile was obtained by deriving a relation between the velocity and density profiles using dimensionless Schmidt number, Sc. The density profile was given by

$$\bar{\rho}(r) = 0.5\rho_\infty \left\{ 2 + \left(\frac{\rho_j}{\rho_\infty} - 1 \right) \left(1 - \mathrm{Tanh}\left[0.25 \frac{R}{\theta} \left(\frac{r}{R} - \frac{R}{r} \right) \right] \right) \right\}^{Sc} \qquad (1.2.6)$$

where r is the radial distance from the center of the jet. R/θ is the jet parameter characterizing the jet velocity profile at various axial locations as described in equation (1.2.1) by Crighton and Gaster (1979). The effect of density ratio and buoyancy (Froude number) on the nature of instability was studied in detail. At a very large Froude number (negligible buoyancy), a critical density ratio of 0.525 was found below which the jet was absolutely unstable. A critical Froude number was determined; for all the Froude numbers less than the critical Froude number the jet was absolutely unstable for any low density gas injected into high density ambient gas (any density ratio below 1). Experiments were also conducted to differentiate the instability characteristics of a round low-density gas jet and a round constant density jet. The mesh searching technique

outlined by Lin and Shen [24] was utilized to ascertain the nature of the instability. Critical Froude number and density ratio values were provided along with the correlations of Strouhal number. For the first time, buoyancy and Schmidt number effects were considered in the stability analysis of low-density jets. However, a discrepancy between the stability analysis results obtained by Lawson (2001) and experimental results of Yep et al. (2003) was observed. Lawson (2001) obtained a critical density ratio of 0.525; even at negligible buoyancy, for the density ratios less than 0.525, the jet was absolutely unstable. Whereas, the experimental results of Yep et al. (2003) showed that a helium jet injected into air (density ratio of 0.14) exhibited no oscillations in microgravity.

Vedantam (2003) investigated the effects of the mean velocity and density profiles on the instability characteristics of low-density gas jets. Three different sets of mean velocity and density profiles were utilized in the temporal and spatio-temporal stability analysis. The first set of mean velocity and density profiles assumed were those used by Monkewitz and Sohn (1988) for investigating absolute instability in hot jets. The second set of velocity and density profiles assumed for this study were the ones used by Lawson (2001). The third set of mean profiles included a parabolic velocity profile and a hyperbolic tangent density profile. The effects of the density ratio and the Froude number on the absolute instability of the jet, for the three sets of profiles, were studied. For large Froude number (negligible gravity) case, a critical density ratio was found for the three profiles at which the low-density jet became absolutely unstable. For all the profiles, the jet became more absolutely unstable as the density ratio was reduced further below the

critical density ratio and the jet was convectively unstable for the density ratios above the critical density ratio.

To date, stability analyses (Lawson, 2001; Vedantam, 2004) have assumed locally parallel flow neglecting streamwise variations in velocity and density fluctuations. Discrepancies observed between the experimental and stability analysis results in investigating buoyancy effects on unstable low-density jets could possibly be due to a variety of reasons. The parallel flow assumption and nature of velocity and density profiles might be plausible causes for the discrepancies. Owing to these reasons, stability analysis considering the effects of non-parallel flow would be helpful in bridging the gap between experimental and analytical results.

1.3 Objectives

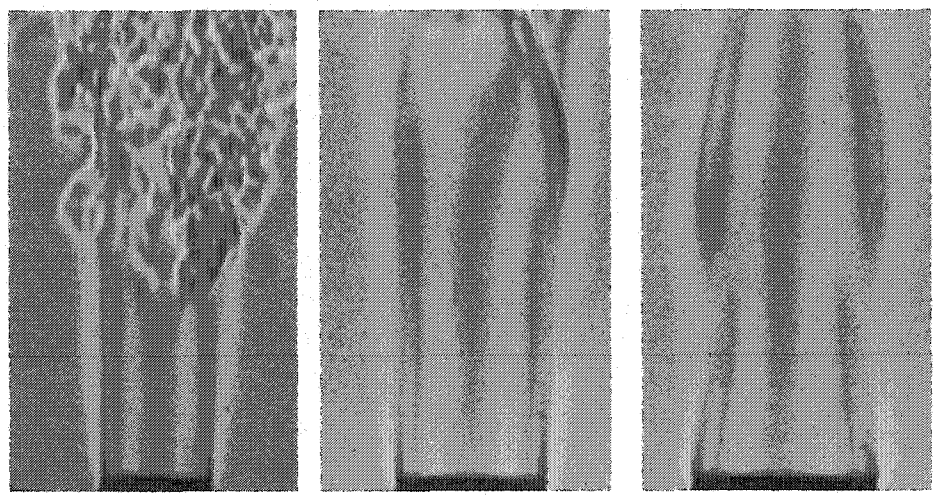
The primary objective of the proposed research is to study the buoyancy effects on the origin and nature of the flow instability and structure in the near-field of low-density gas jets, specifically in the momentum-dominated regime. As discussed previously, direct physical evidence of buoyancy effects on flow structure and instability in momentum-dominated low were inadequate in explaining and predicting the exact nature of buoyancy effects on the spatial and temporal growth rates of the flow instability. The specific objectives of the present study are listed below:

1. To study the scalar flow structure of self-excited buoyant helium jets discharged vertically into air and identify the shape, structure, and evolutionary path of the high vorticity entrainment region in Earth gravity.
2. To investigate buoyancy effects on the flow structure by subjecting the self-excited helium jet to micro gravity (free-fall) in momentum-dominated regime (Ri

< 0.5). The structure will be studied using Rainbow Schlieren Deflectometry apparatus integrated with a high-speed camera. The concentration field measurements yielding spatial and temporal evolutions of the instability, and frequency power spectra in the whole field will provide insight into the flow structure in the buoyant and non-buoyant regimes.

3. To perform computational simulations to obtain simultaneous visualization of the concentration and flow fields using commercial CFD code FLUENT.
4. To perform linear temporal and spatio-temporal stability analyses in variable density jets discarding the parallel flow assumption and considering buoyancy effects. The nature of the instabilities, whether absolute or convective will be determined.

The overall research effort will focus on achieving congruence in the analytical, experimental and computational approaches to the problem.



(a) (b) (c)

Figure 1.1: Rainbow schlieren images of helium jet for (a) Re = 1500, Ri = 0.002, d = 10.5mm, (b) Re = 800, Ri = 0.02, d= 14.5mm (c) Re = 200, Ri = 0.72, d = 19.05mm.

CHAPTER 2. EXPERIMENTAL METHOD

Experiments were conducted at the NASA John H. Glenn Research Center's 2.2s drop tower facility. A compact drop rig was utilized for tests in the drop tower to simulate microgravity conditions. The setup used by Leptuch (2001) was modified to visualize the structure of oscillating helium jet under Earth gravity and microgravity conditions using high-speed RSD flow imaging system. With the modifications in place, high jet Reynolds numbers (~1500) and low jet Richardson numbers (~0.002) were achieved. Prior to these experiments, the oscillating characteristics of helium jets in Earth gravity were studied by conducting experiments in buoyancy-dominated regime.

2.1 Experimental Setup

The experimental setup was designed to investigate flow oscillations in helium jets. Al- Ammar (1998), who conducted experiments with gas-jet diffusion flames in Earth gravity and microgravity, completed the original setup. Several modifications were made to the setup for experiments with helium jets in the present study. The experimental setup consists of a test rig, the flow system, the rainbow schlieren apparatus, and image acquisition system. The details of the above constituents for experiments in Earth gravity and microgravity will be discussed in the next sections.

2.1.1 Test Rig

The test rig, shown in Fig 2.1, consisted of an aluminum frame, 840-mm high, 960-mm long and 400-mm wide. It housed the flow system, the RSD apparatus, data acquisition system, and a ruggedized computer. A vertical tube to achieve fully developed flow at the tube exit was mounted at the center of the test rig. The RSD apparatus was configured on an optical breadboard that was maintained horizontal. The

optical layout of the rainbow schlieren apparatus is shown in Fig 2.2. The major components included a 100-μm wide, 3-mm high source aperture placed at the focal point of an 80mm diameter and 310mm focal length achromatic lens serving as the collimating lens. For experiments in Earth gravity, the light input was provided by a 600-μm diameter fiber optic cable (Thorlabs-FT-600-EMT) connected to a 150-W CUDA halogen light source. For experiments in microgravity, higher light throughput was needed at low exposure rates to reduce the blur. To increase the light through put, a focusing optic assembly was used to focus the parallel white light coming out the CUDA light source to a small area. That particular small area increased the intensity of light transmitted to the source aperture. The light input to the source aperture was provided by a 1000-μm diameter fiber optic cable (Thorlabs-FT-1000-EMT). The light rays deflected by the test media were decollimated by an 80-mm diameter, 1000-mm focal length achromatic lens. A pair of 100-mm diameter, aluminum coated flat surface mirrors was used to fold the rays by 180 degrees. A displaced image of the source aperture was formed at the focal point of the decollimating lens, wherein a 3-mm wide symmetric rainbow filter was placed.

2.1.2 Flow System

For experiments in Earth gravity, the external helium flow rate from a compressed gas cylinder was adjusted by the needle valve to obtain the desired Re (or Ri) for injector tubes (d = 32mm and 19mm). Sufficient vertical tubing length (~1m) was provided in each case to achieve fully developed flow at the tube exit. Helium flow was initiated by activating the solenoid valve.

For drop tower experiments, helium was supplied from two on-board 1000 cm^3 compressed gas cylinders. A constant supply pressure of 690 kPa (100 psig) was maintained using a pressure regulator. A calibrated mass flow meter (0-100 slpm) was used to measure the helium gas flow rate and a needle valve was utilized to control the flow. A solenoid valve was used to initiate and terminate the flow. The remaining flow system consisted of a plastic hose, U-tube segment and a straight tube. Three straight tubes of inside diameters of 19.05mm, 14.5 mm and 10.5mm exit diameters were used for experiments. The total length of the tubing was 300mm. The helium gas was discharged through the tubing system into the quiescent air.

2.1.3 Quantitative Rainbow Schlieren Deflectometry

The quantitative rainbow schlieren deflectometry is a nonintrusive, line-of-sight measurement technique. In the present study, this technique was used to visualize the flow and to make quantitative measurements of helium mole fraction across the full field of the pulsating jet. The RSD technique, developed by Greenberg et al. (1995), employs a computer-generated, continuously graded rainbow filter instead of a knife-edge used in the conventional schlieren technique. The filter generates a color schlieren image, wherein a color uniquely represents angular deflection of a light ray passing through the test section with the density gradients. The image is defined by the RGB (Red-Blue-Green) model, which is unsuitable for analysis owing to three independent variables. Thus, the HSI (Hue-Saturation-Intensity) model, wherein a color is uniquely represented by the hue value, was used for the image analysis.

2.1.4 Image Acquisition

For experiments in Earth gravity, the filtered image was acquired at 30 frames per second by the CCD array of a color camera with a 75-mm diameter focal length lens. Each image frame is a composite of two image fields that are 1/60s apart. The camera shutter was adjusted to yield exposure time of 1.0ms for each field image. Thus, each schlieren image field represents instantaneous flow structure because the fluid motion during the exposure time is small (about 1mm) compared to the jet diameter. After the flow was stabilized, a set of color schlieren images were acquired by the camera, digitized by a 24-bit PCI bus frame grabber, and stored in the system RAM in real time. Next, the digital images were transferred to the hard disk media and stored in TIFF format at pixel resolution of 640x480.

Higher framing rates were needed in momentum-dominated regime owing to smaller convective time scales compared to those in buoyancy-dominated regime. So, for the experiments in drop tower, the image acquisition system underwent major changes. The filtered images were acquired by a high-speed digital camera (Redlake Model Motion Xtra HG-TX) at an exposure time of 297-μs and an acquisition rate of 1000 frames per second. The spatial resolution of the each acquired image was 512 × 385 pixels measuring 512KB in size. The measurements were made with a temporal resolution of 1ms and spatial resolution of 0.2mm. The camera has a buffer memory of 1.5GB making it possible to store 2728 images at the acquisition rate of 1000 frames per second. This enables acquisition of 2.728 seconds of temporal data including 0.4 sec at the start of the drop in Earth gravity and 2.2 seconds of microgravity data, thereby effectively utilizing the available microgravity time in the drop tower. A programmable

logic controller (PLC model Direct Logic 05) was used to control the sequence of the operations in the experiment. The details of the PLC circuit and Ladder Logic program are provided in Appendix C.

2.2 Test Procedure

In this section, the 2.2s drop tower at NASA John H. Glenn Research Center research facility and the drop test procedure are briefly described. Various levels of the drop tower are shown schematically in Figure 2.3.

2.2.1 Drop Tower

Microgravity experiments were carried out in the 2.2s drop tower at NASA Glenn Research Center in Cleveland, OH. The drop tower has a vertical shaft 79ft and 1in (24.1m) high which allows 2.18 seconds of low gravity on the order of 0.0001g. The vertical shaft is shown in Figure 2.4. Experiments were conducted under atmospheric conditions with the drop rig enclosed inside an aerodynamic shield to minimize drag during the drop. The light supply was provided by a 150ft long external fiber optic cable connected to the light source. The total weight of the air shield and experimental rig was approximately 1075lb; the rig was decelerated after 2.18 seconds by an 11ft 7in (3.53m) diameter airbag. The deceleration levels at impact reached values of 20 to 40g.

2.2.2 Drop Procedure

The 2.2s drop tower is a multi-user facility accommodating up to 12 drops per day. At full capacity, the facility allows a researcher 45 minutes to perform a drop. The duration of the simulated microgravity allowed for the observation of only one experimental condition per drop. To establish experimental uncertainty, repeatability,

and consistency of the rig, all conditions were tested on ground prior to each individual drop.

Prior to each drop, the rig would go through a checklist that was necessary to both prepare the rig for the upcoming drop and to ensure that all systems and components were operating correctly to minimize equipment failure or malfunction. This would consist of charging the helium gas cylinders to full capacity levels, checking battery charge, inspection of the test section for any damage, and securing any loose wiring or tubing. Once the checklist was completed, a "dry run" or "Earth gravity drop" was performed to simulate a drop sequence and check the experimental readiness of the rig. This would allow the researcher to observe, evaluate, and correct any aspect of the drop sequence to accommodate each experiment individually.

When the rig successfully passed the checklist it was ready to be dropped. It was then rolled to the fifth floor of the drop tower where it was placed within the air shield. The air shield and rig were then hoisted to the eighth floor and suspended by the drop release mechanism comprising of a steel cable attached to a sharpened chisel inserted in a pneumatic actuator as shown in Figure 2.5. The hanging fiber optic cable is also visible in Figure 2.5. The rig was now suspended 7.5-in (19.8-cm) above the bottom of the air shield. Next, the operator would announce all personnel in the tower to standby for a drop. Then the light source was switched on and camera was activated. The air-shield was then closed and secured at which point the 60-second countdown would commence. The whole sequence of operations inside the drop rig was controlled by the PLC. First, the solenoid valve was turned on to initiate the flow in Earth gravity. Sufficient time was allowed for the flow to develop and stabilize into an oscillatory mode at the required flow

rate. Then, the PLC triggered the storage of schlieren images in the camera memory. After 0.4 seconds capture of Earth gravity data at which point the 60-second countdown would end, the PLC executed the drop. The solenoid valve was deactivated to terminate the flow after the drop. Figure 2.6 shows the air shield resting on the air balloon after the drop process. After retrieving the drop rig, the images were transferred from the camera memory to hard disk memory of a computer.

2.3 Rainbow Schlieren Analysis

The schlieren method is one of the oldest and most commonly used approaches for flow visualization. When a low-density gas jet is injected into high-density fluid, the path of a light ray through the stratified fluid is deflected because of the changes in the refractive -index gradient. In rainbow schlieren deflectometry, these deflected rays after decollimation pass through a continuously graded color filter of known transmissivity to create a color schlieren image of the test media. This color representation eliminates problems associated with conventional knife-edge schlieren such as inhomogeneous absorption of light by the medium and nonlinearities in the recording media.

A photograph of the symmetric rainbow filter is shown in Figure 2.7. The filter is 3-mm wide and it was printed on a 35-mm color slide at a resolution of 115 pixels/mm. Note that the filter colors vary in the transverse direction indicating that the filter is sensitive only to transverse ray displacements. The filter is positioned exactly at the focal plane of the decollimating lens. After printing, the filter was calibrated in the schlieren setup by traversing the filter using a micro positioner. At each filter location, a rainbow schlieren image was taken without the test medium. The hue at a given traverse location was represented by the average hue of the schlieren image at that location. The average

hue is average of the all hues corresponding to the pixels in the chosen window. Different window sizes were used and the standard deviation showed no significant change. For the present experiments, a window of 200x200 was chosen for averaging. Figure 2.8 shows the filter calibration curve exhibiting the filter transmissivity function. The standard deviation of the hue at each traverse location is also shown in Fig 2.8. The maximum standard deviation is about 15 degrees and it occurs at an average hue of about 150 degrees. It will be shown later that the region corresponding to high standard deviation in Fig 2.8 is subjected to large measurement errors i.e., a large standard deviation of hue leads to large measurement uncertainties. Therefore, the filter size must be selected to optimize the measurement sensitivity and accuracy in a given experiment. A smaller filter, providing high measurement sensitivity, is unsuitable if the source image is large. Conversely, a wider filter limits the measurement sensitivity and hence the range of colors obtained in the rainbow schlieren image. Al-Ammar (1998) noted that the filter optimization is a compromise between measurement sensitivity and measurement accuracy. In the present study, filters of width 2.0mm, 2.5mm, 3mm, and 3.5mm were generated. Preliminary experiments were performed using 2.5mm wide filter. For tube diameter of 32mm, ray displacements at the filter plane exceeded the filter width, and hence the analysis produced erroneous results. Thus, a filter of 3.0mm width was employed for experiments in Earth gravity. The process was repeated for the lowest tube diameter with the highest jet flow rate possible and the optimum filter size of 3.0mm was finalized and utilized for microgravity experiments.

The hue at a point in the schlieren image is related to the deflection angle and hence, to the refractive-index gradient in the medium. In the following section, a brief

descriptions of the analysis employed in this study is presented. The transverse displacement at the filter plane is related to the deflection angle (Goldstein and Kuehn, 1996)

$$d(y) = \tan\left[\varepsilon(y)\right].f \approx \varepsilon(y).f \tag{2.3.1}$$

where f is the focal length of the decollimating lens, and $\varepsilon(y)$ is the deflection angle of a ray at the projected location 'y'. The transverse displacement is found from the hue in the color schlieren image using the filter calibration curve shown in Fig 2.8. The deflection angle of a light ray passing through an axisymmetric refractive index field for small deflections is determined applying the relationship given by

$$\varepsilon(y) = 2y\int_{y}^{\infty}\frac{d\delta}{dr}\frac{dr}{\sqrt{r^2 - y^2}} \tag{2.3.2}$$

Here $\varepsilon(y)$ is the beam deflection angle at the projected radial location y, $\delta = (\eta\text{-}1)$ is the normalized refractive index difference and η is the refractive index normalized by that of the surrounding medium. Next, the displacement is related to the angular ray deflection to determine the refractive index difference using the Abel inversion for an axisymmetric medium given by

$$\delta(r) = -\frac{1}{\pi}\int_{r}^{\infty}\varepsilon(y)\cdot\frac{dy}{\sqrt{(y^2 - r^2)}} \tag{2.3.3}$$

In discrete form this is given as

$$\delta_i = \delta(r_i) = \sum_{j=i}^{NJ} D_{ij}\varepsilon_i \tag{2.3.4}$$

where ε_i is the angular deflection of ray at a projected radial location 'i' and the geometric coefficients D_{ij} are given by Agrawal et al.(1999) as

$D_{ij} = 0 \qquad j < i$

$= (1/\pi).\ A_{i,j} \qquad j = i$

$= (1/\pi).\ [A_{i,j} - B_{i,j-1}] \qquad j > i$

with $$A_{i,j} = \sqrt{(j+1)^2 - i^2} - \sqrt{j^2 - i^2} - (j+1)\ln\left(\frac{j+1+\sqrt{(j+1)^2 - i^2}}{j+\sqrt{j^2 - i^2}}\right)$$

$$B_{i,j} = \sqrt{(j+1)^2 - i^2} - \sqrt{j^2 - i^2} - j\cdot\ln\left(\frac{j+1+\sqrt{(j+1)^2 - i^2}}{j+\sqrt{j^2 - i^2}}\right)$$

Equation 2.3.4 has a form similar to equation 1 in Dasch (1992) to invert the path integrated interferometric data or absorption measurements. In this form, the coefficients D_{ij} are independent of the sampling interval.

For a mixture of gases, the refractive index difference is given by Yates (1993) as

$$\delta = \frac{P}{\bar{R}T}\sum_j \kappa_j X_j M_j \qquad (2.3.5)$$

where P is the pressure, $\bar{R}$ is the universal gas constant, T is the temperature, κ is the Dale-Gladstone constant, X is the species mole fraction, and M is the species molecular weight. The summation is taken over all species 'j', i.e., oxygen, nitrogen, and helium. Equation (2.3.5) is used to construct a plot between refractive index difference and helium mole fraction, assuming nitrogen to oxygen mole ratio of 3.76 in standard air.

2.4 Image Processing

The schlieren images were processed and analyzed using in-house computer programs. The images were digitized in the tag image file format (TIFF). A typical TIFF file consists of three sections: image file header (IFH), image file directory (IFD), and bitmap data. The IFH is the first eight bytes of a TIFF file and was used to determine the format, version and location of the IFD of the image. The IFD defines the exact location of the bitmap data (Murray, 1994).

The image processing programs were written in Fortran. These were converted to C programming language using a conversion program. This was done keeping in view the extensive availability of TIFF image processing libraries in the C programming language. Data are read by the program in the form of individual scan lines in each image. An image consists of rows and columns of pixels, similar to a matrix with rows and columns of elements. A scan line is an array of pixels in a row of the image. Once the scan line data have been stored, the color information at each individual pixel is determined using the RGB color model. In this model, the color at each individual pixel is defined by three attributes namely, Red, Green, and Blue: each ranging from zero to 255 (providing an 8-pixel resolution). The RGB format is inconvenient because three variables are required to represent a color. Thus, the RGB data was converted to Hue, Saturation, Intensity (HSI) values, wherein a color is uniquely represented by hue while keeping saturation and intensity constant. The hue varies from zero to 360 degrees (0 to 2π radians). Using a subroutine within each program the image data stored in the RGB model were converted to the HSI color model.

2.4.1 Time Dependent Technique

A time dependence technique was developed to create an image containing the color data from consecutive images at a specified axial plane. After specifying the radial pixel location of the tube center and tube inside diameter in pixels, the computer program generates the space-time image at the specified axial location. A sample space-time image is shown in Figure 2.9. The axial location was normalized with respect to the tube inside diameter (d). In the space-time image, the x-axis indicates the radial location and the y-axis corresponds to the time.

Space-time image is an effective way to represent the temporal evolution of the jet. It saves computational effort requiring a single image to determine desired results such as the frequency spectrum at a given axial plane. In addition, the image generated is used to determine helium mole fraction profiles at specified axial locations. Instantaneous contours of deflection angle and helium mole fraction are obtained for quantitative representation of the jet flow and location, size and speed of the vortical structures.

2.4.1.1 Frequency Spectrum

The frequency spectrum at a specified radial location is determined using the hue data from the time-space image and applying the fast Fourier Transform (FFT) algorithm given by Teukolsky et al. (1992). Since the hue values are linearly related to the deflection angle, the frequency spectrum of the deflection angle is same as that of hue.

2.4.1.2 Temporal Evolution

The temporal evolution of various parameters was determined from the space-time image. It shows how the image hue at a specified axial plane changes with the passage of time. The RGB data from the space-time image is converted to hue values

which are stored in a two dimensional array. The hue data from the image are transformed into deflection angle using the filter calibration curve. First, the transverse location on the calibration curve corresponding to the background hue of the image is calculated. The center location corresponds to zero deflection angle. The location of minimum hue value in the center region corresponds to the center location. Ideally, this location should correspond to the center position in the filter calibration curve. Due to measurement noise at and around the center of the jet, the center location slightly varies at different axial planes. The instantaneous refractive index difference is then calculated from deflection angle using equation (2.3.4). Finally, the instantaneous helium mole fraction is calculated from the refractive index difference using equation (2.3.5).

2.4 Uncertainty Analysis

Uncertainties in measurements of angular deflection arise because of spatial variations of hue in images used to generate the filter calibration curve as described by Al-Ammar et al. (1999). The local uncertainty for a given hue in a rainbow schlieren image is found from the standard deviation of the filter calibration curve. Using equations (2.3.1)-(2.3.5), the uncertainty in helium mole percentage could be calculated. In this study, uncertainty in angular deflection corresponding to the maximum local uncertainty was $16.0*10^{-4}$ degree. The uncertainty in angular deflection is most critical in regions of low density-gradients (typically near the jet center where the helium concentration is high) causing small angular deflection, and hence, poor signal-to-noise ratio. Furthermore, for a given uncertainty of angular deflection, the uncertainty of refractive index difference or helium concentration increases exponentially towards the jet centerline. The uncertainty of helium concentration measurements is between 5 and 10%

for r/d < 0.2 for concentration measurement above 90%. Outside these constraints, the helium concentration measurements are accurate to within 5% of the measured value. Experimentally, image blur was unavoidable because of the finite exposure time. In this study, the maximum estimated image blur by convection is 5mm, corresponding to a jet exit velocity of 17 m/s and the exposure time of 297μ-sec.Details of uncertainty analysis procedure are outlined in Appendix B.

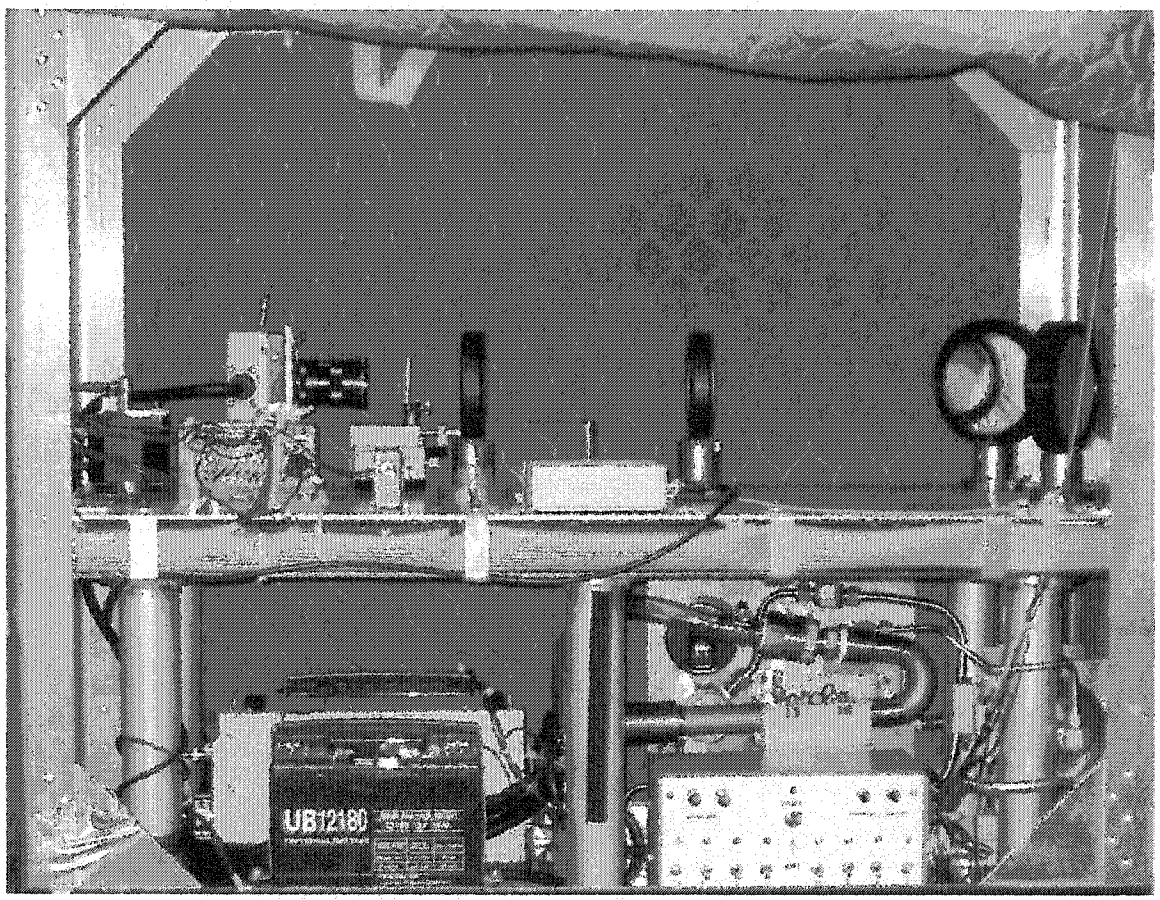
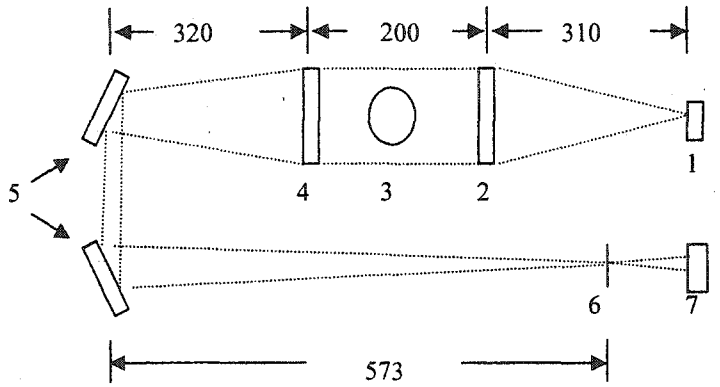


Figure 2.1: A photograph of the experimental test rig.



All dimensions are in mm

Figure 2.2: Optical Layout

1 - Source aperture, 2 - Collimating lens, 3 – Test Media,

4 -Decollimating lens, 5 - Flat surface mirrors, 6 – Rainbow Filter, 7 – Camera lens

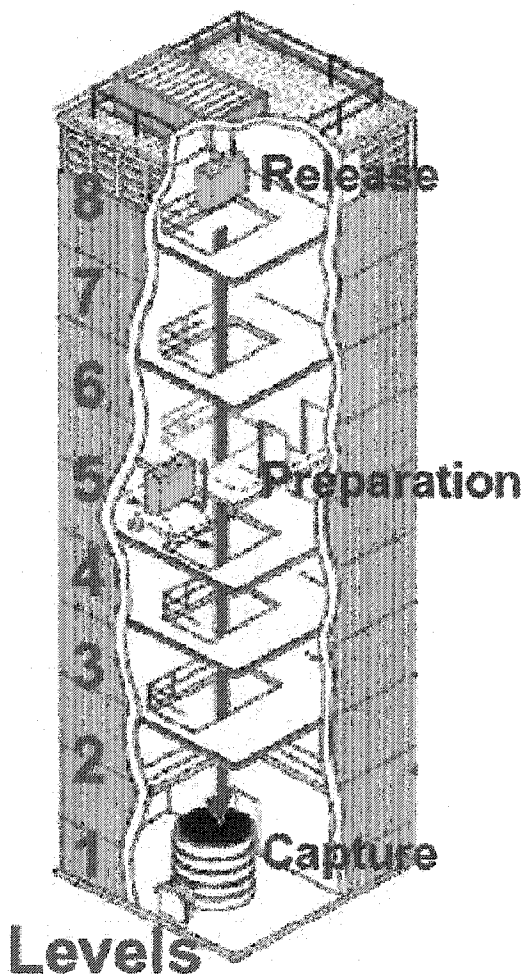


Figure 2.3: A cutaway drawing of the 2.2s Drop Tower, showing the levels on which an experiment package is prepared, released and captured.
(Courtesy: http://microgravity.grc.nasa.gov).

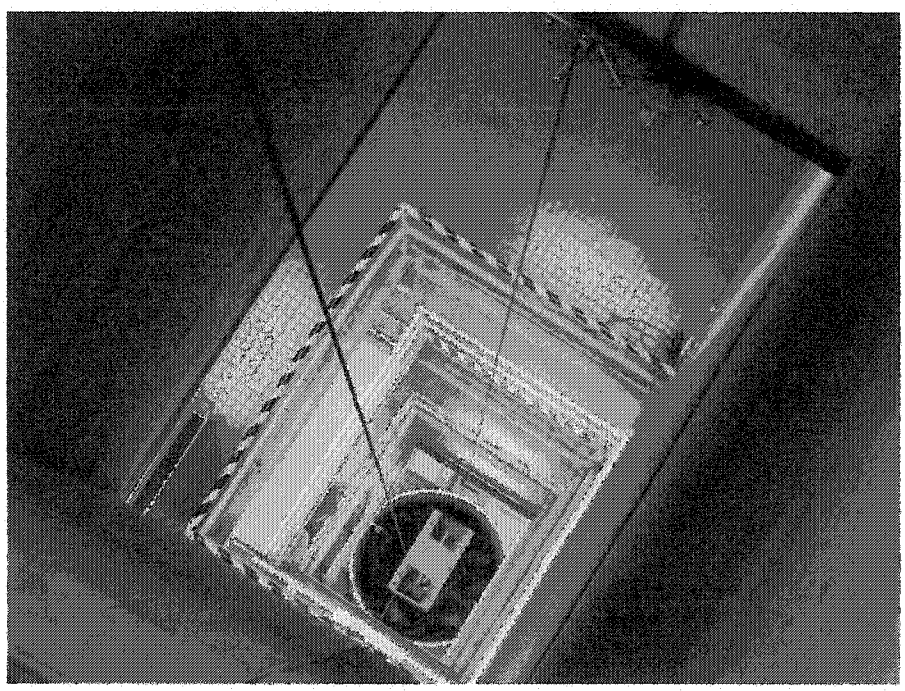


Figure 2.4: The vertical shaft of the drop tower. The air shield containing the rig is being hoisted to the eighth floor in preparation for a drop.

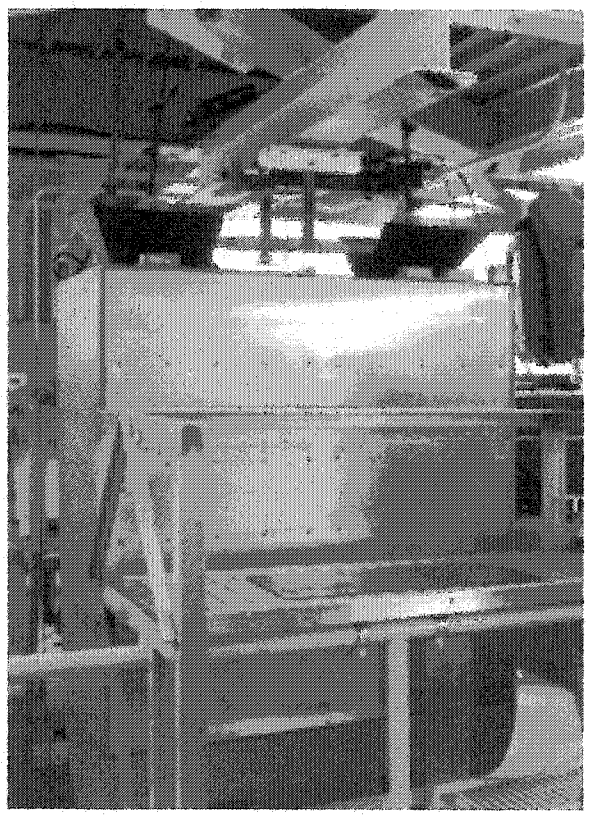


Figure 2.5: The air shield containing the rig is being suspended by the drop-release mechanism on the eighth floor in preparation for a drop.



Figure 2.6: The air shield containing the rig resting on the pneumatic balloon after a drop.

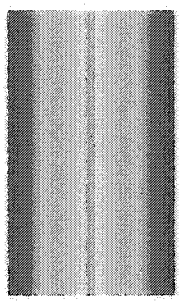


Figure 2.7: Rainbow color filter

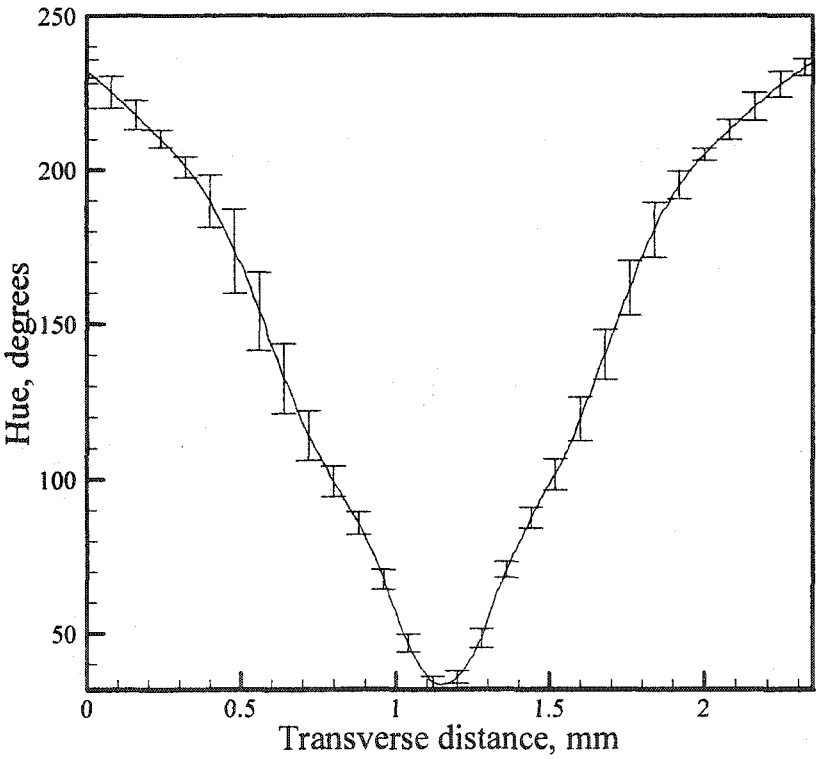


Figure 2.8: Filter calibration curve.

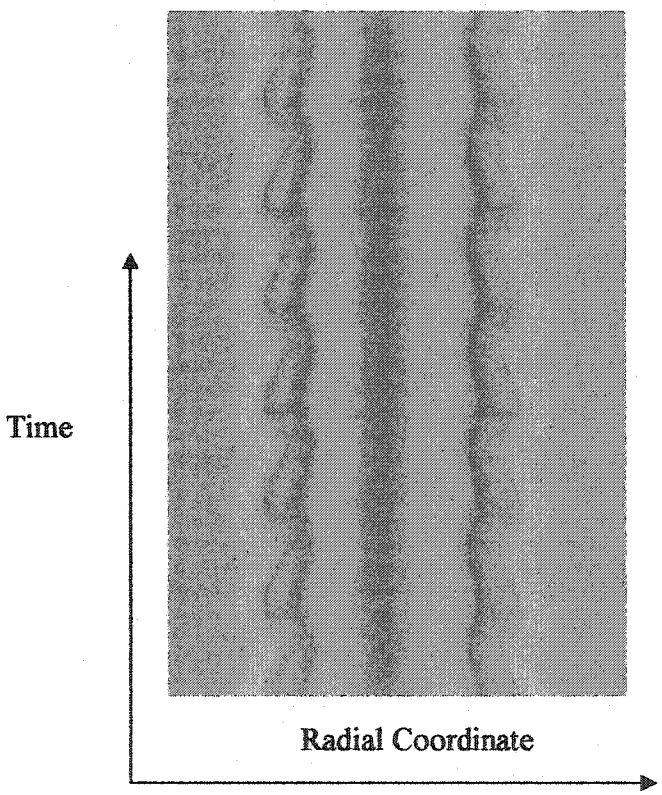


Figure 2.9: Space-time image

CHAPTER 3. NUMERICAL PROCEDURE

In this section, the details of a computational model of the unsteady helium jet developed using a commercial code FLUENT are provided.

3.1 Governing Equations

The governing equations for 2D axisymmetric, laminar, unsteady, and axisymmetric flow were expressed in cylindrical coordinate system as:

Continuity:

$$\frac{\partial \rho}{\partial t}+\frac{1}{r}\frac{\partial}{\partial r}(\rho v r)+\frac{\partial}{\partial z}(\rho u)=0 \tag{3.1.1}$$

Momentum:

$$\frac{\partial}{\partial t}(\rho u)+\frac{1}{r}\frac{\partial}{\partial r}(\rho r v u)+\frac{\partial}{\partial z}(\rho u u)=\frac{1}{r}\frac{\partial}{\partial r}\left(\mu r\frac{\partial u}{\partial r}\right)+\frac{\partial}{\partial z}\left(\mu\frac{\partial u}{\partial z}\right)+\left(\rho_{\infty}-\rho_{j}\right)g+S_{u} \tag{3.1.2}$$

$$\frac{\partial}{\partial t}(\rho v)+\frac{1}{r}\frac{\partial}{\partial r}(\rho r v v)+\frac{\partial}{\partial z}(\rho u v)=\frac{1}{r}\frac{\partial}{\partial r}\left(\mu r\frac{\partial v}{\partial r}\right)+\frac{\partial}{\partial z}\left(\mu\frac{\partial v}{\partial z}\right)+S_{v} \tag{3.1.3}$$

where

$$S_{u}=\frac{\partial}{\partial z}\left(\mu\frac{\partial u}{\partial z}\right)+\frac{1}{r}\frac{\partial}{\partial r}\left(\mu r\frac{\partial v}{\partial r}\right)-\frac{2}{3}\left\{\frac{\partial}{\partial z}\left(\mu\frac{\partial v}{\partial z}\right)+\frac{\partial}{\partial z}\left(\mu\frac{\partial u}{\partial z}\right)\right\}$$

$$S_{v}=\frac{\partial}{\partial z}\left(\mu\frac{\partial u}{\partial r}\right)+\frac{1}{r}\frac{\partial}{\partial r}\left(\mu r\frac{\partial v}{\partial r}\right)-\frac{2}{3}\left\{\frac{1}{r}\frac{\partial}{\partial r}\left(\mu r\frac{\partial v}{\partial r}\right)+\frac{1}{r}\frac{\partial}{\partial r}\left(\mu r\frac{\partial u}{\partial z}\right)\right\}-2\mu\frac{v}{r^{2}}$$

Mixture Fraction:

$$\frac{\partial}{\partial t}(\rho f)+\frac{1}{r}\frac{\partial}{\partial r}(\rho r v f)+\frac{\partial}{\partial z}(\rho u f)=\frac{1}{r}\frac{\partial}{\partial r}\left(\rho D_{b} r\frac{\partial f}{\partial r}\right)+\frac{\partial}{\partial z}\left(\rho D_{b}\frac{\partial f}{\partial z}\right) \tag{3.1.4}$$

where u, v are the axial and radial velocities respectively, μ, ρ, D_b, f are the mixture viscosity, mixture density, binary mass diffusion coefficient (helium-air) and mixture fraction respectively. The terms g, ρ_{∞} and ρ_j represent, respectively, the acceleration due

to gravity, density of the ambient fluid and density of the jet fluid at the exit. The computations were performed to simulate the experiments in Earth gravity in a helium jet discharged vertically into ambient air described previously. The internal diameter of the jet tube was 32 mm and the wall thickness was 2 mm. The Reynolds number and Richardson number based on jet exit conditions were, respectively, 147 and 5. The jet was modeled as laminar and the temperature and pressure variations were assumed to be negligible. In this study, the jet flow was considered as a binary fluid system by treating air as a single species. In this binary fluid system, the species concentrations and hence, the fluid properties were uniquely related to the helium mass fraction because the sum of individual species mass fractions is equal to unity. Accordingly, the transport equations of helium mass fraction coupled with the conservation equations of the mixture mass and momentum were solved. The mixture density and kinematic viscosity (based on kinetic theory and Wilkes mixture formula) were defined as

$$\rho = \frac{P}{RT\sum_i \frac{m_i}{M_i}}$$

$$\mu = \sum_i \frac{X_i \mu_i}{\sum_i X_i \phi_{ij}}$$

$$\text{where } \phi_{ij} = \frac{\left[1+\left(\frac{\mu_i}{\mu_j}\right)^{\frac{1}{2}}\left(\frac{M_j}{M_i}\right)^{\frac{1}{4}}\right]^2}{\left[8\left(1+\frac{M_j}{M_i}\right)\right]^{\frac{1}{2}}}$$

Here X_i, M_i, m_i, μ_i represent the mole fraction, molecular weight, mass fraction and dynamic viscosity of species i respectively. The terms P, $\overline{R}$, T represent the operating

pressure (in this case atmospheric pressure), universal gas constant and ambient temperature respectively. The helium-air binary mass diffusion coefficient was specified as a constant.

3.2 Model Formulation

The computational preprocessing was conducted using Gambit, a grid development software tool. Here the computational domain was built with the requisite dimensions. It extended 20d in radial direction and 20d in the axial direction. The upstream boundary of the jet was placed at a distance of 1.0d below the tube exit. The domain was divided into several zones to facilitate the adaptation of different boundary conditions as outlined in Figure 3.1. Because of symmetry, only one side of the jet was considered for analysis. The domain was meshed using control-volume formulation. Initially, the analysis was done using a coarse grid of 2000 elements. The model shown in Figure 3.1 was exported to Fluent as a mesh-format file. After the flickering phenomenon was observed, the grid was refined to 35,000 control volumes and the analysis was repeated. A grid-size convergence check was performed which revealed the importance of finer grid size in the sensitive gradients.

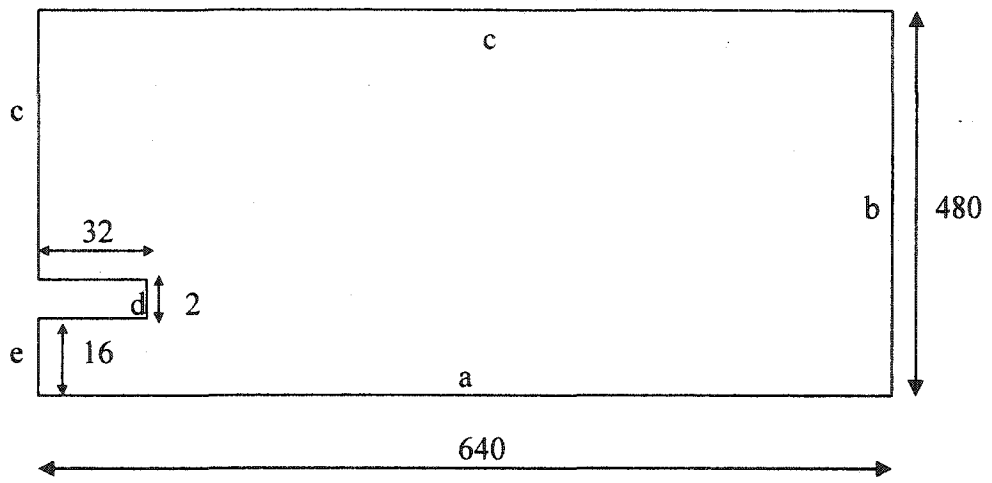
3.3 Flow Formulation

The helium jet flow was modeled as laminar, axisymmetric and unsteady. The boundary conditions were given to match the operating conditions in the experiment. Thus, parabolic velocity profile was assumed at the injector inlet boundary. In addition, the mass fraction of helium was specified as unity (pure helium) at the injector inlet. Far away radially, ambient pressure condition was specified. In the axial direction, gradients

are assumed to be small far away from jet exit and hence, outflow boundary condition was specified there.

3.4 Solution Procedure

The analysis in the model was started with a zero initial guess everywhere in the computational domain (no flow). Convergence criterion was 0.0001 for the flow and concentration variables based on the conservation equations. The steady state solution was given as the initial guess for the unsteady case. A time step of 1.667 ms ($1/600^{th}$ of a second) was used. The total time for flow computations was 10 seconds. Data were saved after every ten time steps. This was done to compare the computed results with the experiments, which had a frame rate of $1/60^{th}$ of a second.



All dimensions are in mm

Figure 3.1: Computational domain of the numerical model of helium jet ejecting vertically into ambient air. a. Axis of symmetry (Jet centerline), b. Outflow boundary, c. Ambient pressure condition, d. Pipe wall, e. Helium jet inlet.

CHAPTER 4: EXPERIMENTAL RESULTS

The test matrix for experiments is shown in Table 4.1. Cases 1 and 2 were conducted under Earth gravity conditions. Cases 3-14 were conducted in drop tower for both Earth gravity and microgravity conditions. In these test cases, noticeable change in transitional flow was observed in Cases 6 and 9. The test cases listed in Table 4.1 show that the range included experiments in both the buoyancy-dominated (Ri > 0.1) and the momentum-dominated flow regimes (Ri <0.01).

This chapter is divided into three sections. First, the experimental results detailing the dynamics and temporal behavior of the oscillating jet flow in buoyancy-dominated regime under Earth gravity conditions will be presented. Then, results obtained from drop tower experiments highlighting buoyancy effects in buoyancy-and momentum-dominated laminar low-density jets using RSD are presented. Finally, buoyancy effects in the transitional flow regime are presented.

4.1 Buoyancy-Dominated Flow Regime

As a first step, several experiments were conducted to ascertain the global flow oscillations in Earth gravity in the operating range of Re =130 to 150 and Ri = 0.3 to 6.6, which overlapped with experiments in the buoyant flow regime by Subbarao and Cantwell (1992). For each case, the angular deflection data at several axial and radial locations were analyzed using fast Fourier transforms. The results indicated that: (1) the flow oscillated at a dominant frequency that was independent of the spatial location, and (2) the Strouhal number was nearly independent of Re and dependent only on Ri, suggesting a buoyancy-driven instability. To understand structural and temporal details of the fluctuating jet flow, helium concentration data were analyzed for test Cases 1 and 2

listed in Table 4.1. The structure of the flow field and vortex dynamics are discussed for the Case 1. The effects of Richardson number on the oscillating flow field are illustrated by the Case 2.

4.1.1 Rainbow Schlieren Visualization

A sequence of color schlieren images (16.7ms apart) is shown in Figure 4.1 to facilitate visual understanding of the oscillating flow. The tube exit and outer surface are visible as black regions in the lower row images. The downstream region ($z/d > 1.8$) in the upper row images was visualized by lowering the jet tube with respect to the schlieren field-of-view. Although the experiments were conducted at different times, an excellent match between images in the upper and lower rows was achieved because flow oscillations are periodic. In a color schlieren image, the primary colors with increasing departure from the background color (red) are yellow, green, and blue. Accordingly, the blue color signifies large angular deflections produced in a region of high-density gradients. The schlieren images exhibit good symmetry about the centerline confirming axisymmetry, except farther downstream at $z/d > 3.0$. Changes in the flow structure during an oscillation cycle are significant. High density-gradients in the wake region of the tube wall are indicated by the blue color in that region. Color gradations on the tube outer wall indicate that the jet fluid has diffused upstream of the tube exit. The first image at time $t = 0.0$ ms shows a wavy structure with the jet contracting near the exit, bulging in the mid-region ($z/d = 0.5$), and contracting gradually in the downstream region. A secondary structure (signifying a toroidal vortex as discussed later) surrounds the primary jet at $z/d > 2.0$. In the second image at $t = 16.7$ms, the potential core is contracted until $z/d = 0.5$, where a secondary structure has formed. The newly-formed secondary structure

is clearly visible at z/d > 1.0 in the third image at t = 33.3ms. The next image at t = 50.0ms depicts a bulge near the jet exit. Furthermore, the secondary structure has moved downstream. The last image at t = 66.7ms depicts flow features between t = 0.0 and 16.7ms because the oscillation cycle has repeated. This is consistent with the oscillation period, T = 58.8ms (or oscillation frequency, f = 17 Hz) determined from the spectral analysis of angular deflection data. Accordingly, the last image at t = 66.7ms replicates the oscillating flow at t = 7.9ms.

4.1.2. Time-Resolved Concentration Distributions

Figure 4.2 shows helium mole percentage contour plots during an oscillation cycle. Data from two consecutive cycles were arranged in phase to depict the gradual flow development. Only one side of the jet is shown, owing to the symmetry observed until about z/d = 3.0. In the first plot at t = 0.0ms, small indentations in contour levels are observed near the tube exit (z/d = 0.1). Contraction of the primary jet by radial inflow of the surrounding fluid grows gradually till z/d = 0.4 at t = 7.9ms. Contour levels at t = 16.7ms show the presence of a local minimum and maximum near z/d = 0.6. This reversal in curvature of concentration contours is attributed to the entrainment caused by the toroidal vortex, as illustrated in Figure 4.6. The entrained fluid mixes with helium in the primary jet during the upward fluid motion inside the vortex. The radial profile at axial location A in Figure 4.6 shows the helium concentration increasing gradually from the outside until the inflection point 3, signifying the outer edge of the entrainment region. Helium concentration decreases from the maximum at point 3 to a minimum at point 2, construed as the mid-point of the entrainment region. Helium concentration rises from point 2 to point 1 as the vortex interacts with the primary jet. The leading or trailing

edges of the entrainment region have a concentration profile with an inflection point, instead of a local minimum and maximum. The entrainment region (expected to contain a high amount of vorticity) is referred to as the vortex. The vortex boundary can be identified manually from concentration profiles at various locations to within a few pixels. Note that the vortex is not identified through measurements of the velocity field.

Based on the above background, the trailing edge of the vortex is discerned in Figure 4.2 from the first horizontal (flat) contour level, i.e., C = 50% and z/d = 0.55 at t = 16.7ms. The vortex boundaries are marked by dots in the contour plots. The leading edge of the vortex, where the concentration is higher than the maximum contour level of 70% used to generate the plot, is not visible. The jet continues to contract at t = 24.5 and 33.3ms, as the vortex grows and moves downstream. At t = 50.0ms, the vortex has moved downstream and its effect on the near field has diminished as evidenced by the bulging of the jet near the exit. The vortex is located next in the upper plot at t = 0.0, which coincides with the end of the cycle at t = 58.8. At this instant, the jet contraction near the exit has re-initiated, in preparation for another vortex. Later on, the vortex present in the upper plot at t = 0.0 or 58.8ms moves outside the field of view.

Several features of the vortex interacting with the jet flow are inferred from the contour plots in Figure 4.2. The small spacing between contours near the jet exit signifies large radial concentration gradients, as the jet contracts during the initial stages of vortex formation. The radial concentration gradient outside and downstream of the vortex is also high. Contours with large spacing are seen upstream of the vortex trailing edge. The contour spacing increases with the downstream movement of the vortex. A large contour curvature indicates that the axial diffusion is important throughout the flow

field. An exception is the downstream region after the passage of the vortex, when the contours appear as nearly vertical lines, e.g., for z/d > 2.5 at t = 16.7 and 24.5ms. Another observation is the significant diffusion of helium around the jet tube.

To observe the concentration and velocity fields simultaneously, computational modeling of the helium jet was performed for Case 1. Figure 4.3 shows the computed contours of helium mole fraction. The contours are shown till z/d = 3 in the axial direction to compare with experimental results. In the first plot at t = 0.0ms, small indentations in contour levels are observed near the tube exit (z/d = 0.5). Contour levels at t = 16.7 ms show the presence of a local minimum and maximum, near z/d = 0.9. The computed frequency of oscillations is about 12 Hz compared to the experimental value of 17 Hz. The jet contraction continues at t = 33.3 and 50 ms, as the vortex grows and moves downstream. At t = 66.7 ms, the vortex has moved downstream and its effect on the near field has diminished, as evidenced by the jet bulging near the exit. At this instant, jet contraction near the exit has re-initiated in preparation to form another vortex. The spillage of the helium is observed around the tube with molar concentration of about 10%. All these features were previously observed in Figure 4.2 for the experimental data at the same operating conditions. Even though precise timing between data acquisition was not replicated, a qualitative representation of the concentration field of oscillating cycle was achieved in the computational results.

The computational analysis using commercial CFD code FLUENT provided a variety of output parameters (vorticity, velocity vectors) along with species concentration. The vortex evolution and propagation have been explained by the isoconcentration contours of helium mole percentage. Vorticity distribution provides a

measure of the rotational component of the vortex field. Figure 4.4 shows the contours of the magnitude of vorticity during an oscillation cycle. The vorticity value in Figure 4.4 reaches a maximum at the edge of the vortex identified previously, indicating the extent of rotation of the entrained air into the main jet. The magnitude of vorticity increases as the vortex grows and moves downstream during the cycle.

Figure 4.5 shows the contours of the magnitude of axial velocity throughout the flicker cycle. The velocity profile is parabolic at the injector exit, with a maximum velocity of 1.12 m/s at the center. We observe the buoyant acceleration of the jet in the central regions with velocities of up to 4 m/s at t = 50 ms. This region of buoyant acceleration also coincides with the leading edge of the vortex. At t = 0.0, the velocity is 2 m/s at z/d = 0.5 to 0.7, where the first indentations of vortex are seen. At t = 16.7 and 33.3 ms, the axial velocities are 3 m/s and 4 m/s respectively, at the leading edge of the vortex.

4.1.3 Vortex Structure and Evolution

Figure 4.7 shows helium concentration profiles in the radial direction for several axial locations within the vortex (i.e., the entrainment region as explained earlier) at t = 16.7ms. For clarity, every third data point is indicated by a symbol. The inflection point at z/d = 0.55 pertains to the trailing edge of the vortex with helium concentration of about 55%. Radial profiles at z/d = 0.6, 0.7, and 0.8 show local minimum/maximum attributed to the vortex. The vortex leading edge is located at z/d~0.9. At a given axial location, concentration changes gradually between vortex midpoint (or local minimum) and vortex outer edge (or local maximum) compared to that from the vortex midpoint to the vortex

inner edge, i.e., the radial location matching the concentration at the vortex outer edge. This trend is ascribed to the higher flow velocities in the inner region of the vortex.

Helium concentration distribution in the axial direction is shown in Figure 4.8 for r/d = 0.44, which approximates the mid-radial plane of the vortex. Evidently, the concentration increases from 55% at the trailing edge to 85% at the leading edge of the vortex. The rate of increase in concentration is observed to decrease gradually in the axial direction. Figure 4.9 also depicts the concentration profile at the mid-radial plane of the vortex after it has moved downstream at t = 50.0ms. A separate scale is used for the axial coordinate because the vortex length had nearly doubled. Results show that the axial concentration profiles at t = 16.7 and 50.0ms will overlap with each other if the axial coordinate is normalized by the vortex height. Further insight into the vortex structure is gained from the radial concentration profiles in Figure 4.8 where data in the mid-axial plane of the vortex at t =1 6.7 and 50.0ms are compared. Again, separate scales are used for the radial coordinate to account for the difference in the width of the vortex. Results presented in Figures 4.8 and 4.9 show that the internal scalar structure of the vortex at different times can be matched by a judicious choice of length scales used for normalization.

The vortex shape and location at various times were determined to plot the evolutionary path shown in Figure 4.10. The vortex leading edge could not be located in some cases because of greater measurement uncertainties for r/d < 0.2 and/or concentrations above 85%. The estimated accuracy of the vortex boundaries is less than 0.02d. Although exact details of the vortex could not be obtained, several important features are delineated from the present measurements. Figure 4.10 depicts a small vortex

near the jet exit at t = 16.7ms. Only minor changes in vortex shape and size are observed thereafter. At t = 58.8ms, the vortex length and width are 0.80d and 0.16d, respectively. At all times, the vortex is about 4 to 5 times longer than its maximum width. Figure 4.10 reveals that the vortex moves radially inward during the formative stage (t = 16.7 and 24.5ms), and thereafter, the vortex moves outward, as shown by the outward shift in the vortex direction at t = 58.8ms. Next, the trailing edge of the vortex was tracked to obtain a representation of the vortex convection velocity during its evolutionary path. Results in Figure 4.11 show that the vortex (trailing edge) convection velocity increases rapidly during the formative stage and gradually thereafter.

4.1.4 Oscillating Flow Characteristics

The analysis of the oscillating flow field in this section was performed using 140 schlieren field images acquired in 2.4 seconds. First, the flow structure is described using mean and RMS (root-mean-square) helium mole percentage profiles at several axial locations in Figure 4.12. Near the jet exit at z/d = 0.05, the mean concentration shows a top-hat profile with a finite shear layer thickness. Near the centerline, the helium concentration is not 100% because of the measurement uncertainties as discussed previously. A significant amount of helium has diffused in the radial direction. The jet radius has increased to r/d = 0.65 and the mean concentration at the inside boundary of the tube (r/d = 0.5) has reduced to about 55%. At z/d = 0.2, the shear layer is wider although the jet radius has not changed. This trend continues at z/d = 0.6, where the mean concentration has decreased at all radial locations except in a narrow outer region. Reduced concentration implies an accelerating jet-flow, which is required to satisfy the conservation of helium mass. Flow acceleration is accompanied with an inflow of the

surrounding fluid, which inhibits the growth of the jet in the radial direction. The mean concentration profile at z/d = 1.0 reveals an inflection point at r/d = 0.34. The radial location of the inflection point coincides with the mid-point of the vortex in Figure 4.10. The RMS profiles in Figure 4.12 reveal large fluctuations near the jet exit. The peak RMS concentration of 12% at z/d = 0.05 increases to 18% at z/d = 0.2 and to 26% at z/d = 0.6. The location of the peak RMS concentration shifts inward with the axial direction, which is consistent with contraction of the jet flow during vortex formation. Concentration fluctuations confined to the wake region ($0.4 < r/d < 0.6$) near the jet exit broaden in the axial direction and contaminate most of the flow at z/d = 1.0.

The temporal evolution of the jet flow is depicted next by a series of plots in Figures 4.13 and 4.14. At each axial location, the experimental data are placed sequentially in time to produce these figures. Data are shown for a brief time-interval to closely analyze the radial and axial growths of instability during the oscillation cycle. The time traces in Figure 4.13 show that the oscillations are repeatable at all axial and radial locations. The measurement time at all axial locations in Figure 4.13 is the same because the schlieren data are obtained across the whole field. Thus, the time delay between peaks (or valleys) at different axial locations represents downstream propagation of the instability. The time-interval between two consecutive peaks (or valleys) is the period (T) of the oscillation cycle. An examination of Figure 4.13 yields T~58ms from concentration peaks (or valleys) at different axial locations. This result agrees with the oscillation frequency of 17Hz (or T = 58.8ms) computed using the fast Fourier analysis of angular deflection data. In agreement with mean and RMS concentration profiles in Figure 4.12, the intensity and radial extent of fluctuations are shown to increase in the

axial direction. The surrounding fluid entrains farther into the main jet as the jet progresses in the axial direction. For example, near the jet exit, the 60% concentration curve is located at r/d = 0.5. At z/d = 1.0, the 60% concentration range extends between r/d = 0.25 and 0.5.

Time traces of the helium mole percentage at the specific radial locations of r/d = 0.3, 0.5 and 0.6 are shown in Figure 4.14. Near the jet exit (z/d = 0.05), the flow oscillates in the outer region. The oscillation amplitude increases in the axial direction as the jet core region (r/d = 0.3) is contaminated by the vortex at z/d = 1.0. The measurements suggest a strong coupling between the vortex and the surrounding flow field because r/d = 0.5 and 0.6 are locations outside the vortex path (see Figure 4.10). Next, the time at the peak concentration was found at various axial locations to compute the propagation velocity. The analysis was performed for several radial locations and a typical result is shown in Figure 4.15. Although the temporal resolution was limited to 16.7ms, the results depict a definite trend. The propagation velocity increases in the axial direction, rapidly near the jet exit and gradually in the downstream region. The trend in Figure 4.15 is similar to that in Figure 4.11 for the vortex (trailing edge) convection velocity and provides evidence of strong coupling between the vortex and the surrounding flow field.

4.1.5 Effects of Richardson Number

The Richardson number was changed to delineate the role of buoyancy on flow and instability characteristics. The oscillation period T = 30.3ms (or f = 33Hz) was determined by examining a sequence of five oscillation cycles. The fast Fourier analysis was inapplicable because the sampling rate of 60Hz did not satisfy the Nyquist criterion.

Figure 4.16 shows a sequence of helium mole percentage contour plots arranged in phase to observe the flow structure during an oscillation cycle. The radial contraction of the jet near the exit is observed between t = 0.0 and 6.02ms. The extent of contraction is less severe compared to the high Ri case, as demonstrated by the smaller slope of contour lines. This is interpreted as a slower buoyant acceleration of the main jet at lower Ri, and hence, a reduced inflow of the surrounding fluid contracting the jet. Accordingly, the vortex is expected to form farther downstream. Indeed, in Figure 4.16 for t = 6.02ms, the vortex first appears at z/d = 1.3, compared to z/d = 0.55 for the high Ri case. The vortex forms at approximately the same radial location (r/d = 0.42) for the two cases. Figure 4.16 shows an increase in the size of the vortex as it gets convected downstream. The minimum helium mole percentage inside the vortex is about 70% compared to a value of 55% for the high Ri case. This is interpreted as a direct consequence of the vortex forming at a downstream location, allowing greater diffusion of helium into the shear layer. The inner and outer boundaries of the vortex could not be precisely located because of the measurement uncertainties at high helium concentrations in those regions. An examination of the vortex path reveals that the vortex pushes inward during the formative stages. The vortex (trailing edge) convection velocity plot in Figure 4.17 demonstrates that the vortex accelerates rapidly during the formative stage and gradually thereafter, an observation also made at higher Ri (see Figure 4.11). In spite of the smaller Ri, significant buoyancy effects are present in the jet flow, evidently because the maximum vortex velocity is more than twice the jet exit velocity.

The mean and RMS helium concentration profiles are shown in Figure 4.18. Results show that the jet radius does not change in the axial direction. However, the mean

profile adjusts as the concentration decreases in the inner and increases slightly in the outer portions of the jet. The profile at z/d = 2.4 shows no distinct inflection point at the location of the vortex. This is attributed to the bias introduced by the limited temporal resolution of the measurements; the vortex at z/d = 2.4 was detected only for every 5^{th} cycle. The RMS concentration profiles show minor fluctuations in the wake region of the tube wall. The peak RMS concentrations are small compared to the high Ri case. Peak fluctuations occur in the flow field outside the vortex path. Oscillations contaminate most of the jet core at z/d = 1.0, which is near the vortex formation plane.

4.1.6 Summary

Quantitative RSD was successfully applied to study the scalar flow structure of self-excited buoyant helium jets discharged vertically in air. Time-resolved measurements of helium mole fraction were obtained at temporal resolution of 16.7 ms and spatial resolution of 0.28 mm across whole field of the jet flow. The data were analyzed to identify the vortex size, structure, and evolutionary path, and to understand interactions between the vortex and the oscillating flow field. Peak oscillations occurred in the flow surrounding the vortex. Reduction in buoyancy released at the exit reduced radial contraction of the jet and delayed formation of the vortex. The maximum vortex velocity and peak RMS concentrations were affected by the jet Richardson number. The vortex convection velocity was much higher than the jet exit velocity because of the significant buoyancy effects. Although buoyant jets were investigated in this study under Earth gravity conditions, similar experiments need be performed in microgravity conditions to isolate buoyancy effects on flow structure of buoyancy-dominated and momentum-dominated helium jets exhibiting global flow oscillations. High oscillation

frequencies of these jets however require a schlieren apparatus with high-speed imaging capability.

4.1 Table 1: Experimental test matrix

Case	d, mm	Re	Ri	f, Hz
1	31.8	147	5.0	17
2	19.1	130	1.8	33
3	10.5	1500	0.002	425
4	10.5	1200	0.003	415
5	10.5	1000	0.005	280
6	10.5	800	0.008	215
7	14.5	1200	0.008	390
8	14.5	1000	0.01	160
9	14.5	800	0.02	120
10	14.5	600	0.04	90
11	19.05	800	0.05	85
12	19.05	600	0.08	65
13	19.05	400	0.18	40
14	19.05	200	0.72	28

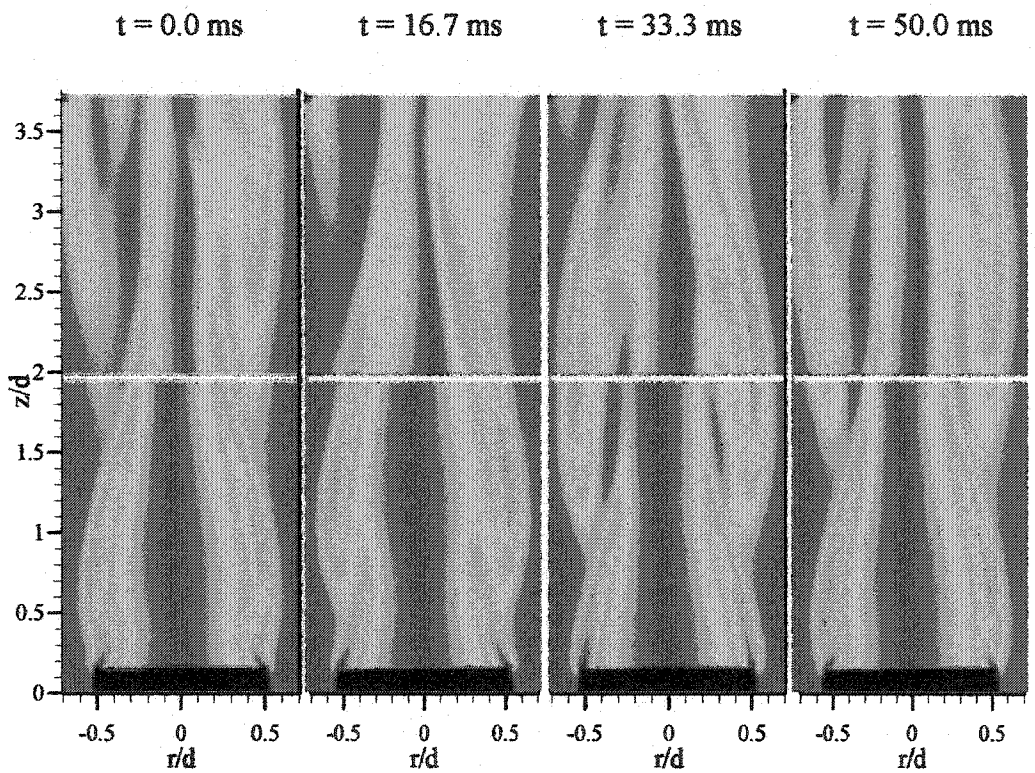


Figure 4.1: Rainbow schlieren images during an oscillation cycle (Case I).

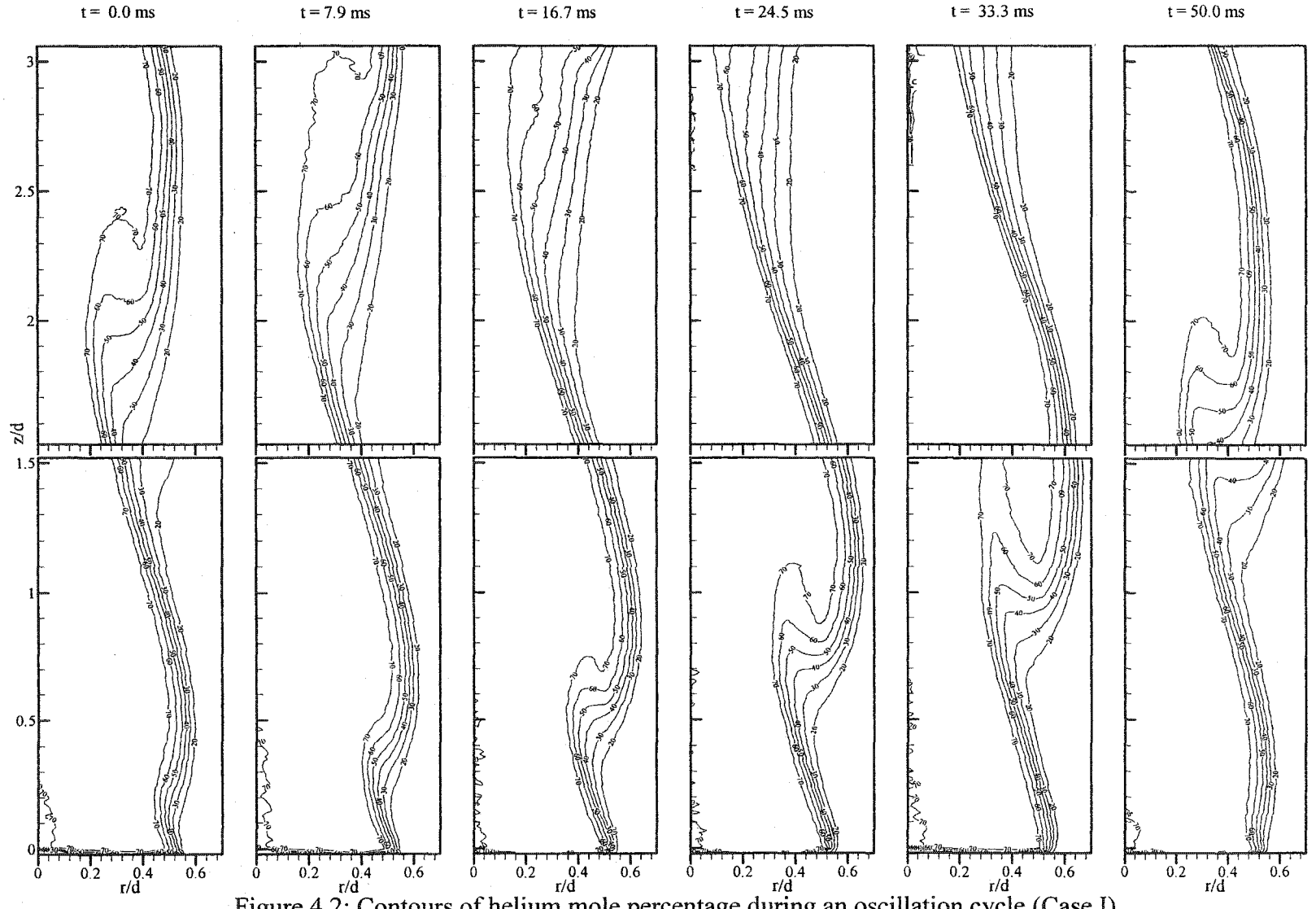


Figure 4.2: Contours of helium mole percentage during an oscillation cycle (Case I).

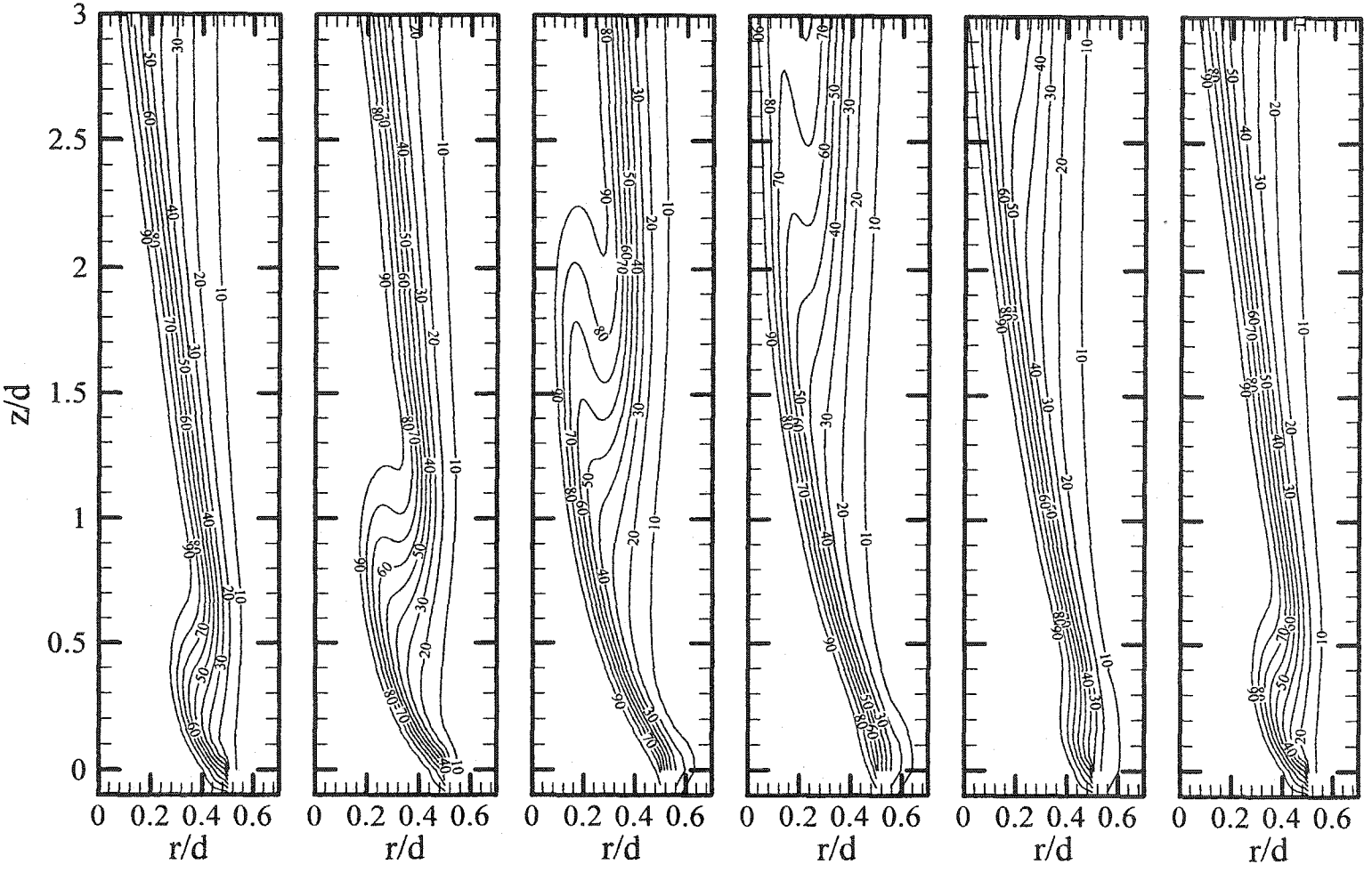


Figure 4.3: Contours of helium mole percentage during an oscillation cycle (Computational case, Case I).

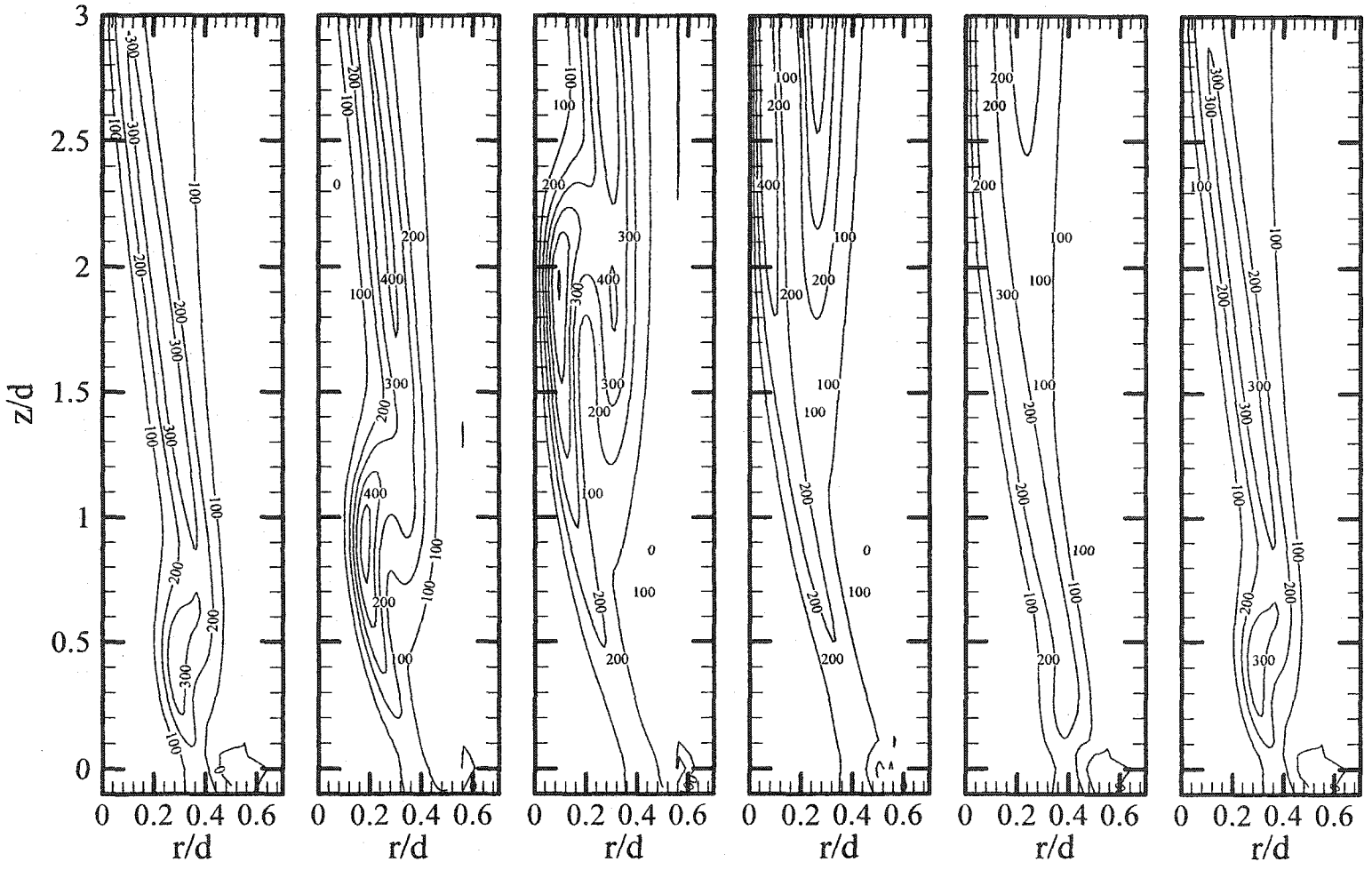


Figure 4.4: Contours of vorticity during an oscillation cycle (Computational case, Case I).

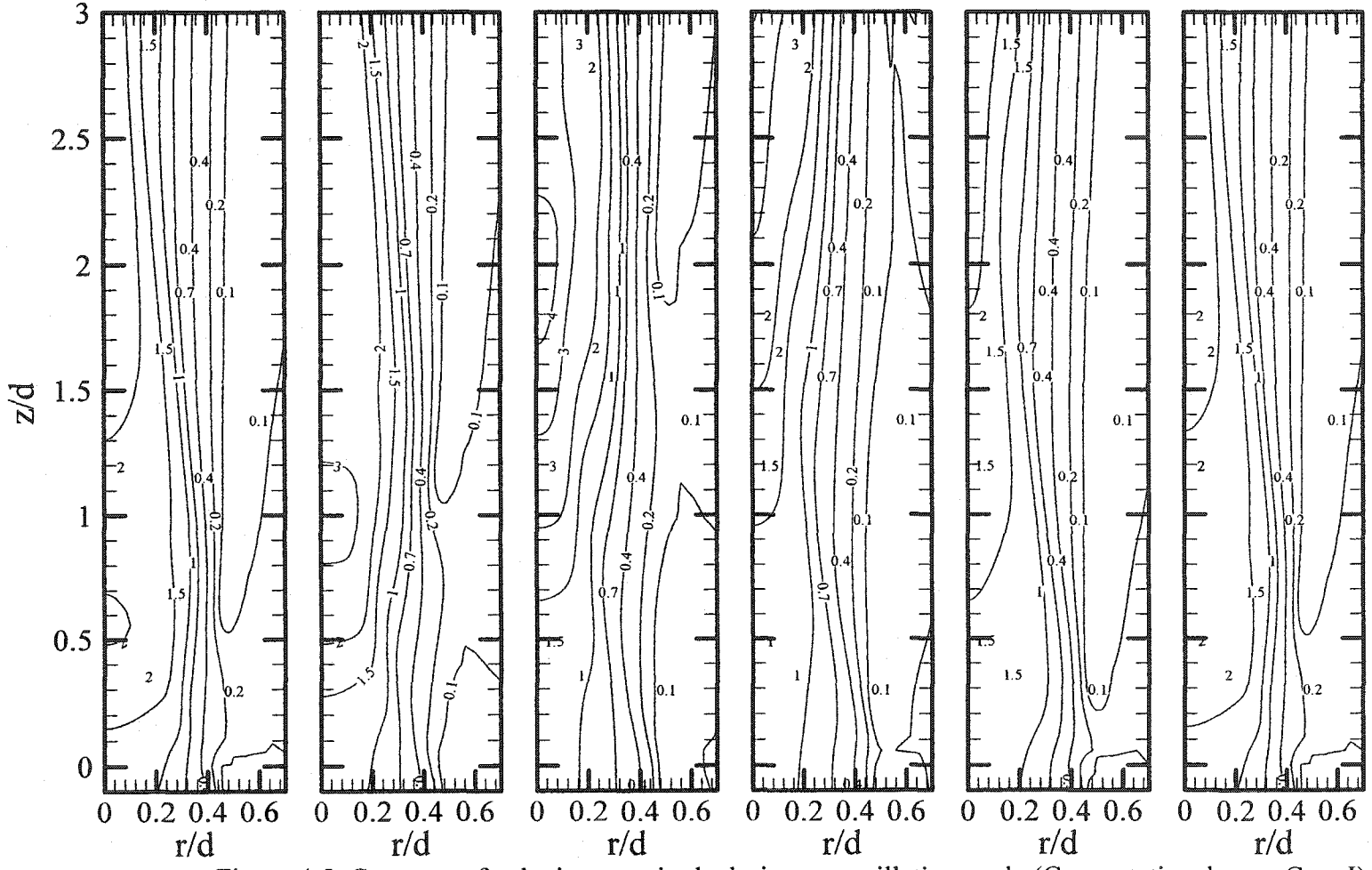


Figure 4.5: Contours of velocity magnitude during an oscillation cycle (Computational case, Case I).

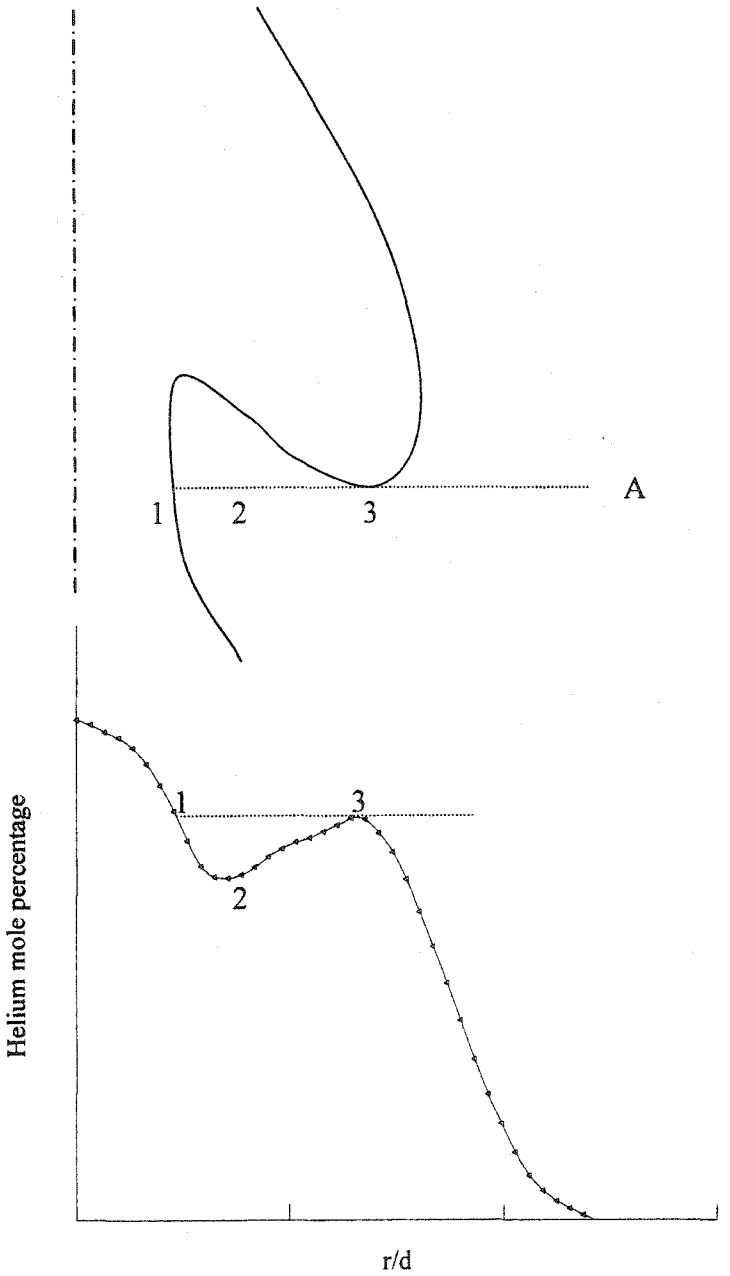


Figure 4.6. Schematic of the vortex and a typical helium concentration profile.

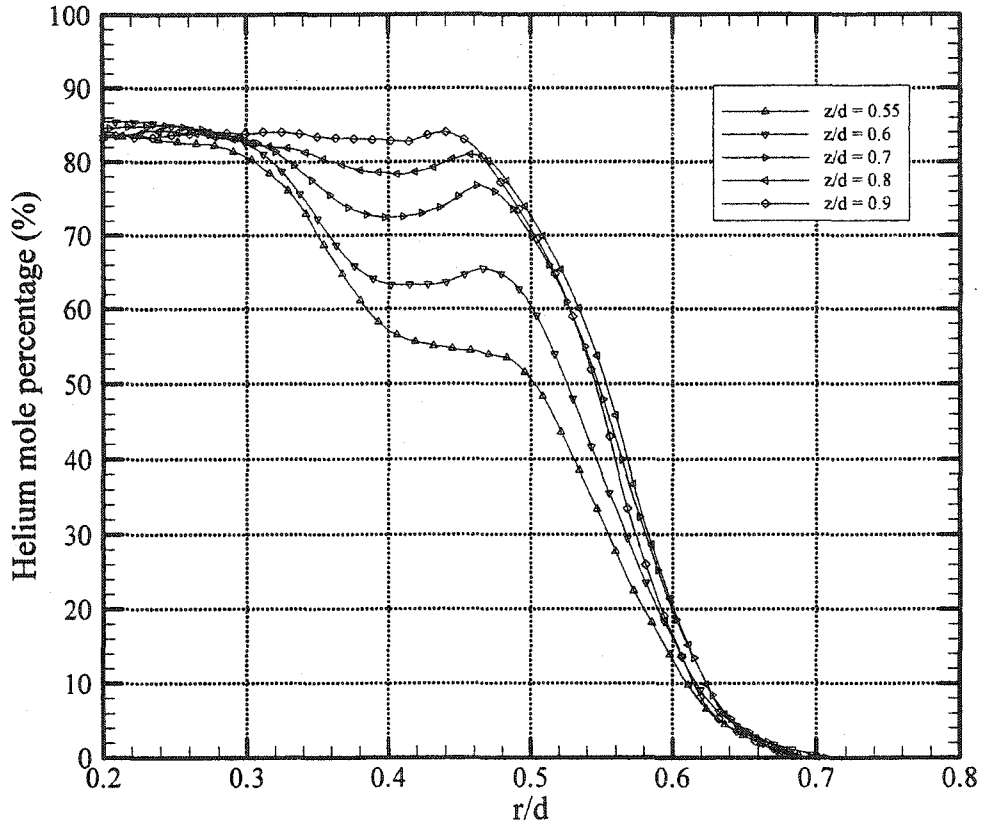


Figure 4.7. Profiles of helium mole percentage in the vortex region at t=16.7ms.

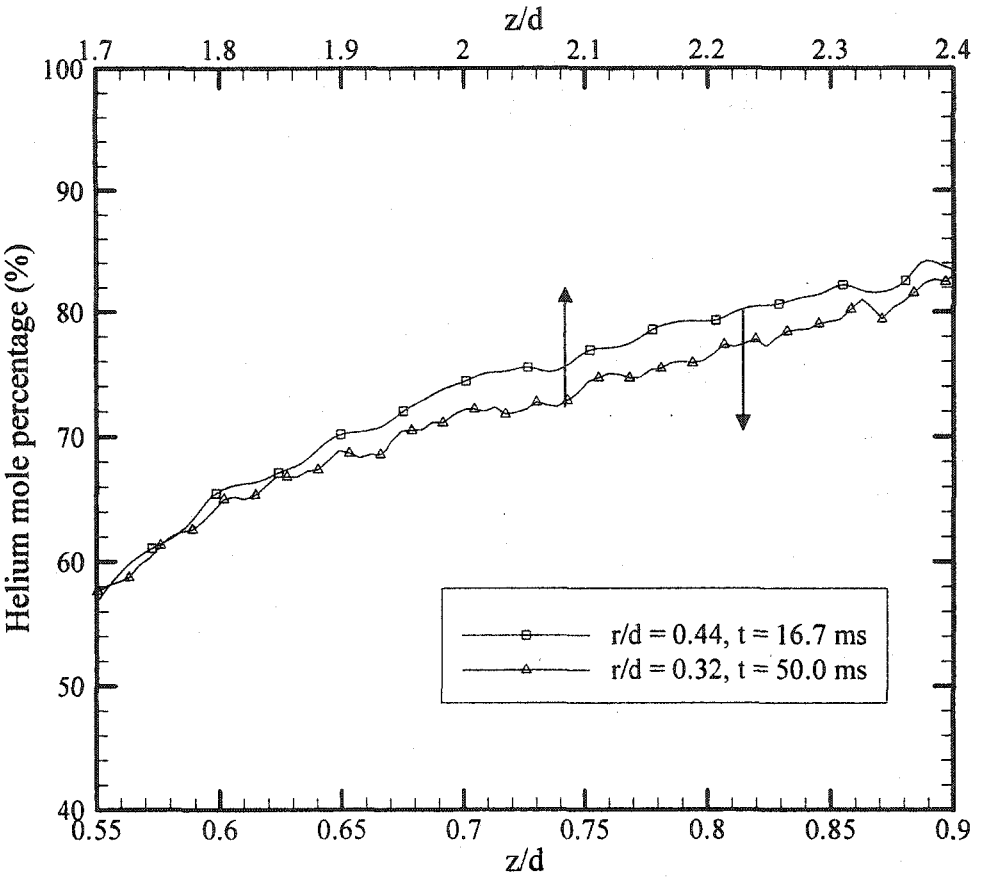


Figure 4.8: Profiles of helium mole percentage at the mid-radial plane of the vortex.

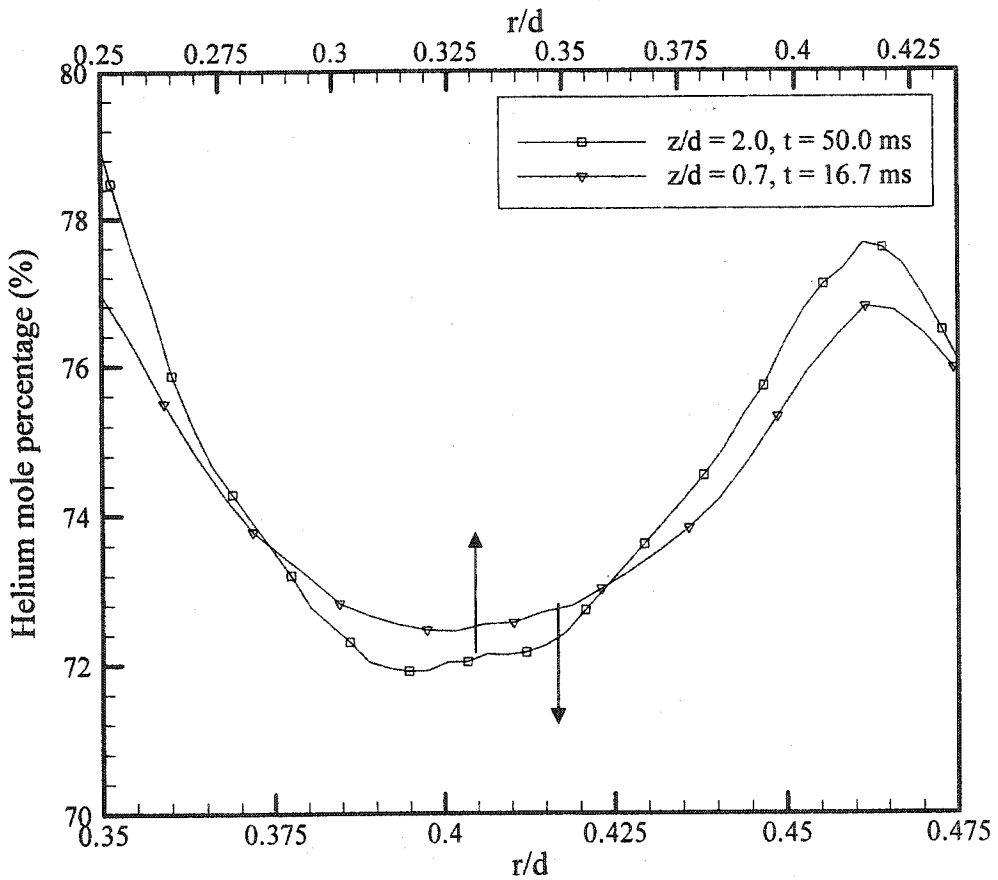


Figure 4.9: Radial profiles of helium mole percentage at the mid-axial plane of the vortex.

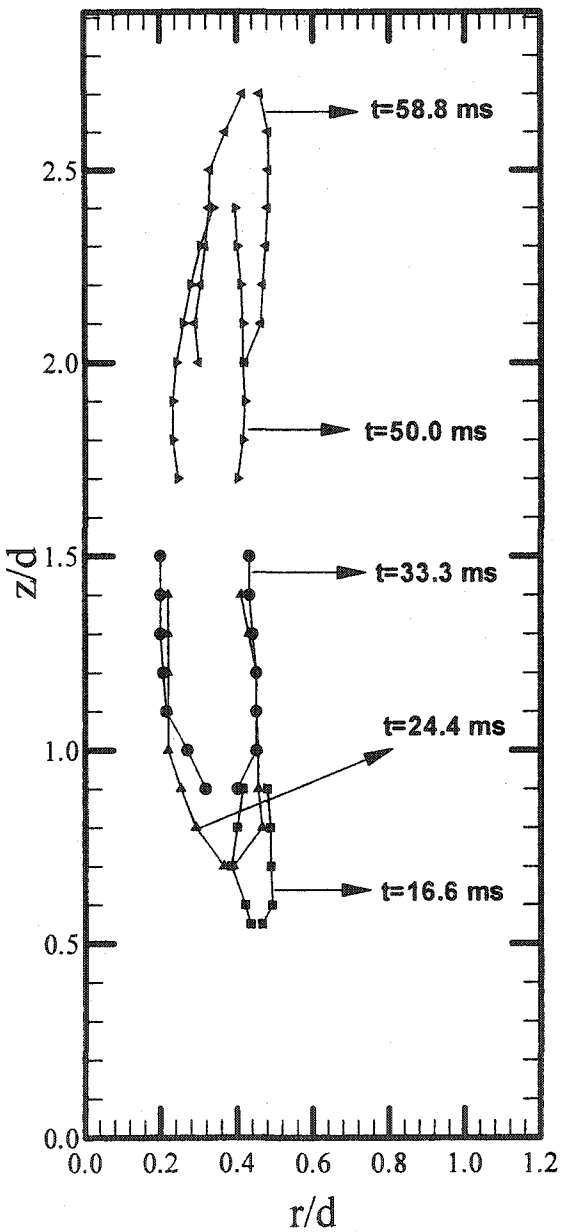


Figure 4.10: The shape and evolutionary path of the vortex.

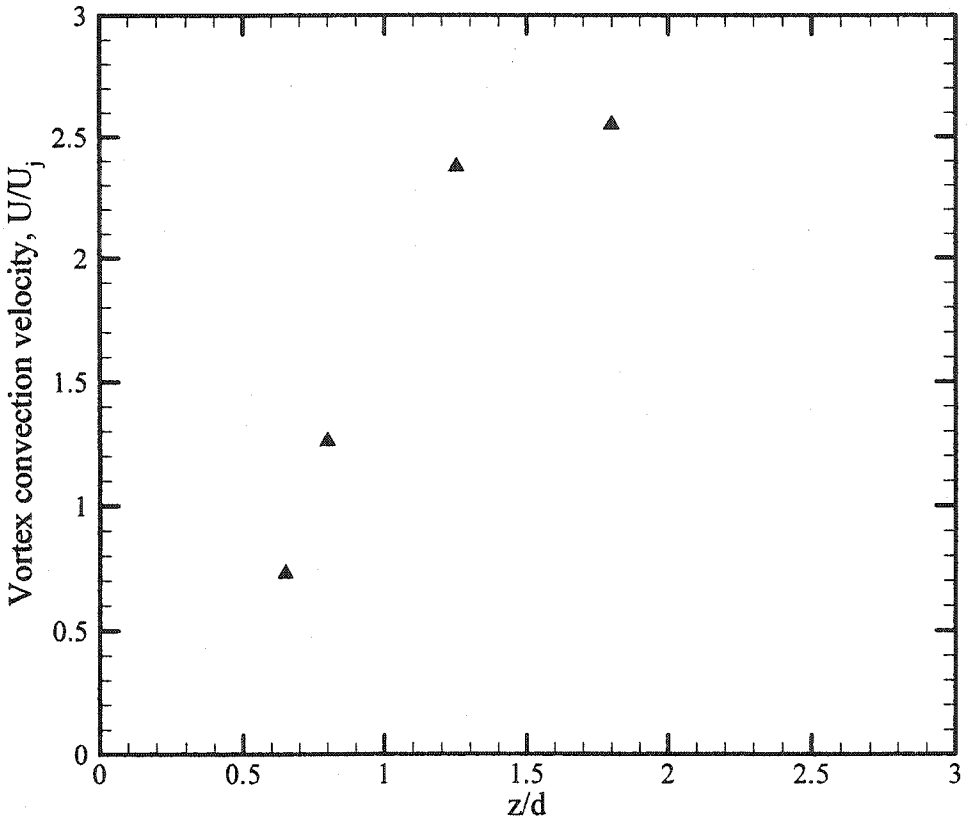


Figure 4.11: Variation of vortex (Trailing edge) convection velocity with axial coordinate (Case I).

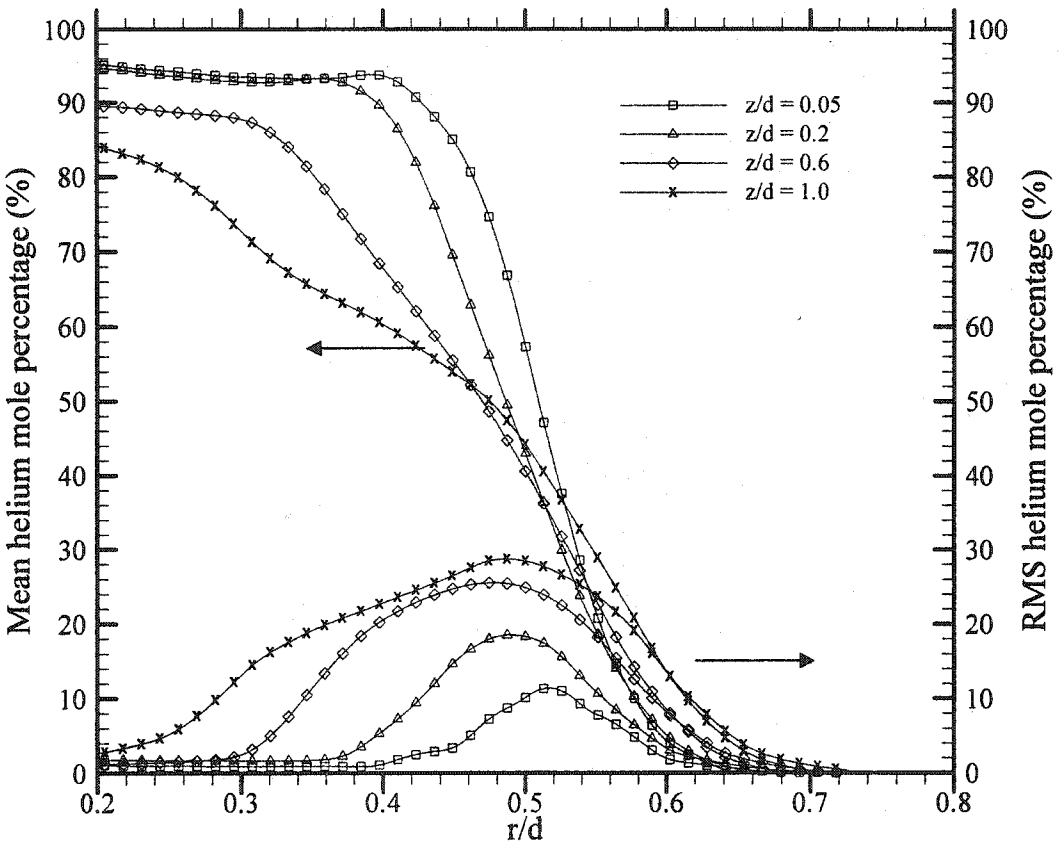


Figure 4.12: Mean and RMS helium mole percentage profiles at various axial locations (Case I).

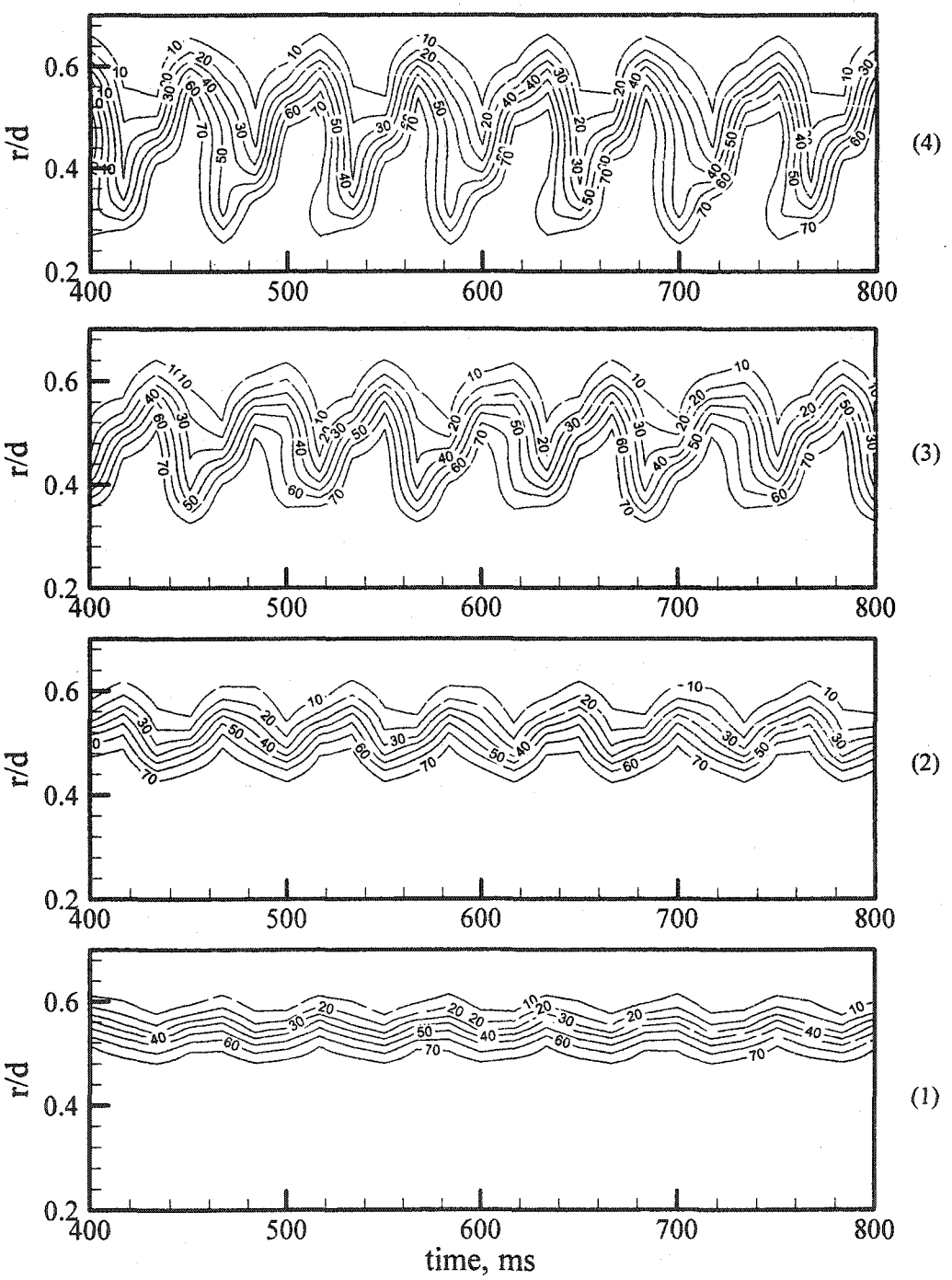


Figure 4.13: Temporal evolution of helium mole percentage at various axial locations; (1) z/d=0.05, (2) z/d=0.2, (3) z/d=0.6, and (4) z/d=1.0.

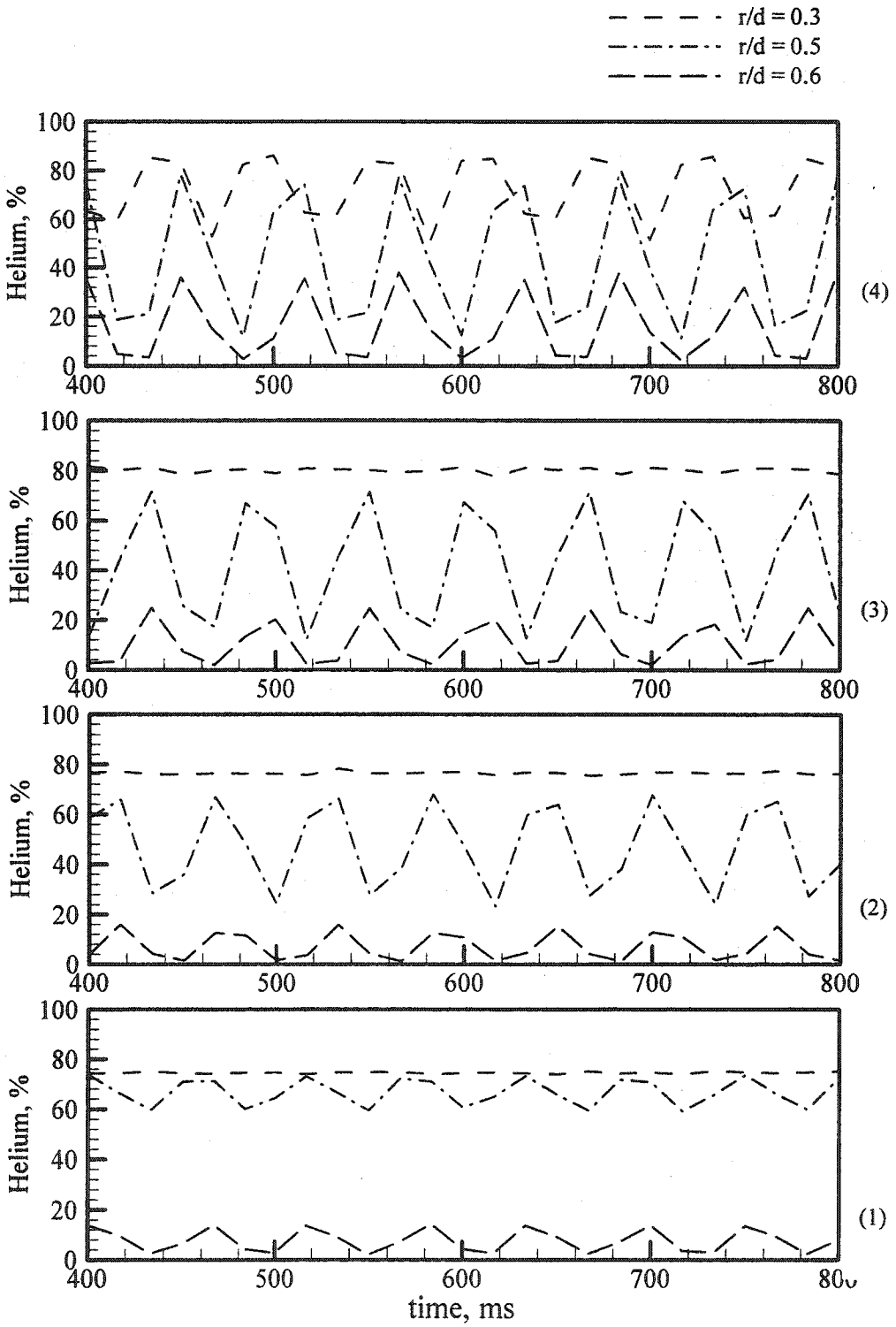


Figure 4.14: Temporal evolution of helium mole percentage at various axial locations; (1) z/d=0.05, (2) z/d=0.2, (3) z/d=0.6, and (4) z/d=1.0.

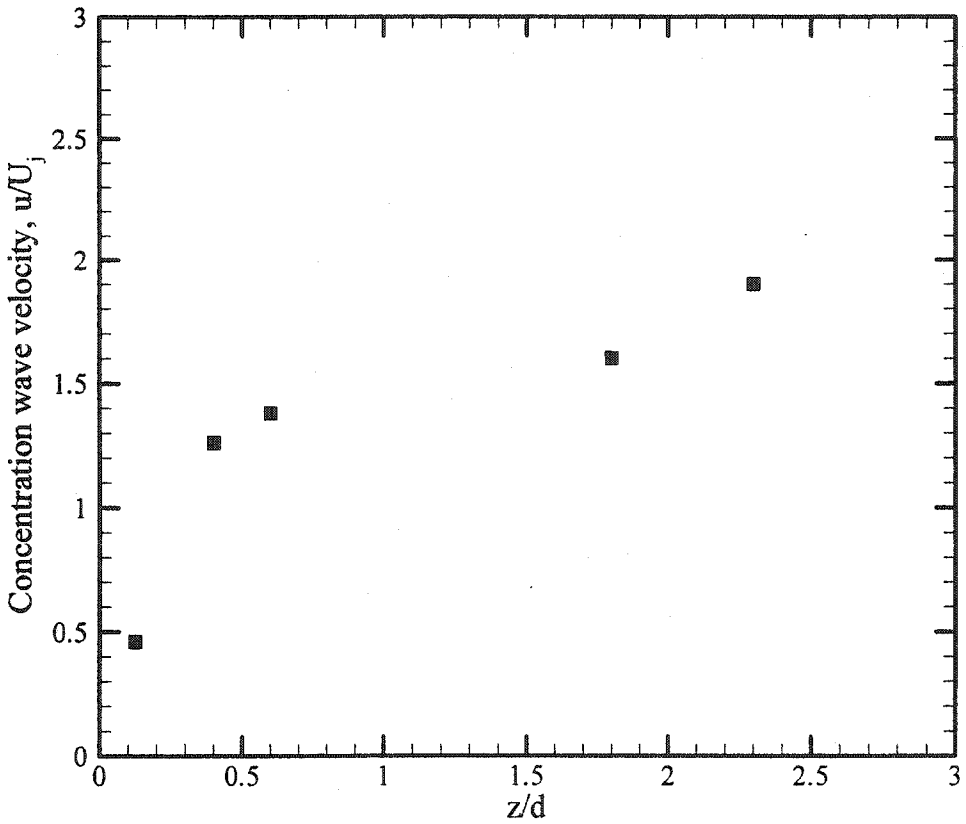


Figure 4.15: Variation of concentration wave velocity with axial coordinate

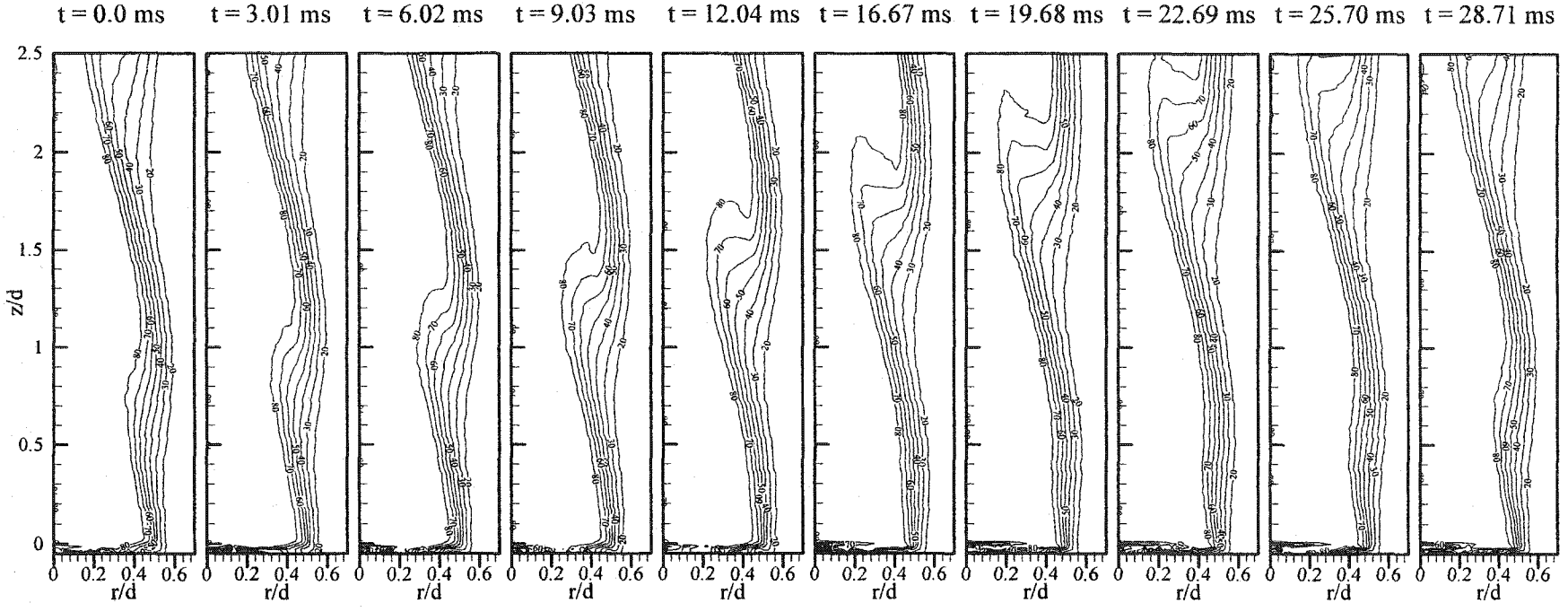


Figure 4.16: Contours of helium mole percentage during an oscillation cycle (Case II).

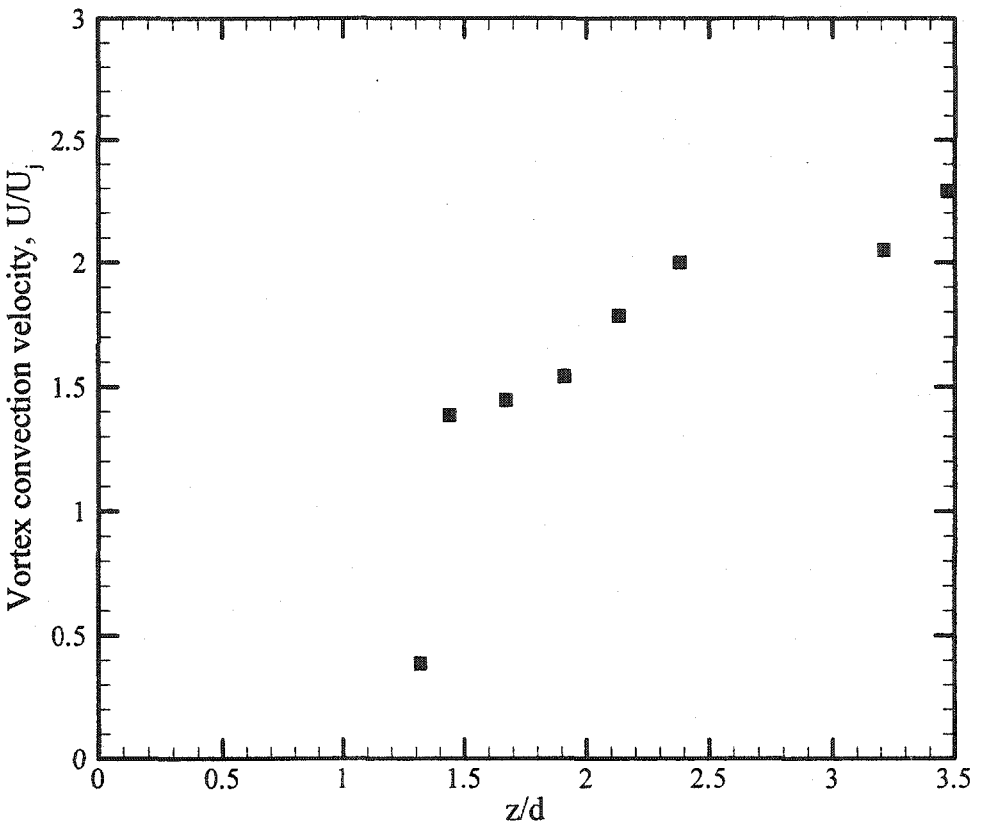


Figure 4.17: Variation of vortex convection velocity with axial coordinate (Case II).

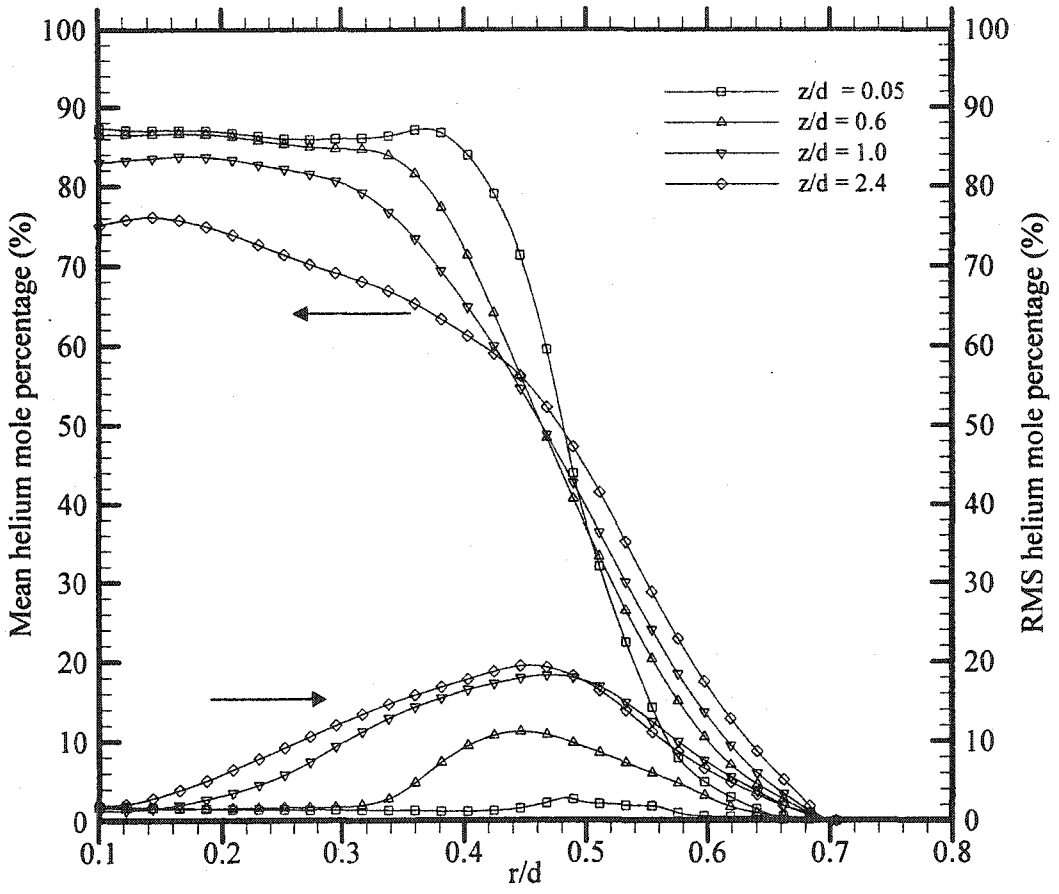


Figure 4.18: Mean and RMS helium mole percentage profiles at various axial locations (Case II).

4.2 Buoyancy Effects in the Near Field of Low-Density Jets

To examine the buoyancy effects on oscillating flow structure of low density jets, microgravity experiments in buoyancy-dominated and momentum-dominated flow regimes were deemed necessary. To accomplish this, a series of experiments were performed on axisymmetric oscillating helium-air jets under Earth gravity and microgravity conditions in the range of Reynolds numbers from 200 to 1500 and Richardson numbers from 0.002 to 1.0. The test Cases 3-14 are listed in Table 4.1.

4.2.1 Schlieren Visualization

To facilitate a visual understanding of the buoyancy effects on the oscillating flow, flow visualization is presented in the form of rainbow schlieren images for Cases 3 and 6 in Figure 4.19 under Earth and microgravity conditions. The laminar shear layers remain axisymmetric until 2.5 diameters downstream of the jet exit and hence, only one side of the jet flow structure is shown till z/d = 2.0. The tube is visible as a black region in all the images. In both cases, an increase in axial diffusion and radial expansion in the absence of buoyancy forces is noted by observing gradual color variation in microgravity. To understand the dynamics of the oscillating instability under gravitational change, concentration measurements are needed in the whole field. RSD facilitates acquisition of spatio-temporal quantitative data on the whole field of view in the jet flow. Figure 4.20 shows isoconcentration contour plots of helium mole percentage in Earth and microgravity conditions for the two cases presented in Figure 4.19. Only one side of the jet is shown owing to the symmetry observed until about z/d = 2.0. The curvature in the interior and exterior contour levels at t = -0.1ms (negative sign indicates prior to the

initiation of microgravity) is caused by entrainment of ambient air into the jet core. This entrainment is manifested throughout the oscillation cycle, giving rise to varied curvature levels at successive times in a repeatable fashion. Details of the dynamics of the wavy contours in an oscillation cycle have been discussed in the previous chapter for buoyant jets in Earth gravity. The waviness disappears gradually after the microgravity condition is initiated (t = 0.1 to 2.1s). The isoconcentration contours are straight lines, reminiscent of a non-buoyant laminar jet after steady microgravity conditions are reached at t = 2.1s. The small spacing between contours in Case 6 signifies the presence of large radial concentration gradients when compared to Case 3 owing to an increase in the jet momentum flux or Re. The large change in jet flow structure in microgravity in both cases prompts the need to observe the flow structure details after removal of gravitational forcing. This will also provide an idea about the time needed by the jet flow to attain steady microgravity conditions.

The evolution of the flow structure during the change from Earth gravity to microgravity is shown in Figures 4.21 and 4.22 by time traces of helium mole percentage for four cases at two axial locations z/d = 1.0 and z/d = 2.0 respectively. The microgravity period starts at 0.0s in each case. The time traces show that a repeatable oscillatory mode exists and persists in Earth gravity and for varying amount of time after removal of buoyancy. Spatial amplification of the oscillation intensity is observed by noticing the increased radial extent of oscillation amplitude into the jet core region in Figures 4.21 and 4.22 for all cases. The gradual damping of the amplitude of oscillations in microgravity is seen in Figures 4.21(a)-(c) and Figures 4.22(a)-(c) before the jet attains steady conditions. The time taken for the oscillating flow to attain steady conditions has

increased with decrease in Ri. Further, the time taken to attain steady conditions in microgravity for the case with Ri = 0.008 in Figures 4.21(d) and 4.22(d) is greater than 1.2s. Jets with Ri < 0.008 would take longer to attain steady microgravity conditions, owing to the high jet momentum flux (Re > 1500).

4.2.2 Temporal Evolution

Space-time plots of helium concentration were constructed to show the evolution of the concentration waves along the radial direction in Earth and microgravity conditions. The plots were developed by extracting data at a specified axial location on one side of the jet flow (the jet is axisymmetric) from the set of 2728 images separated by interval of 0.001s.

Figures 4.23-4.25 show the temporal evolution of helium concentration for different cases in Earth (bottom) and microgravity (top) conditions at three axial locations, z/d = 0.5, 1.0 and 2.0. Helium concentration levels shown in the radial direction range from 20 to 70 percentage in all cases. Plots are shown for 0.1s duration in Earth gravity and microgravity, the period in microgravity being the time towards the end of the drop. In Figure 4.23(a), we observe the evolving oscillating structure for the case with Ri = 0.72 and Re = 200 to be highly repeatable with the appearance of successive crests and troughs. The time period of the concentration wave is the time elapsed between two successive crests or troughs and is approximately equal to 0.04s which corresponds to oscillating frequency of 25 Hz. This value matches well with a frequency of 28Hz obtained by FFT analysis of angular deflection data. The spatial extent of oscillation amplitude is determined by observing the 70% concentration wave, ranging from 0.3d to 0.4d in Earth gravity. The spatio-temporal plot in microgravity reveals the absence of any

oscillatory instability. Fluctuations are completely absent in the concentration waves in microgravity making the jet resemble a steady laminar jet. In addition, the 20% concentration wave is shifted from 0.54d in Earth gravity to 0.62d in microgravity indicating radial expansion of the jet in the absence of buoyancy forces. Figure 4.23(b) shows the temporal evolution for case with Ri = 0.05 and Re = 800. The amplitude of the oscillating flow has increased with decrease in the Richardson number. A widening of the shear layer has taken place in Earth gravity compared to that in Figure 4.23(a) for higher Ri. The spacing between contour levels has narrowed, indicating that the entrainment rates have decreased for higher momentum (Re = 800) jets. In microgravity, the jet is steady and has expanded until r/d = 0.65. The damping of the oscillatory mode observed in microgravity for lower Ri is reiterated by the temporal evolution plots for the cases with Ri = 0.04 and 0.01 in Figures 4.23(c) and 4.23(d), respectively. Further downstream at z/d = 1.0 and 2.0, an increased oscillation amplitude is observed in Earth gravity and the oscillating flow has been damped progressively by the absence of buoyancy forces in microgravity for all cases as shown in Figures 4.24 and 4.25.

To gain further understanding of the varying oscillation intensity in the radial and axial directions, time traces of helium mole percentage at specific radial locations (r/d = 0.3, 0.5 and 0.6) for different Ri are shown in Figures 4.26-4.28; these are the same locations shown in Figures 4.23-4.25. Near the jet exit (z/d = 0.5), the flow oscillates predominantly in the shear layer region in Earth gravity. The concentration fluctuation wave at all radial locations is completely damped in microgravity in Figs. 4.26(a) and (c). For Ri = 0.008, the oscillations persist in microgravity at a level comparable to that in Earth gravity as seen from Figure 4.26(d). The oscillation amplitude increases in the axial

direction at all radial locations in Earth gravity as evident from Figures 4.27 and 4.28. The oscillations become significant in the jet core region (r/d = 0.3) for all cases in Earth gravity. The intensity of oscillations continues to decrease in microgravity for all cases at this axial location (z/d = 2.0).

4.2.3 Power Spectra

In this section, an analysis of power spectra of angular deflection data of the oscillating flow field is presented. The power spectra were generated at different radial and axial locations by the application of fast Fourier transform of the angular deflection data in schlieren images from an ensemble 256 images. As mentioned earlier, there was 2.2 seconds of data available in microgravity. Within the available camera memory buffer, it was possible to acquire at least 500 images in Earth gravity and 2200 in microgravity. The data in microgravity were acquired towards the end of the drop process minimizing residual buoyancy effects.

The power spectra of the angular deflection data for Re = 200 and Ri = 0.72 is shown in Figure 4.29 in Earth gravity (left) and microgravity (right) at different axial and radial locations. A dominant peak corresponding to a frequency of 28 Hz is observed in Figure 4.29(a) under Earth gravity conditions. The frequency corresponding to the dominant peaks at all locations in Earth gravity remains the same (at 28 Hz) indicating that the oscillatory mode is independent of the streamwise and radial locations. The same cannot be said about the spectral power intensity as it varies throughout the flow field. The spectra in microgravity are in a broadband mode, devoid of any characteristic peak at marginal power. The absence of oscillations in microgravity shows that the oscillatory mode in Earth gravity was definitely buoyancy-induced. The decay of self-excited

oscillations in microgravity is not limited to the near field of the jet exit as evidenced by the spectra at r/d = 0.5 and z/d = 2.0. The spectral power in the shear layer (r/d > 0.4) is about an order of magnitude higher than the level observed at other radial locations (r/d < 0.4). Unlike the velocity spectra of Kyle and Sreenivasan (1991), the angular deflection spectra show that the amplitudes of the fluctuations are high in the potential core.

Figure 4.30 shows the power spectra at z/d = 1.0 for four test cases with varying Richardson number in Earth gravity and microgravity. We note that the oscillation frequency in Earth gravity increases from 28 to 85 Hz when Ri decreases from 0.72 to 0.05. The disappearance of the spectral peaks in microgravity for Ri = 0.72 and 0.18 in Figures 4.30(a)-(c) indicates the decay of the oscillatory mode in the absence of buoyancy forces. The spectral power levels in microgravity are an order of magnitude lower than those observed in Earth gravity for these Ri, indicating the gradual decay in the amplitude of the oscillation mode. Any dominant spectral peak can be characterized by a quality factor Q defined as $Q = f_0 / \Delta f_0$, where f_0 is the peak frequency at a spectral power P_0 and Δf_0 is the frequency difference where the corresponding spectral level has decreased to $P_0 / 10$. This formulation was employed previously by Kyle and Sreenivasan (1992) and Raynal et al. (1996) for analysis of velocity spectra in variable density jets. The calculated quality factor in Earth gravity for the cases in Figs. 4.31(a)-(d) shows a monotonic increase from 2.8 to 8.5. The quality factor in microgravity could not be calculated from Figs. 4.30(a)-(c) due to the presence of broadband noise that is devoid of any unique spectral peak. However, the quality factor decreased to 6 in microgravity for Ri = 0.05 in Figure 4.30(d) compared to the value of 8.5 in Earth gravity.

Figures 4.31-4.32 and 4.33-4.36 show the power spectra for decreasing Ri at different axial planes with d = 14.5mm and 10.5mm, respectively. The spectra in Figure 4.31 are shown at the axial plane z/d = 1.5. Results show that oscillation frequency increases (90-390 Hz) with a decrease in jet Richardson number in Earth gravity. The spectral peaks in Earth gravity are greater than the corresponding ones in microgravity by an order of magnitude. In addition, the quality factor shows a decrease of more than 100% for the cases in Figure 4.31(a)-(c) in microgravity. The damping of the oscillatory mode in the absence of buoyancy forces observed previously at moderate Ri (0.72 - 0.05) occurs for even lower Ri (0.04 - 0.008). The trend continues in Figures 4.33-36 where the spectra corresponding to the lowest Ri (0.008 - 0.002) are shown in the shear layer for different Ri and different axial locations. The observed lower spectral peaks and increased broadband noise are due to the rise in intensity of small-scale turbulence with increasing jet Re (800 - 1500) and higher frequencies (215 – 400 Hz). The spatial amplification of the fluctuations in the oscillatory mode is inhibited by the higher jet momentum flux, making the jet parallel before it undergoes transition to turbulence. The spectra show development of dominant sideband peaks in microgravity for Ri < 0.005.

The initial streamwise development of power spectra for the momentum-driven flow at Re = 1500 and Ri = 0.002 is shown in Figure 4.36 for Earth gravity and microgravity conditions. The jet undergoes transition to turbulence after z/d > 1.7. In Earth gravity, a discernible peak is observed at a frequency of 400 Hz in the power spectra at all axial locations. Similar peaks are observed in the power spectra in microgravity conditions. The spectral power has decreased considerably at all axial locations, indicating that the damping of the oscillatory mode in microgravity continues

even at Ri = 0.002. Previously, we observed the peak corresponding to Earth gravity conditions in buoyancy-driven flows to diminish in microgravity significantly. A similar trend of diminishing intensity of oscillations is also observed for momentum-dominated jet flows. However, the decay of oscillations has been considerably delayed. The jet momentum being higher, we expect the jet to take a longer time to attain steady flow conditions in microgravity environment. In the past, the instability in momentum-driven flows has been attributed only to the jet momentum thickness, jet exit diameter and density ratio. However, from spectra at lower Ri, we observe that the oscillating structure has been affected by the removal of buoyancy.

4.2.4 Peak Power Plots

The plots of power spectra show buoyancy effects on the amplitude of oscillations in the shear layer (r/d = 0.5) at different Ri (0.72-0.002). In momentum-driven flows, the instability is speculated to originate in the potential core (Monkewitz and Sohn, 1988). Spectral power has decreased considerably in the absence of buoyancy forces at specified radial and axial locations in the power spectral plots. To quantify the buoyancy effects in the radial direction, the maximum power corresponding to the dominant peak from the power spectra at a specified axial location was plotted against the radial coordinate resulting in what we call a "peak power" plot. Peak power plots in three data samples corresponding to Earth gravity (t = 0.0-0.26s), initial (t = 0.86-1.11s) and final periods (t = 1.96-2.2s) in microgravity are shown in all the plots.

Figures 4.37 and 4.38 show peak power variation for jet exit Richardson numbers ranging from 0.72-0.05 at two axial locations. We observe that the peak power in Earth gravity for Ri = 0.72, 0.18 and 0.02 is greater than that in microgravity by several orders

of magnitude in the shear layer region (0.2 <r/d <0.6) of the jet. For Ri = 0.05 in Figure 4.38, we observe that the peak power in the initial and final stages of microgravity is significant and comparable to the peak power in Earth gravity for r/d < 0.5. At r/d ≈0.58, the peak power shows a local maximum in Earth gravity for all cases and it is greater than the peak levels in microgravity by an order of magnitude. This shows that buoyancy effects become important in the shear layer i.e., in the annular region surrounding the jet, where the velocity and density gradients are large. In addition, the peak power shows a slight decrease from the initial to final periods in microgravity, indicating that the jet flow has not reached steady flow conditions in microgravity. This implies that 2.2 seconds of available microgravity time is not sufficient to study the damping effects of buoyancy effects on the oscillating flow structure for very low Ri.

The gradual decreasing trend in the peak power of the shear layer spectra from Earth gravity to microgravity continues for lower Ri ranging from 0.04 to 0.008 as shown in Figures 4.39 and 4.40. The decay of peak power in microgravity for Ri = 0.04 and 0.02 is evident by the remarkable decrease in the peak power from Earth gravity to microgravity. Note that the peak power in the potential core region (r/d < 0.2) is comparable in Earth gravity and microgravity periods. The gradual damping effect of microgravity on the oscillating jet structure in the shear layer further reaffirms the presence of residual buoyant effects and the insufficient time available for the jet flow to adjust and stabilize in 2.2s drop tower. Figures 4.41 and 4.42 show the peak power variations for experiments with the lowest Ri (0.008-0.002). The peak power increases with an increase in Re and a decrease in Ri in Earth gravity as shown in Figures 4.39 and 4.41. The peak power variations for all cases in Figure 4.41 are confined to a smaller

region ($0.4 < r/d < 0.6$). A gradual decrease in peak power is observed for all cases. The region of peak power becomes narrower for lower Ri in Figure 4.43 with the damping of the amplitude of the oscillations occurring in $0.48 < r/d < 0.58$ for Ri = 0.002 and Re = 1500 in microgravity. All the peaks correspond to the 400 Hz frequency observed in the power spectra plots. The gradual reduction in peak spectral power in microgravity shows that buoyancy affects the oscillating jet structure of momentum-dominated low-density jets and in particular, the jet shear layer region.

4.2.5 Summary

RSD experiments conducted on vertical helium jets undergoing gravitational change in a microgravity environment have revealed that buoyancy affects near field flow structure in both buoyancy-dominated and momentum-dominated flow regimes. Power spectra plots of angular deflection data reveal substantial damping of the oscillation amplitude in microgravity at low Richardson numbers (~0.002). Radial variation of the frequency spectra and time traces of helium concentration revealed the importance of gravitational effects in the jet shear layer region.

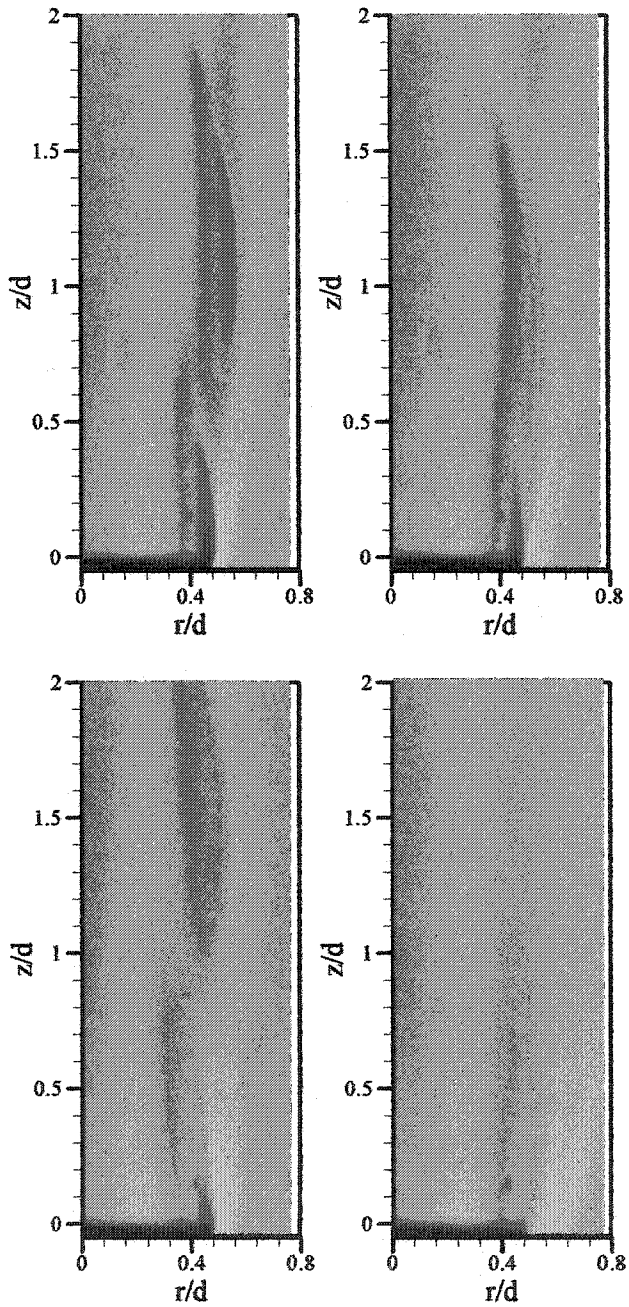


Figure 4.19: Rainbow schlieren images in Earth gravity (left) and microgravity (right) for,

(a) Re = 200, Ri = 0.72 (bottom),

(b) Re = 800, Ri = 0.05 (top).

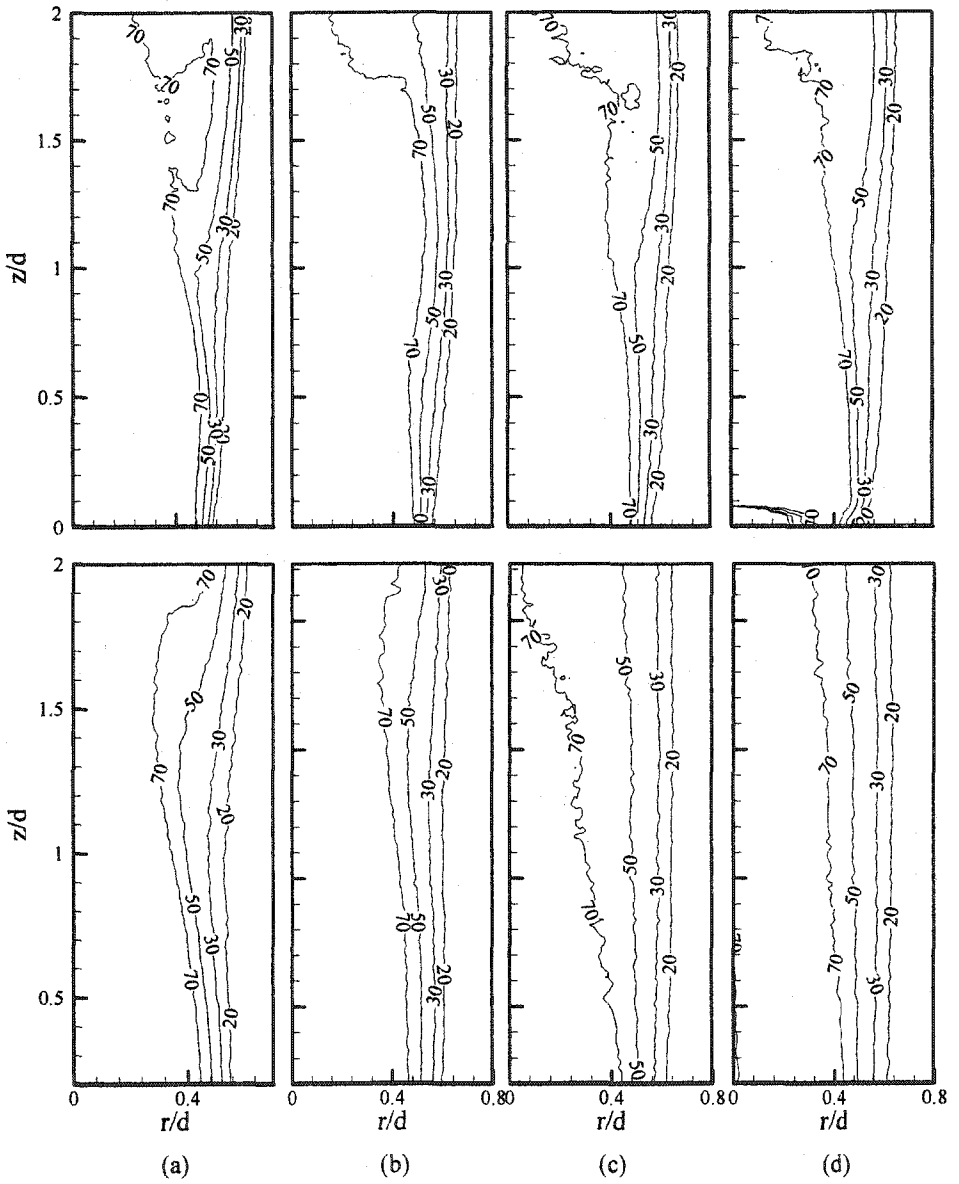


Figure 4.20: Instantaneous helium mole percentage contours in Earth gravity and microgravity for, (1) Re = 200, Ri = 0.72 (bottom) and (2) Re = 800, Ri = 0.05 (top) at (a) T = -0.1s, (b) T = 0.1s, (c) T= 1.1s, (d) T = 2.1s. T= 0.0s denotes the initiation of microgravity.

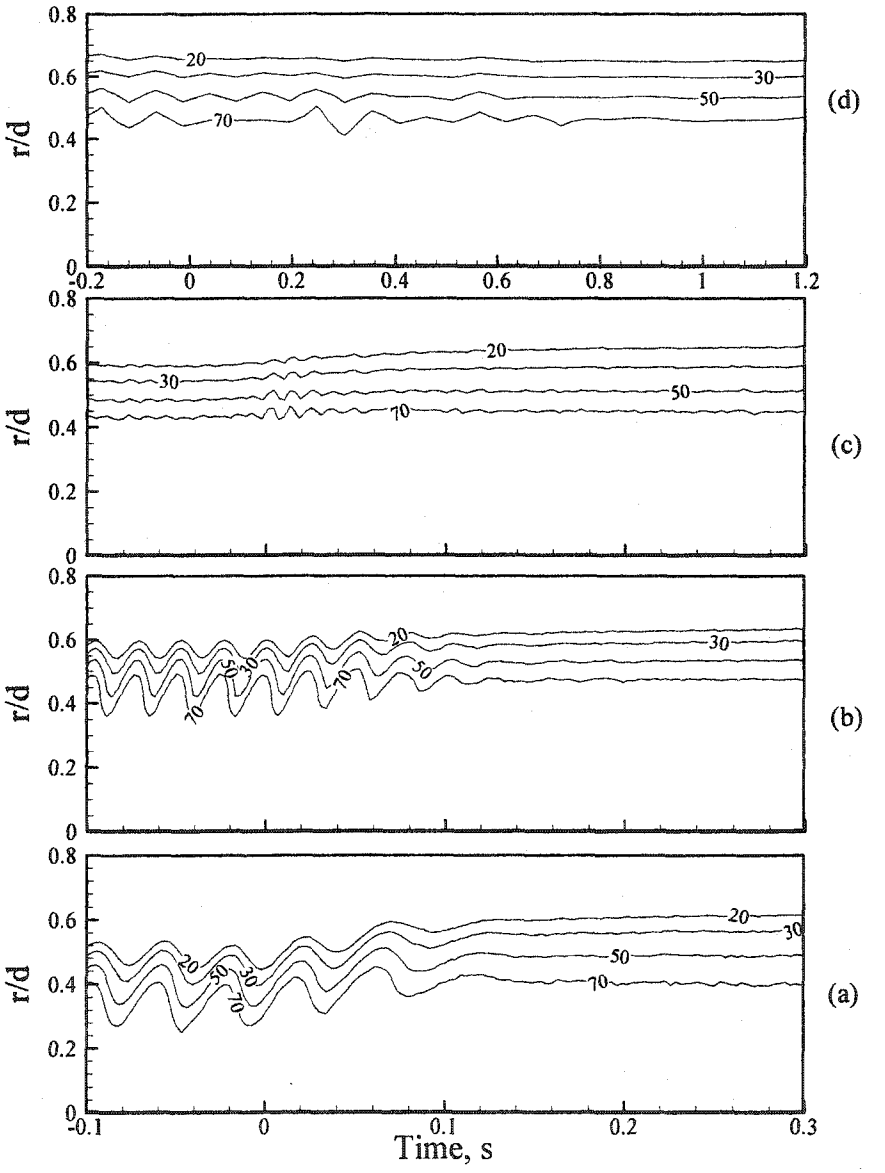


Figure 4.21: Change from Earth gravity to microgravity for varying Ri at z/d = 1.0 for, (a) Re = 200, Ri = 0.72, (b) Re = 800, Ri = 0.18, (c) Re =1200, Ri = 0.03 and (d) Re = 800, Ri = 0.008.T= 0.0s denotes the initiation of microgravity.

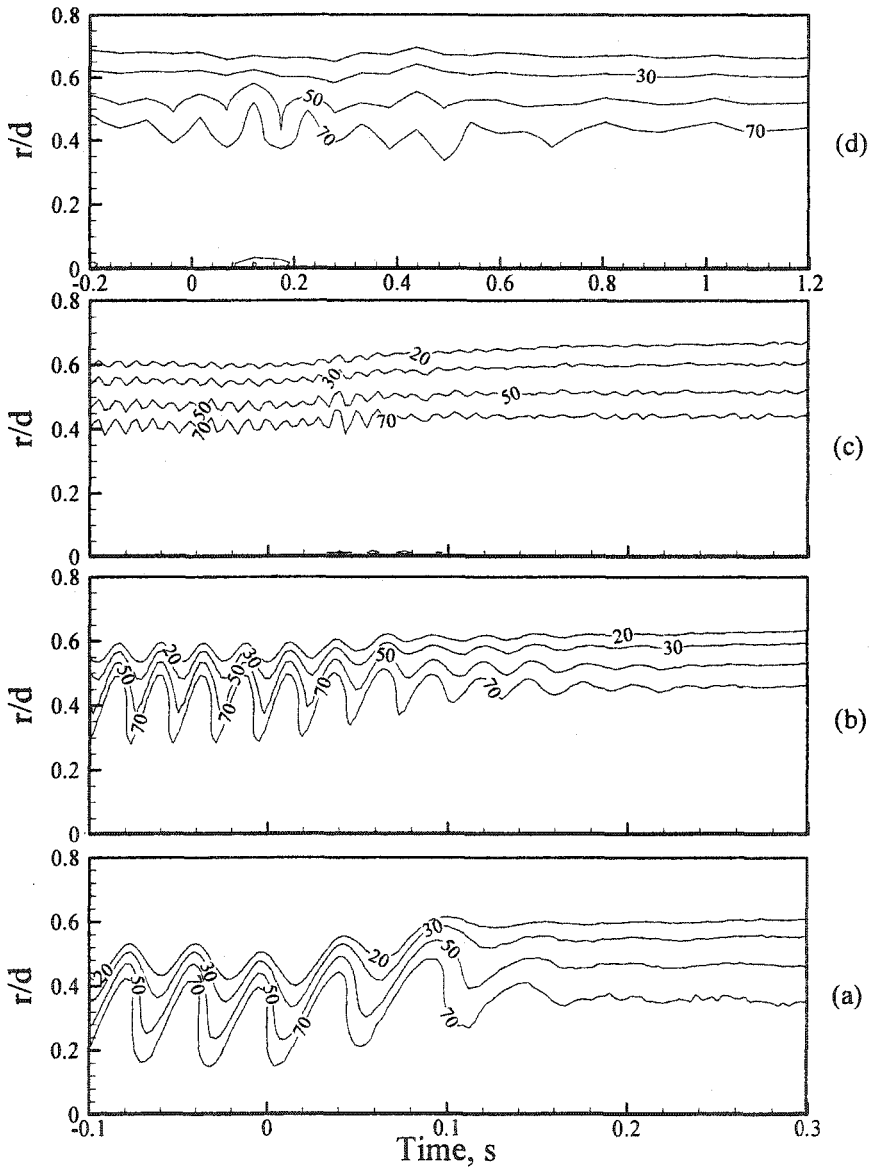


Figure 4.22: Change from Earth gravity to microgravity for varying Ri at z/d = 2.0 for, (a) Re = 200, Ri = 0.72, (b) Re = 800, Ri = 0.18, (c) Re =1200, Ri = 0.03 and (d) Re = 800, Ri = 0.008. T= 0.0s denotes the initiation of microgravity.

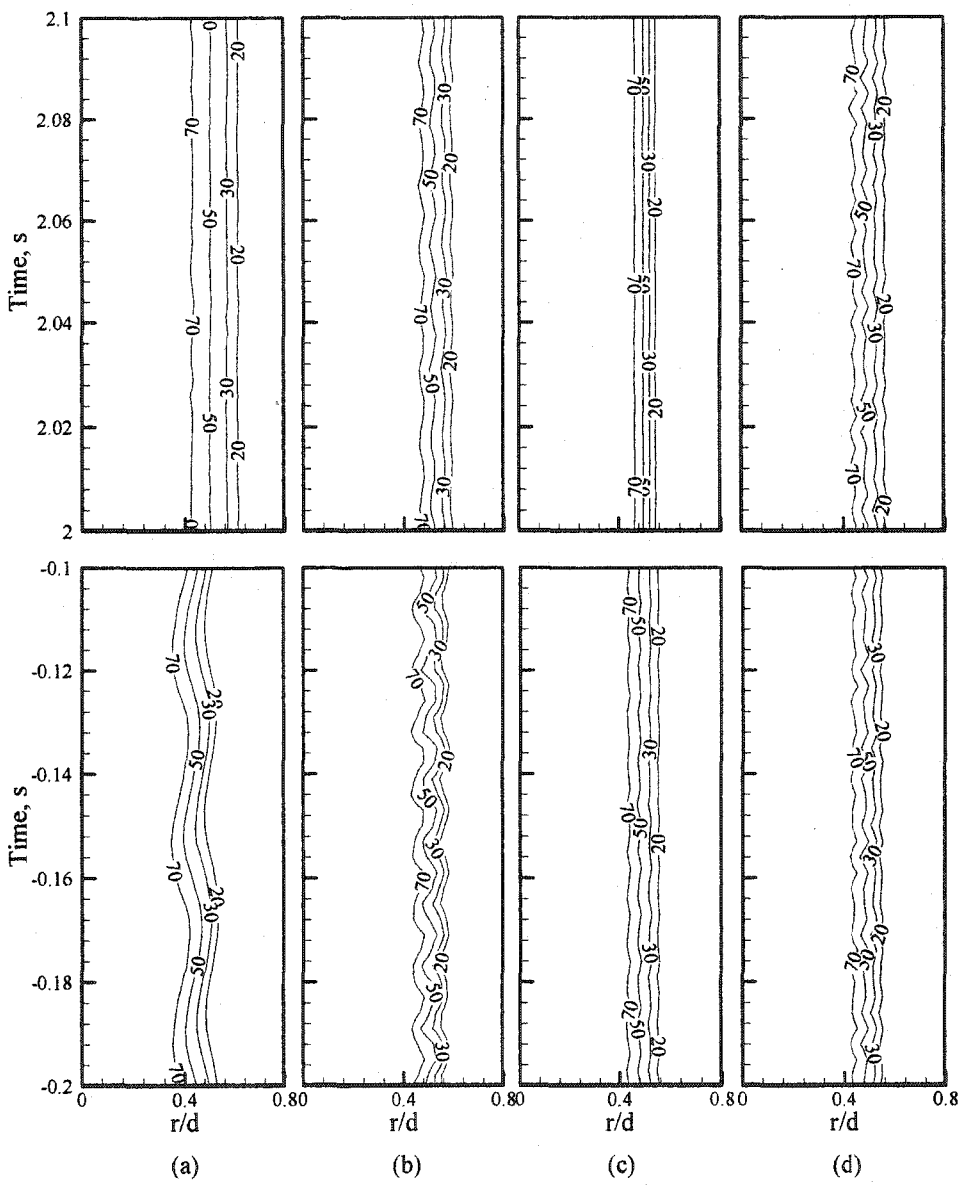


Figure 4.23: Temporal evolution of the helium mole percentage in Earth gravity (bottom) and microgravity (top) at z/d = 0.5 for,
(a) Re = 200, Ri = 0.72, (b) Re = 800, Ri = 0.05, (c) Re =600, Ri = 0.04 and (d) Re = 1200, Ri = 0.008. T= 0.0s denotes the initiation of microgravity.

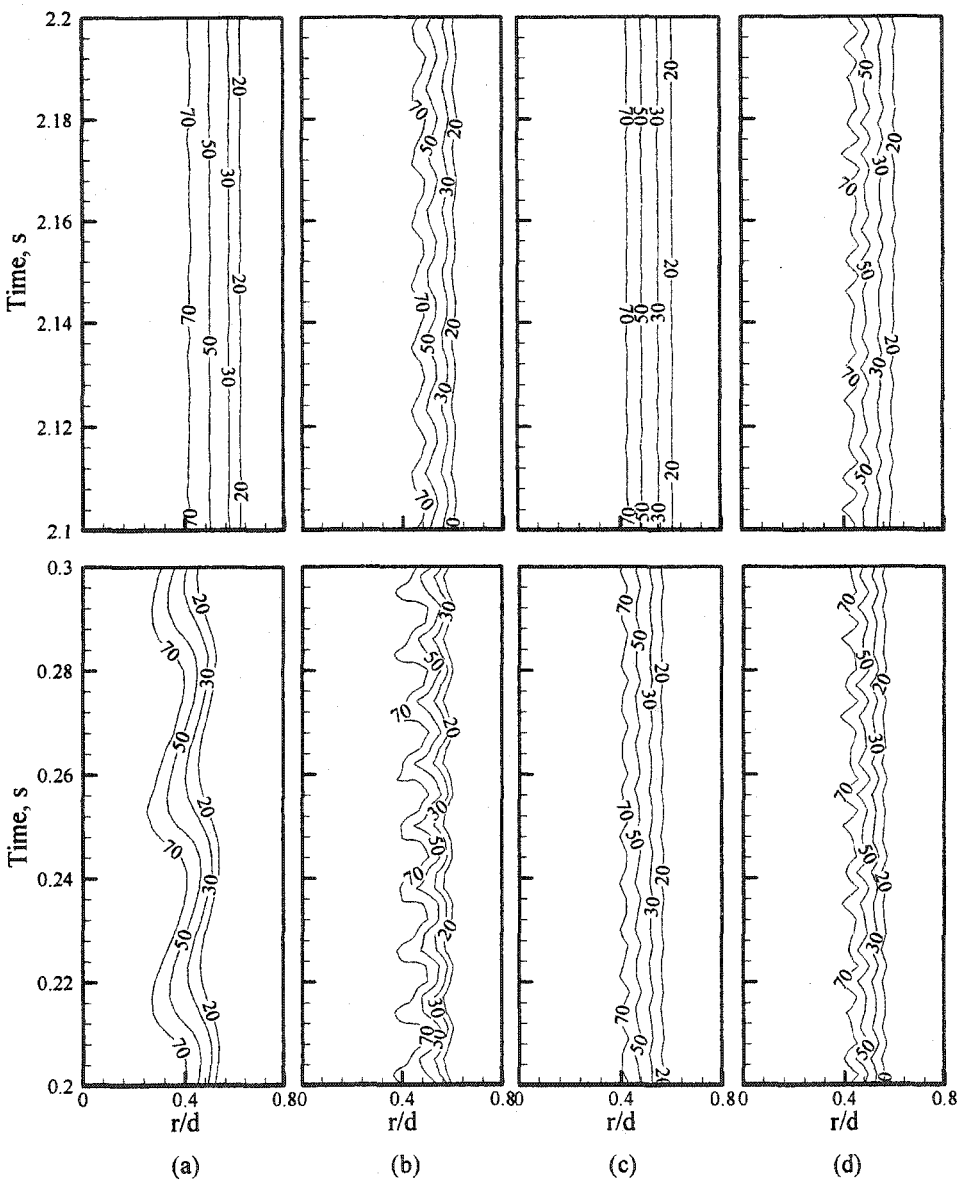


Figure 4.24: Temporal evolution of the helium mole percentage in Earth gravity (bottom) and microgravity (top) at z/d = 1.0 for,
(a) Re = 200, Ri = 0.72, (b) Re = 800, Ri = 0.05, (c) Re =600, Ri = 0.04 and (d) Re = 1200, Ri = 0.008. T= 0.0s denotes the initiation of microgravity.

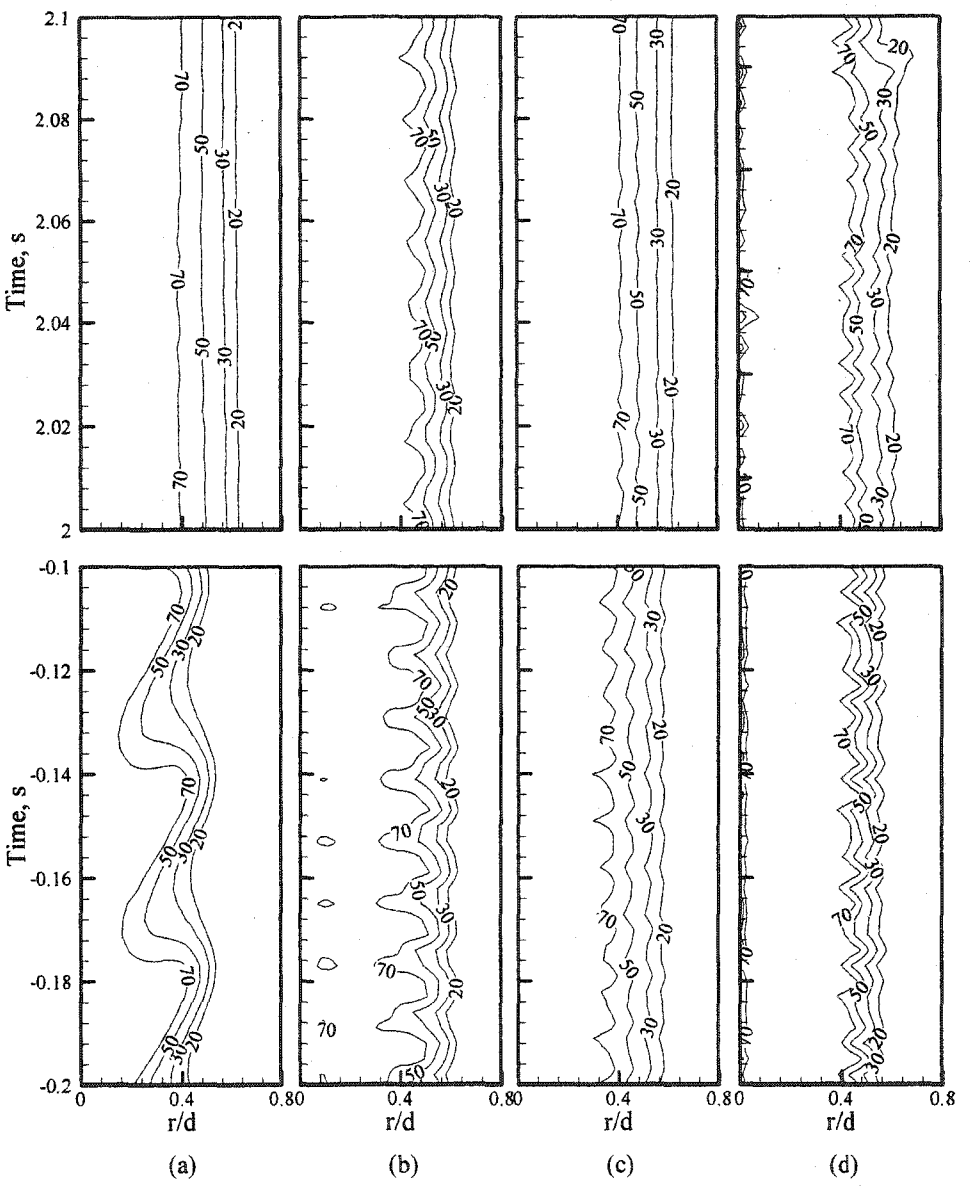


Figure 4.25: Temporal evolution of the helium mole percentage in Earth gravity (bottom) and microgravity (top) at z/d = 2.0 for,
(a) Re = 200, Ri = 0.72, (b) Re = 800, Ri = 0.04, (c) Re =600, Ri = 0.04 and (d) Re = 1200, Ri = 0.008. T= 0.0s denotes the initiation of microgravity.

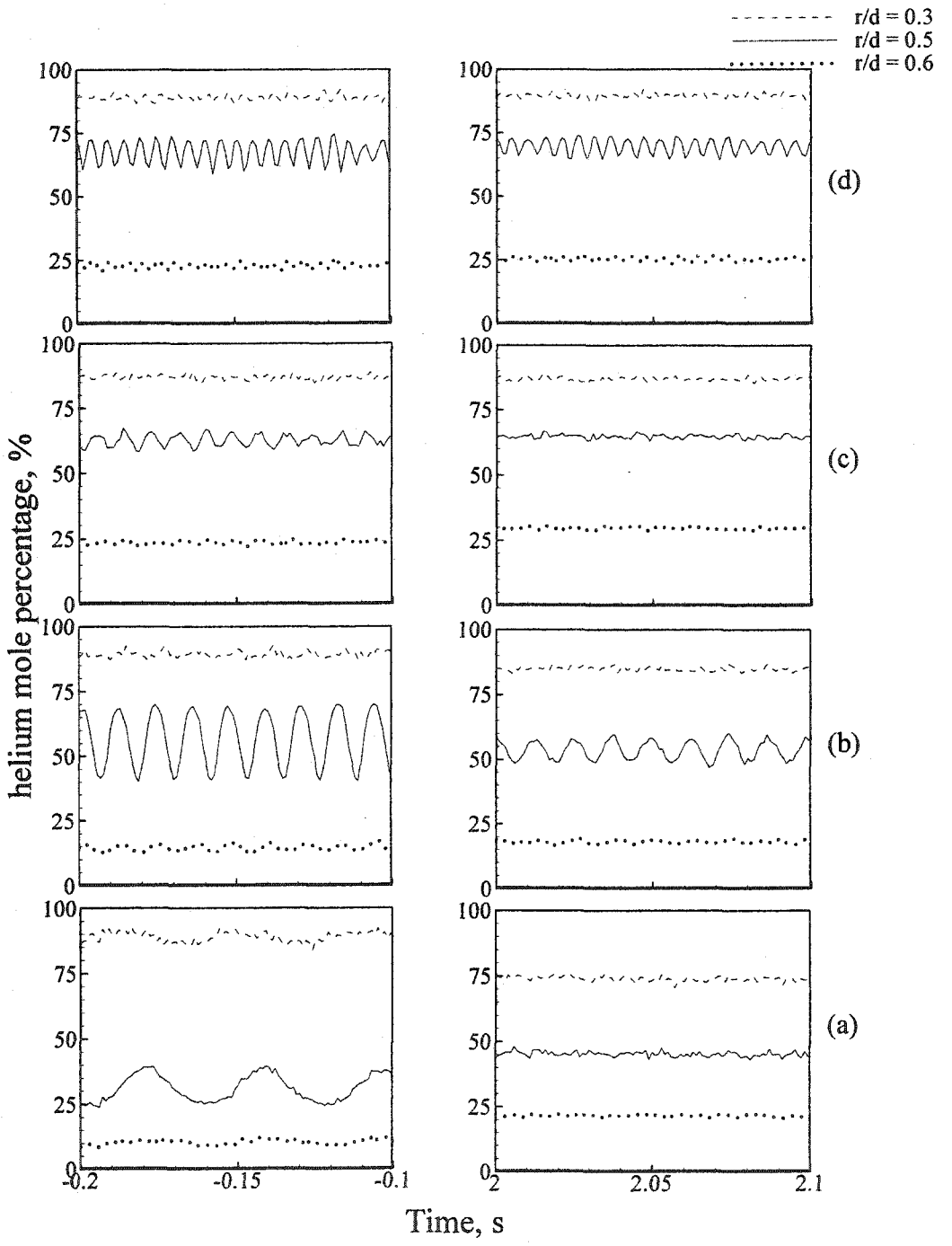


Figure 4.26: Temporal evolution of the helium mole percentage in Earth gravity (left) and microgravity (right) at z/d = 0.5 for different Ri for,
(a) Case 1, Re = 200, Ri = 0.72, d = 19.05mm, (b) Case 2, Re = 800, Ri = 0.045, d = 19.05mm, (c) Case 5, Re = 600, Ri = 0.013, d = 14.5mm and (d) Case 8, Re = 1200, Ri = 0.008, d = 14.5mm. T= 0.0s denotes the initiation of microgravity.

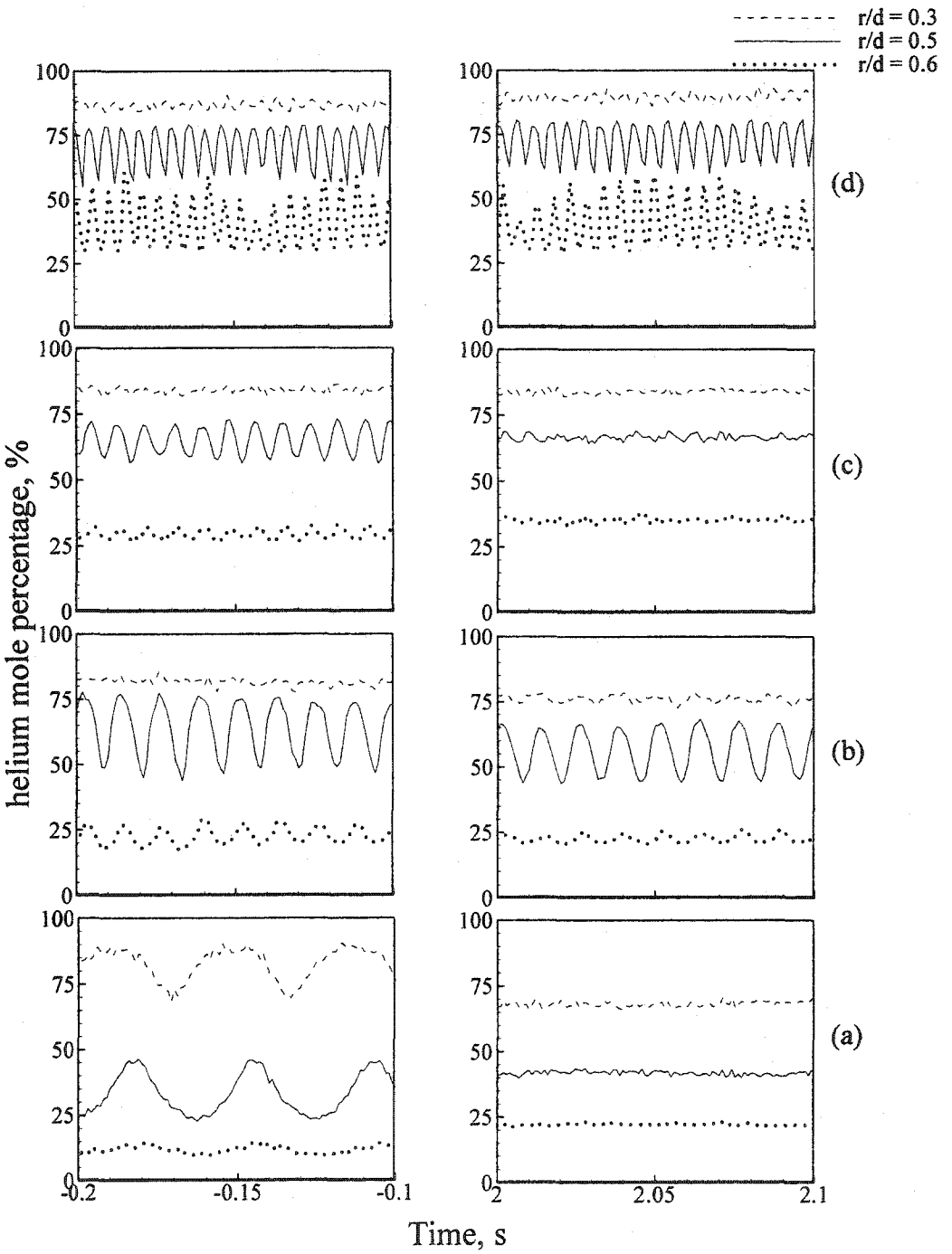


Figure 4.27: Temporal evolution of the helium mole percentage in Earth gravity (left) and microgravity (right) at z/d = 1.0 for different Ri for,
(a) Case 1, Re = 200, Ri = 0.72, d = 19.05mm, (b) Case 2, Re = 800, Ri = 0.045, d = 19.05mm, (c) Case 5, Re = 600, Ri = 0.013, d = 14.5mm and (d) Case 8, Re = 1200, Ri = 0.008, d = 14.5mm. T= 0.0s denotes the initiation of microgravity.

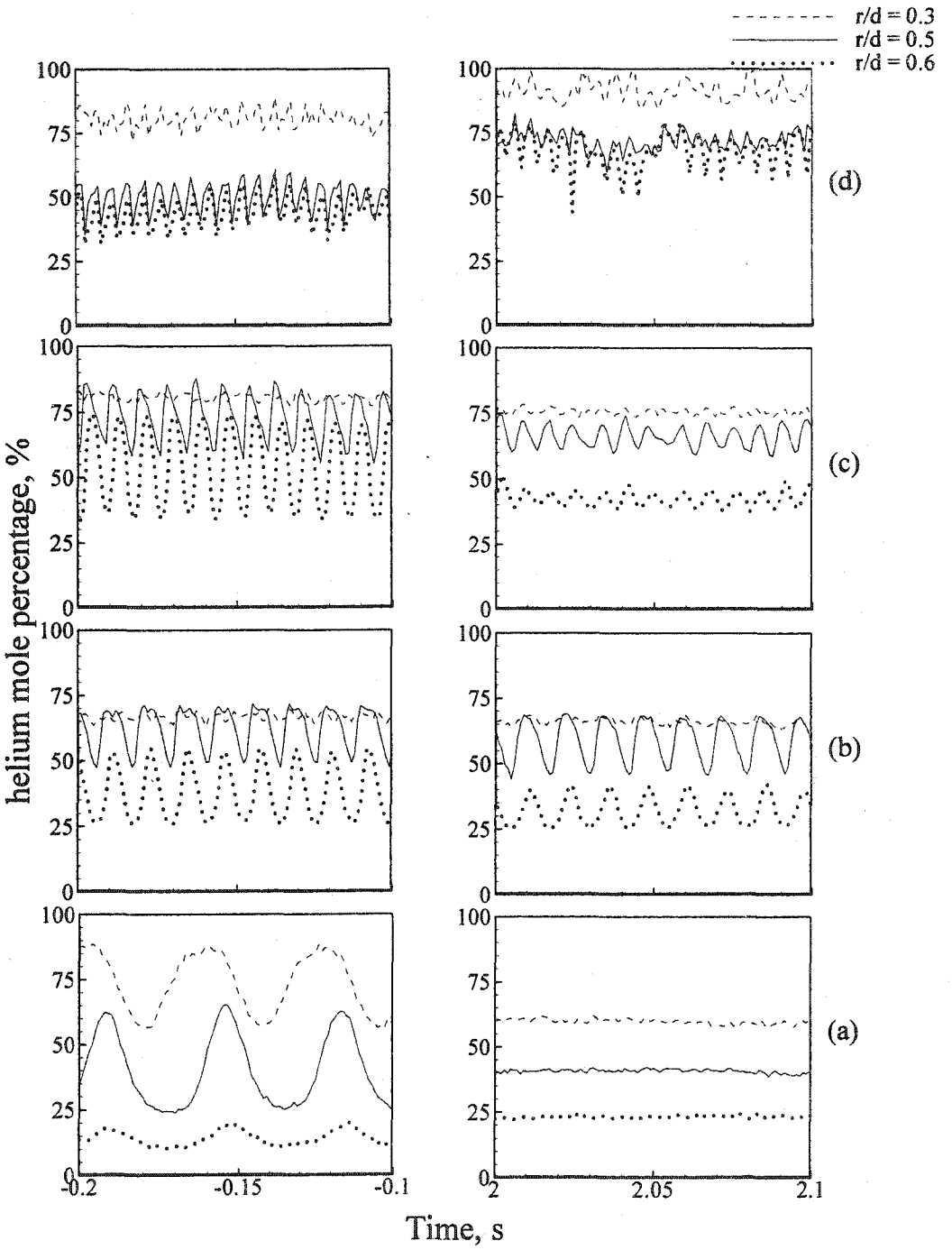


Figure 4.28: Temporal evolution of the helium mole percentage in Earth gravity (left) and microgravity (right) at z/d = 2.0 for different Ri for,
(a) Case 1, Re = 200, Ri = 0.72, d = 19.05mm, (b) Case 2, Re = 800, Ri = 0.045, d = 19.05mm, (c) Case 5, Re = 600, Ri = 0.013, d = 14.5mm and (d) Case 8, Re = 1200, Ri = 0.008, d = 14.5mm. T= 0.0s denotes the initiation of microgravity.

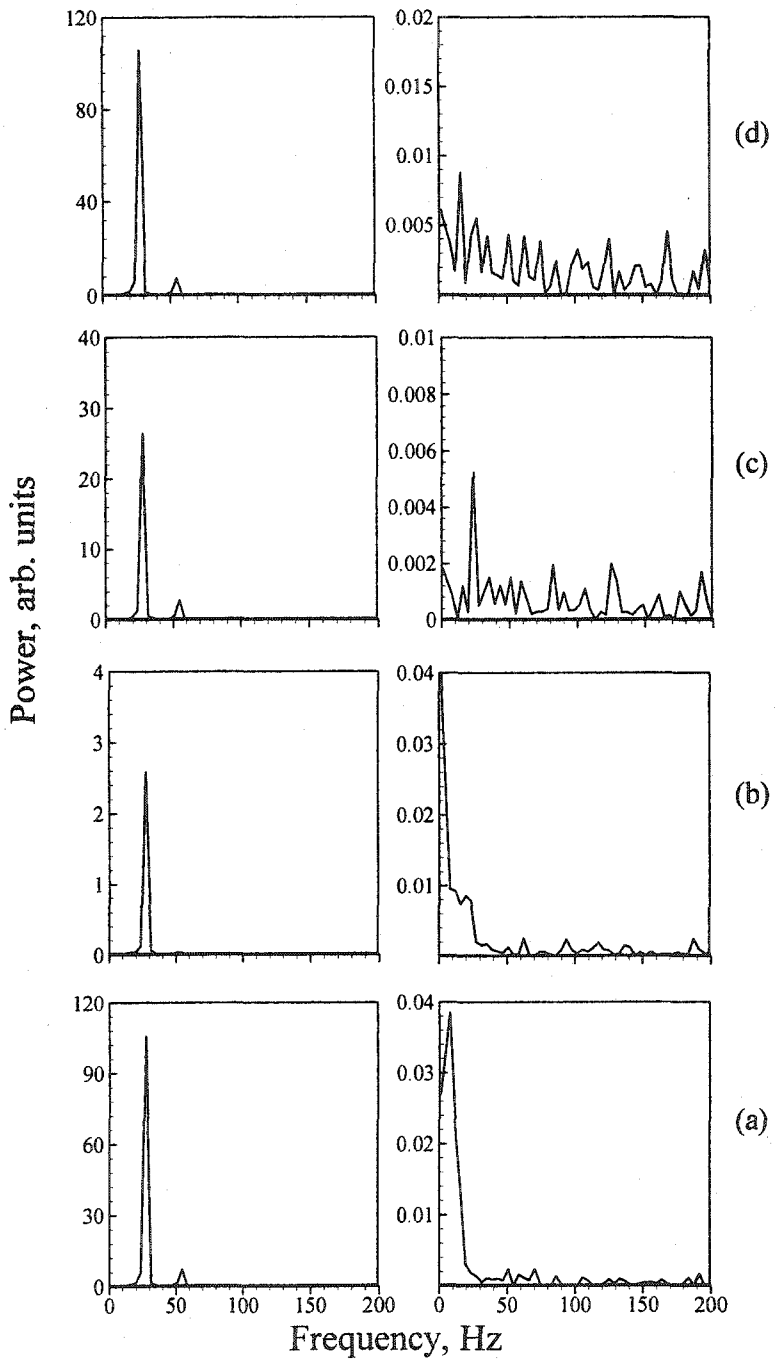


Figure 4.29: Power spectra for various locations throughout the flow field in Earth gravity (left) and microgravity (right) for Re = 200, Ri = 0.72 at (a) z/d = 0.02, r/d = 0.1 (b) z/d = 1.0, r/d = 0.3, (c) z/d = 1.5, r/d = 0.4 and (d) z/d = 2.0, r/d = 0.5.

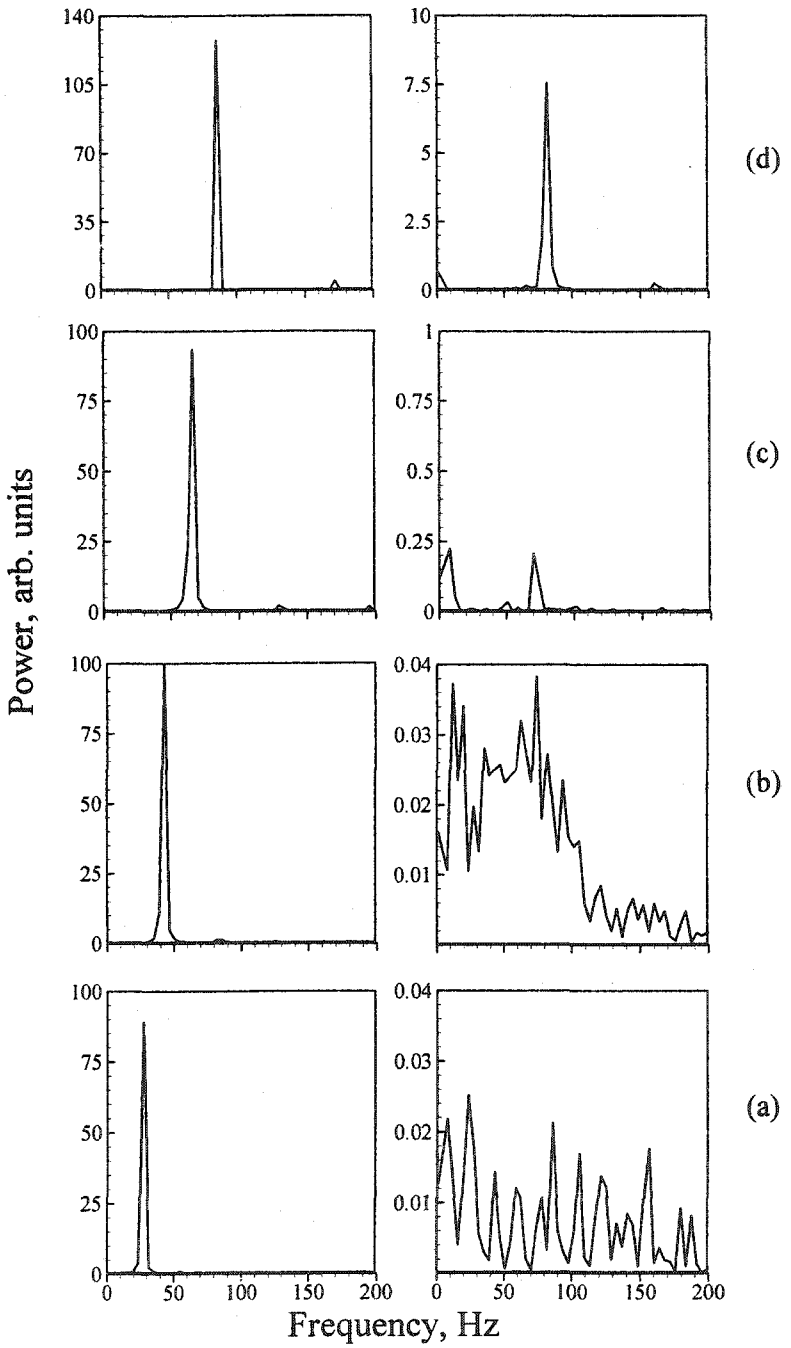


Figure 4.30: Evolution of power spectra with Richardson number in Earth gravity (left) and microgravity (right) for, (a) Re = 200, Ri = 0.72, r/d = 0.47, (b) Re = 400, Ri = 0.18, r/d = 0.53, (c) Re = 600, Ri = 0.08, r/d = 0.57 and (d) Re = 800, Ri = 0.05, r/d = 0.59.

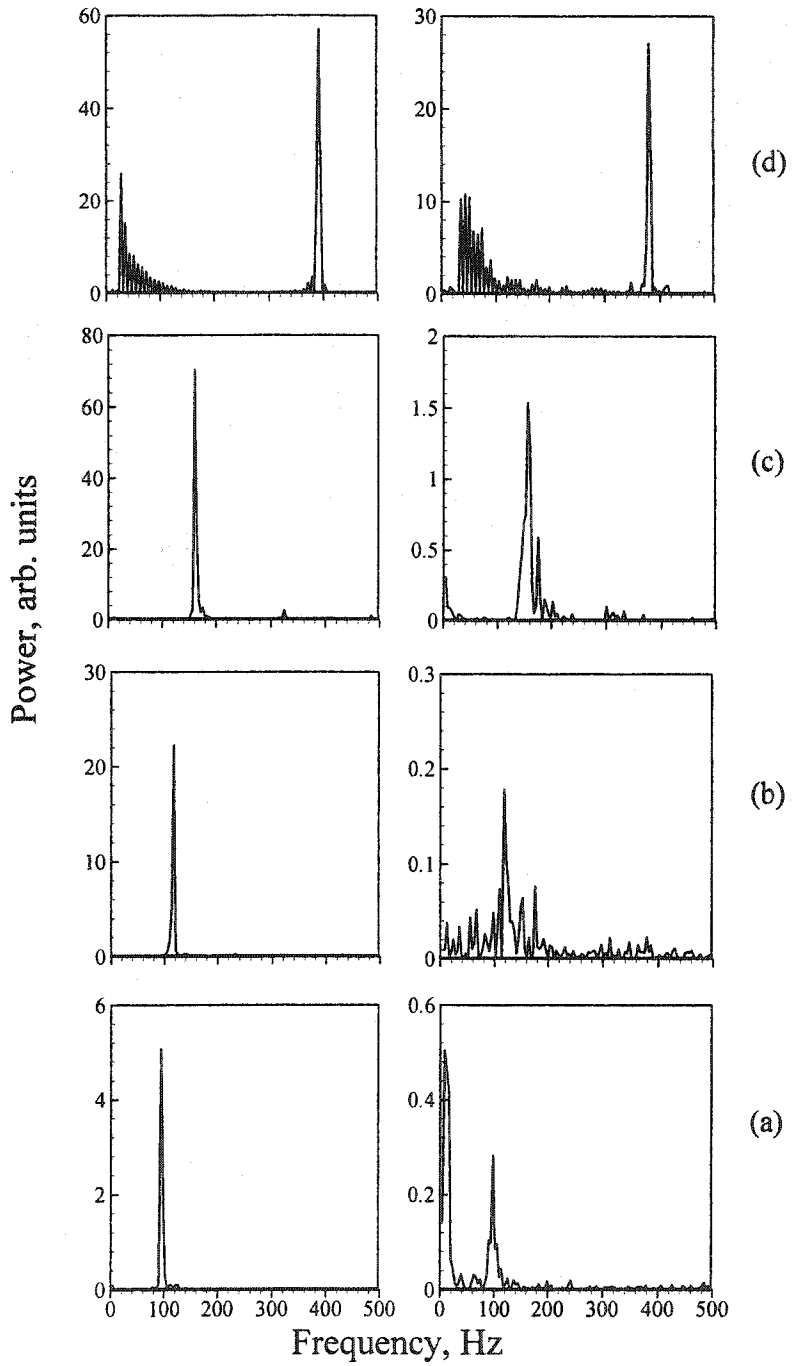


Figure 4.31: Evolution of power spectra with Richardson number in Earth gravity (left) and microgravity (right) at z/d = 0.5 for, (a) Re = 600, Ri = 0.04, r/d = 0.64, (b) Re =800, Ri = 0.02, r/d = 0.54, (c) Re = 1000, Ri = 0.02, r/d = 0.6 and (d) Re = 1200, Ri = 0.008, r/d = 0.5.

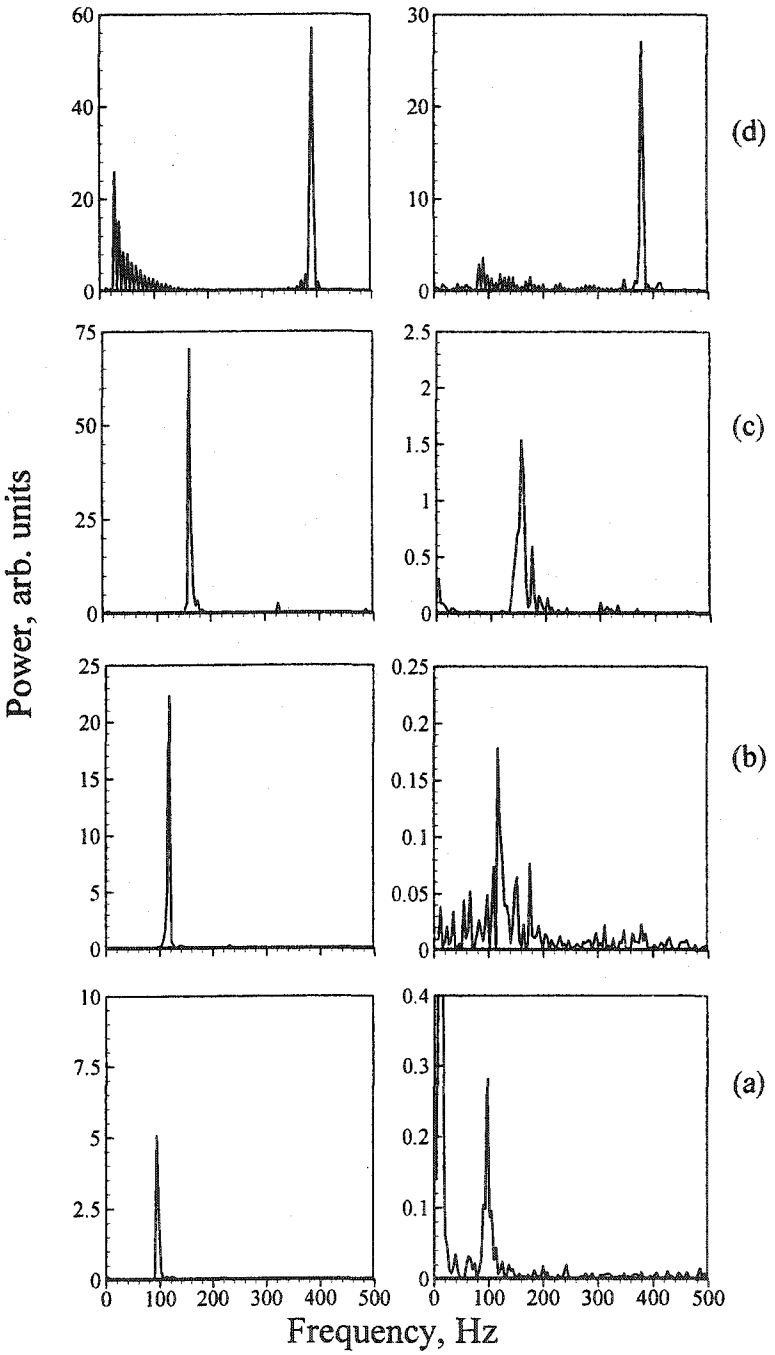


Figure 4.32: Evolution of power spectra with Richardson number in Earth gravity (left) and microgravity (right) at z/d = 1.5 for, (a) Re = 600, Ri = 0.04, r/d = 0.64, (b) Re =800, Ri = 0.02, r/d = 0.54, (c) Re = 1000, Ri = 0.02, r/d = 0.6 and (d) Re = 1200, Ri = 0.008, r/d = 0.5.

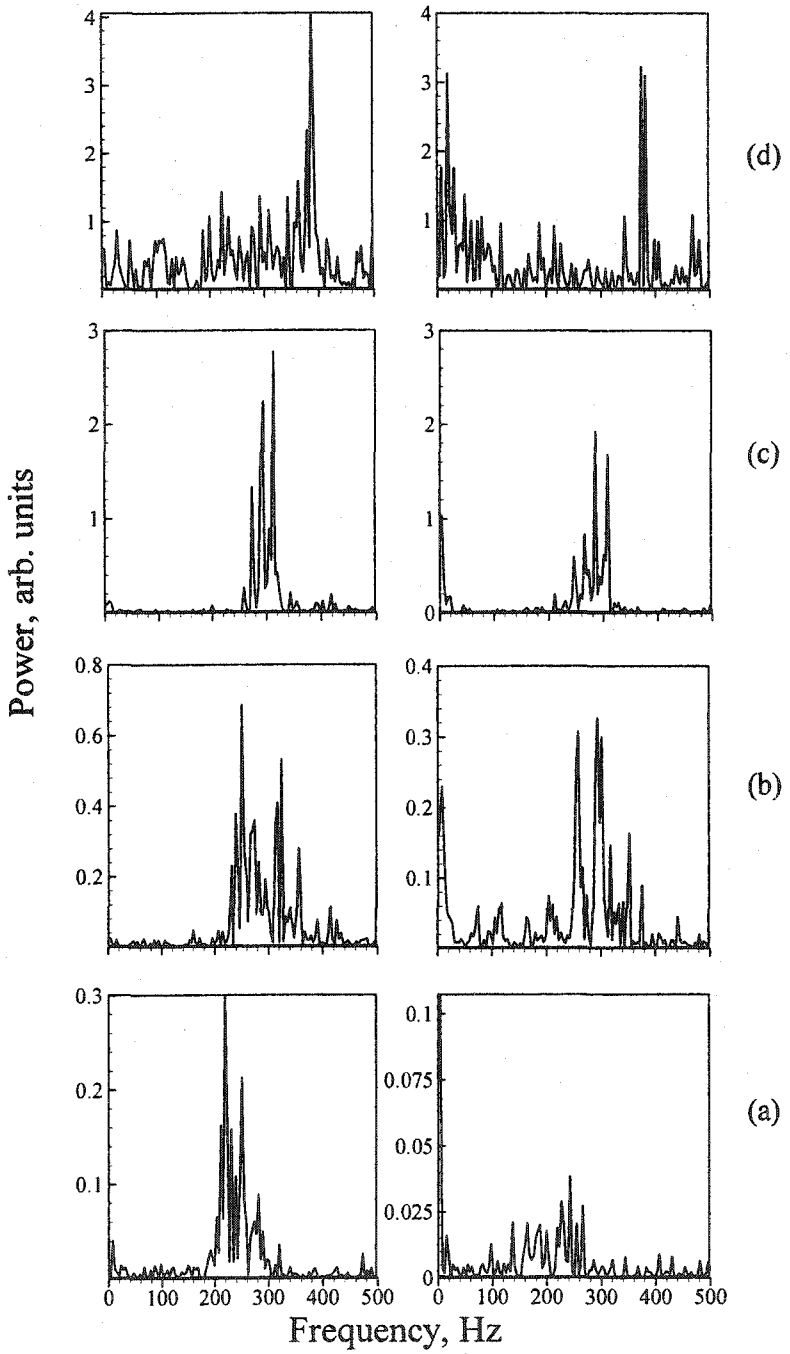


Figure 4.33: Evolution of power spectra with Richardson number in Earth gravity (left) and microgravity (right) for, (a) Re = 800, Ri = 0.008, r/d = 0.53, (b) Re =1000, Ri = 0.005, r/d = 0.49, (c) Re = 1200, Ri = 0.003, r/d = 0.53 and (d) Re = 1500, Ri = 0.002, r/d = 0.56.

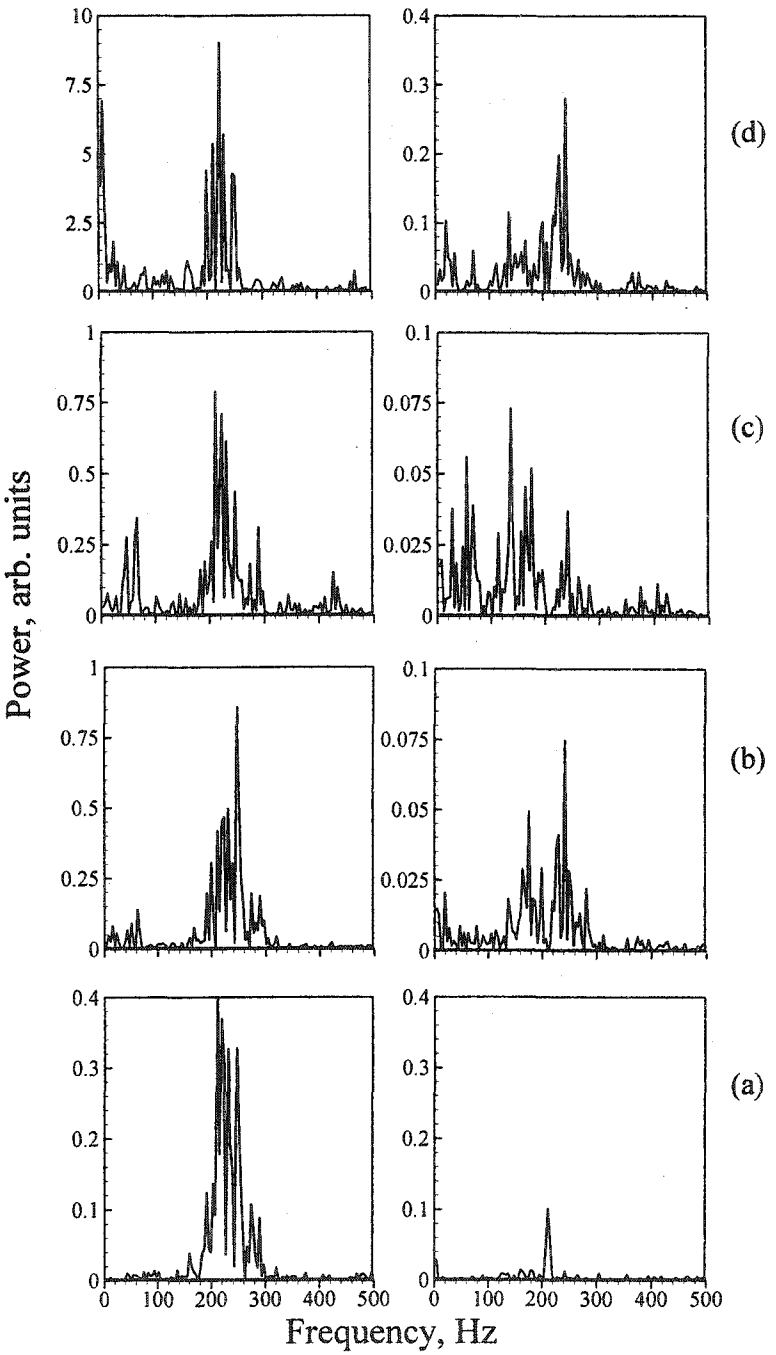


Figure 4.34: Spatial evolution of power spectra in the jet shear layer (r/d = 0.52) in Earth gravity (left) and microgravity (right), Re = 800, Ri = 0.008 at (a) z/d = 0.5, (b) z/d = 1.0, (c) z/d = 1.5 and (d) z/d = 1.7.

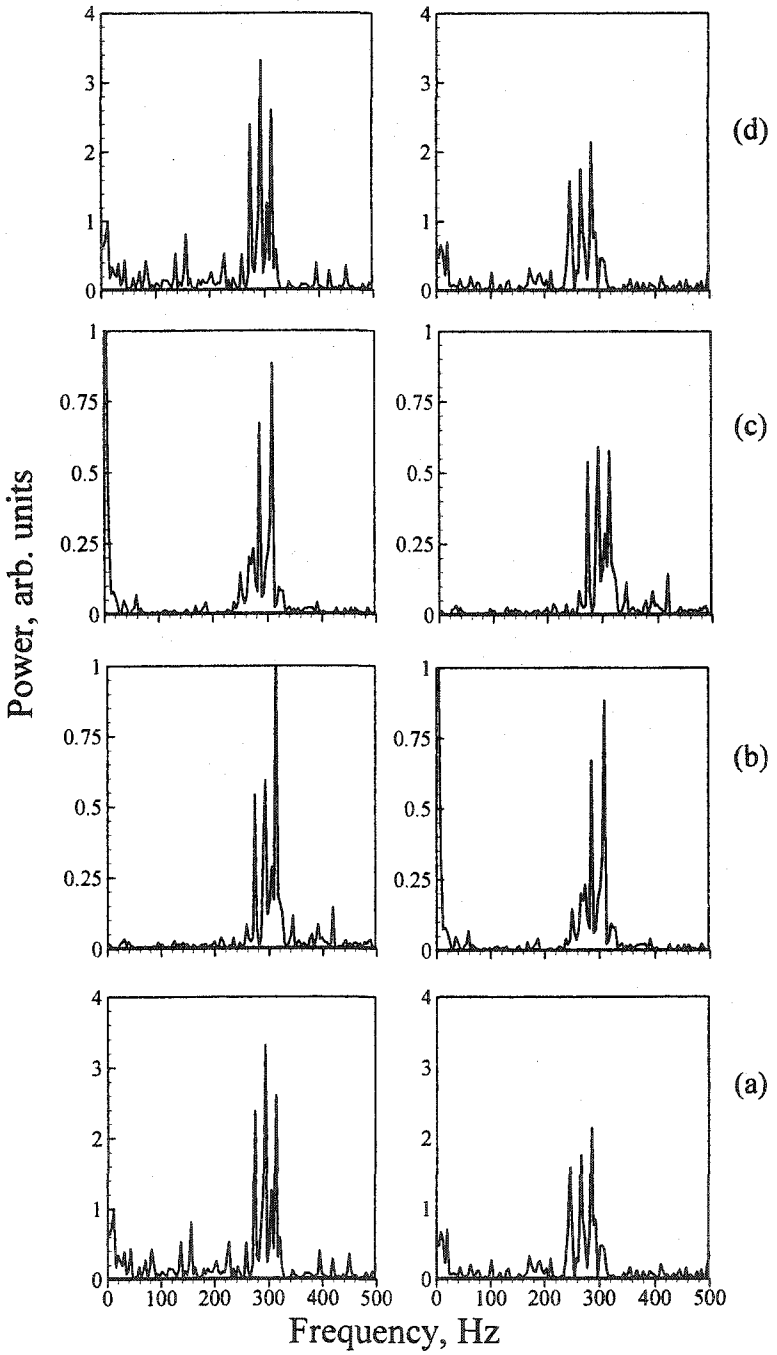


Figure 4.35: Spatial evolution of power spectra in the jet shear layer (r/d = 0.52) in Earth gravity (left) and microgravity (right), Re = 1200, Ri = 0.003 at (a) z/d = 0.5, (b) z/d = 1.0, (c) z/d = 1.5 and (d) z/d = 1.7.

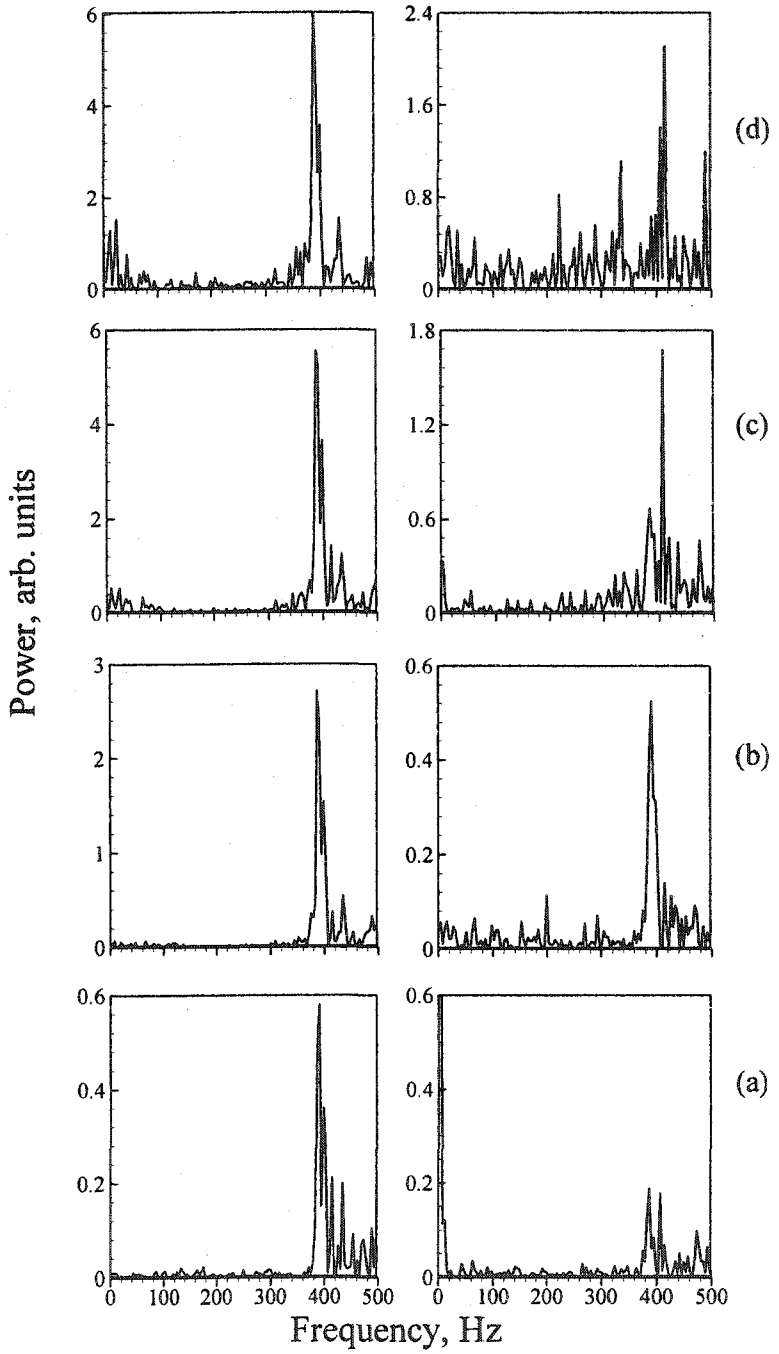


Figure 4.36: Spatial evolution of power spectra in the jet shear layer (r/d = 0.52) in Earth gravity (left) and microgravity (right), Re = 1500, Ri = 0.002 at (a) z/d = 0.5, (b) z/d = 1.0, (c) z/d = 1.5 and (d) z/d = 1.7.

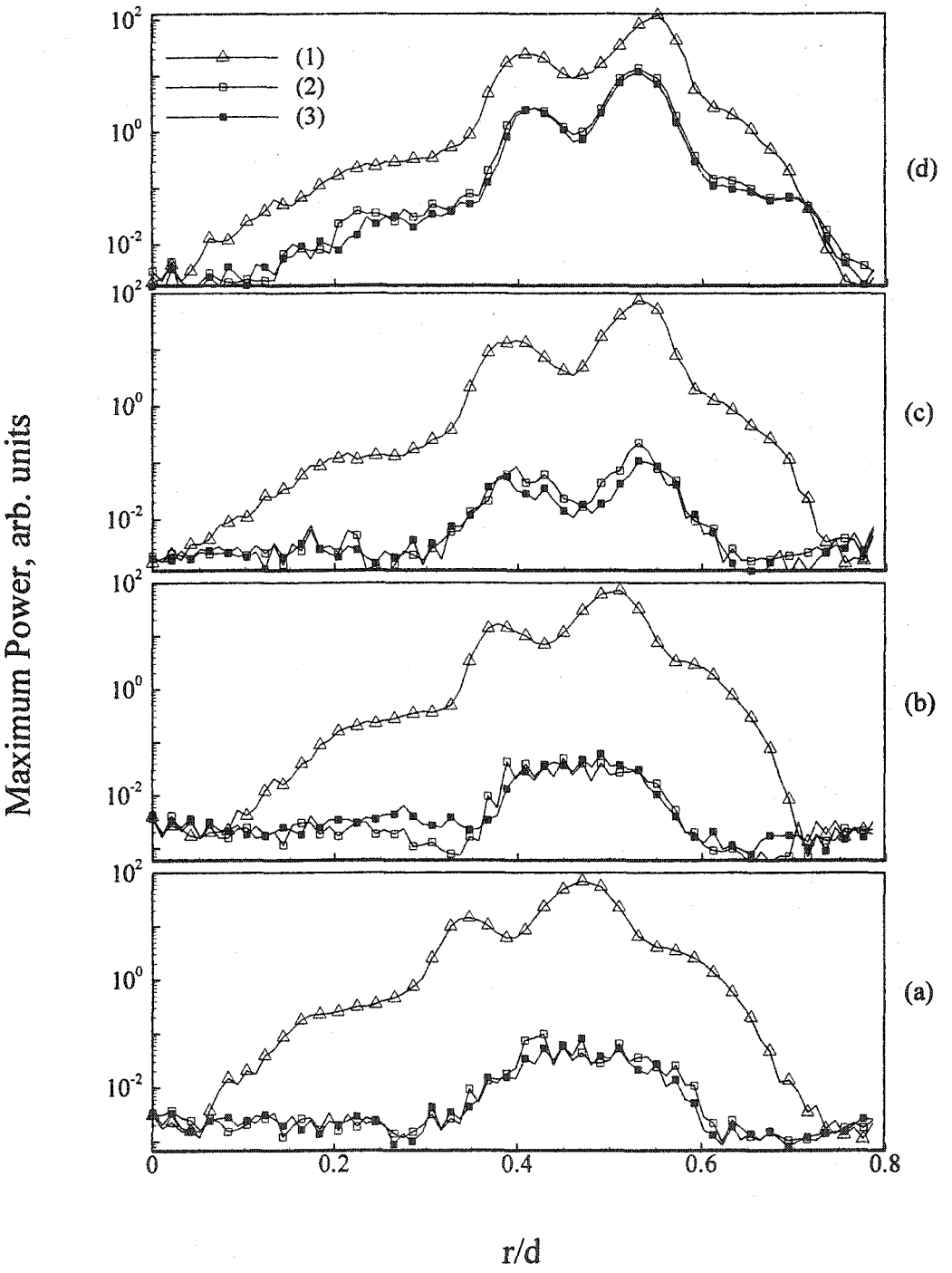


Figure 4.37: Peak power plots (Logscales) for varying Richardson number in Earth gravity and microgravity, d = 19.05mm at (1) Earth gravity (T=-0.1s), (2) Microgravity (T=1.1-1.35s), (3) Microgravity (T=1.9-2.15s) for, (a) Re = 200, Ri = 0.72, (b) Re =400, Ri = 0.18, (c) Re = 600, Ri = 0.08 and (d) Re = 800, Ri = 0.05.

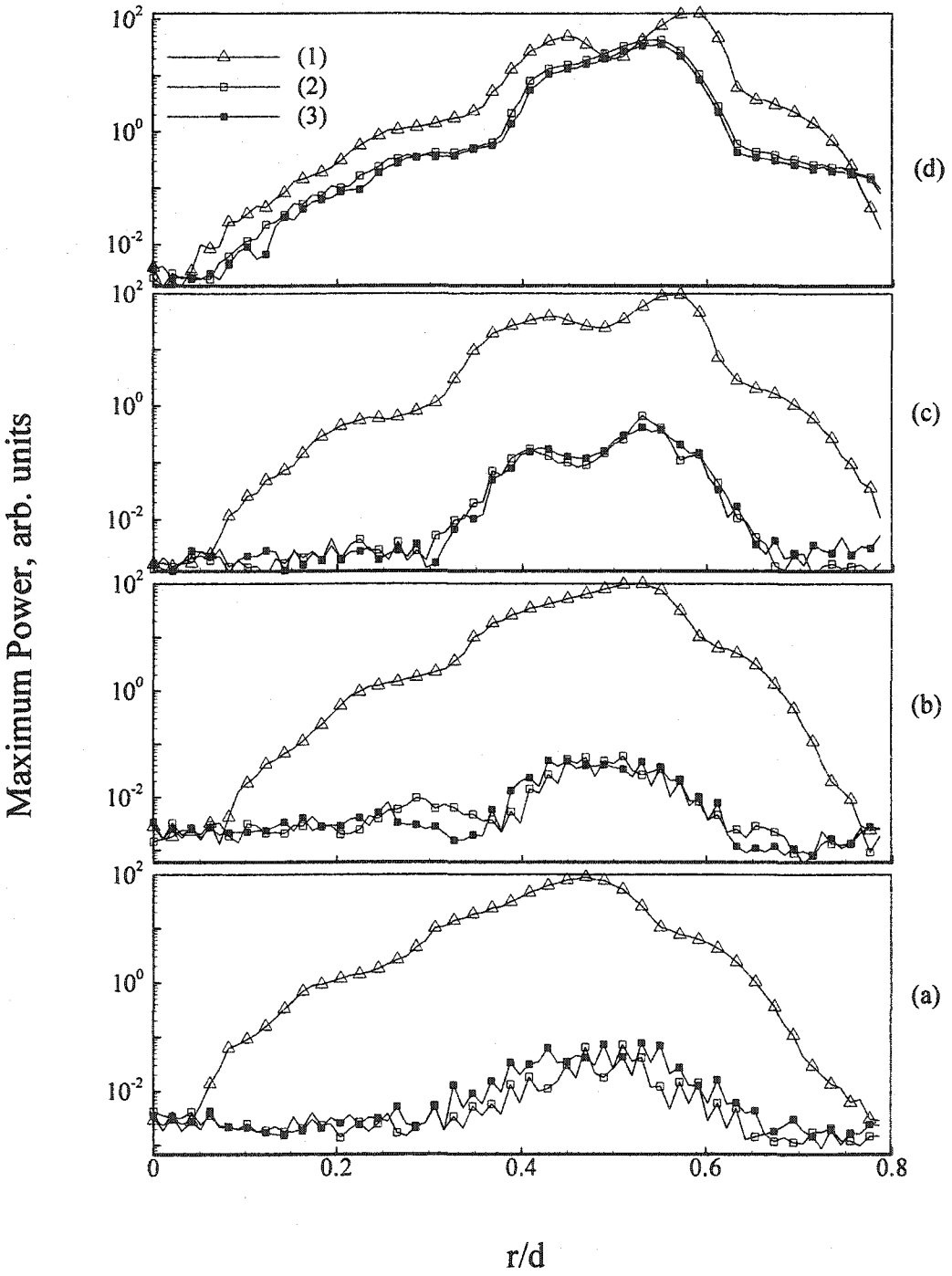


Figure 4.38: Peak power plots (Logscales) for varying Richardson number in Earth gravity and microgravity, d = 19.05mm at (1) Earth gravity (T=-0.1s), (2) Microgravity (T=1.1-1.35s), (3) Microgravity (T=1.9-2.15s) for, (a) Re = 200, Ri = 0.72, (b) Re =400, Ri = 0.18, (c) Re = 600, Ri = 0.08 and (d) Re = 800, Ri = 0.05.

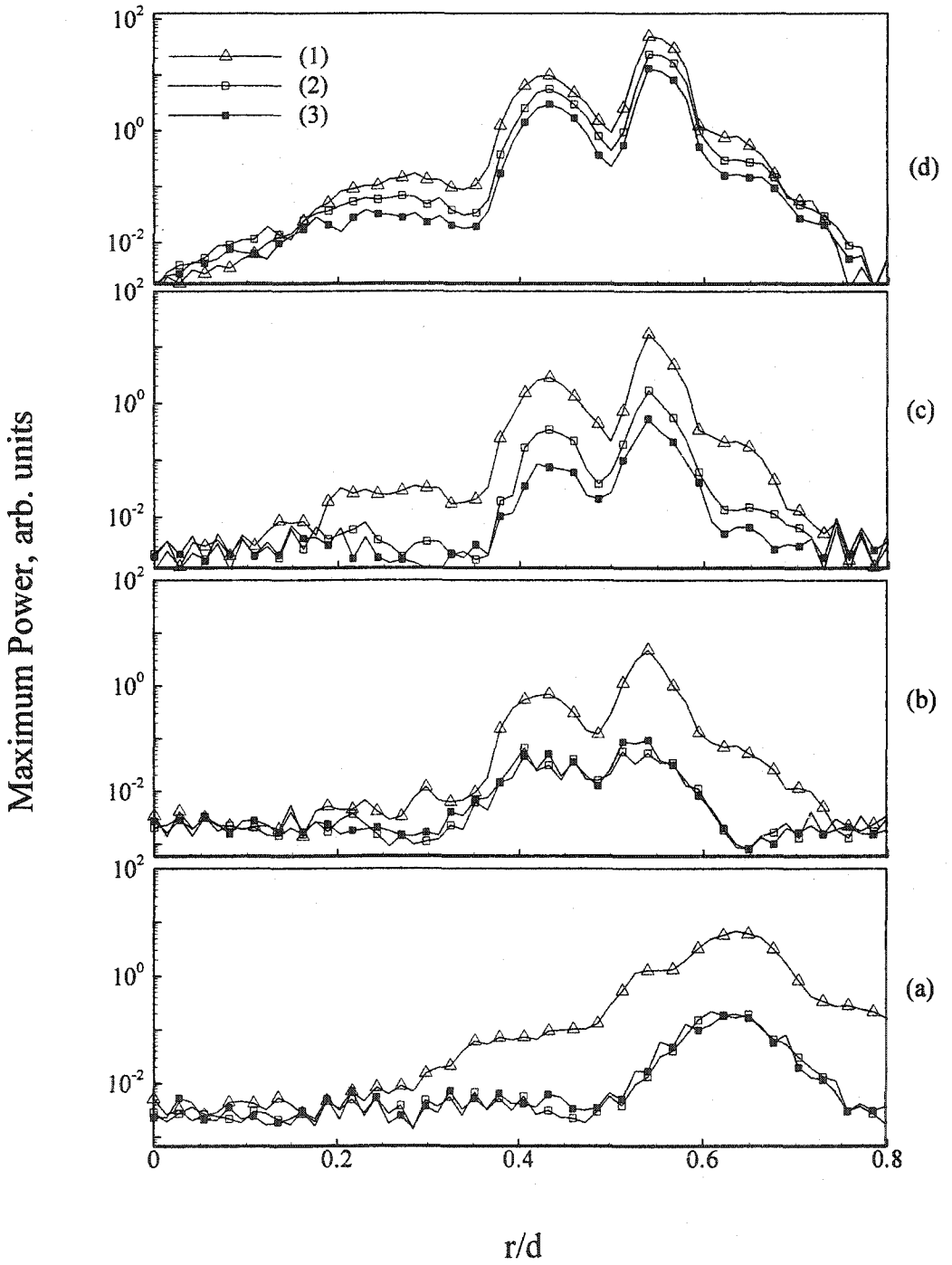


Figure 4.39: Peak power (Logscales) plots for varying Richardson number in Earth gravity and microgravity, at (1) Earth gravity (T=-0.1s), (2) Microgravity (T=1.1-1.35s), (3) Microgravity (T=1.9-2.15s) for, (a) Re = 600, Ri = 0.04, (b) Re =800, Ri = 0.02, (c) Re = 1000, Ri = 0.02 and (d) Re = 1200, Ri = 0.008.

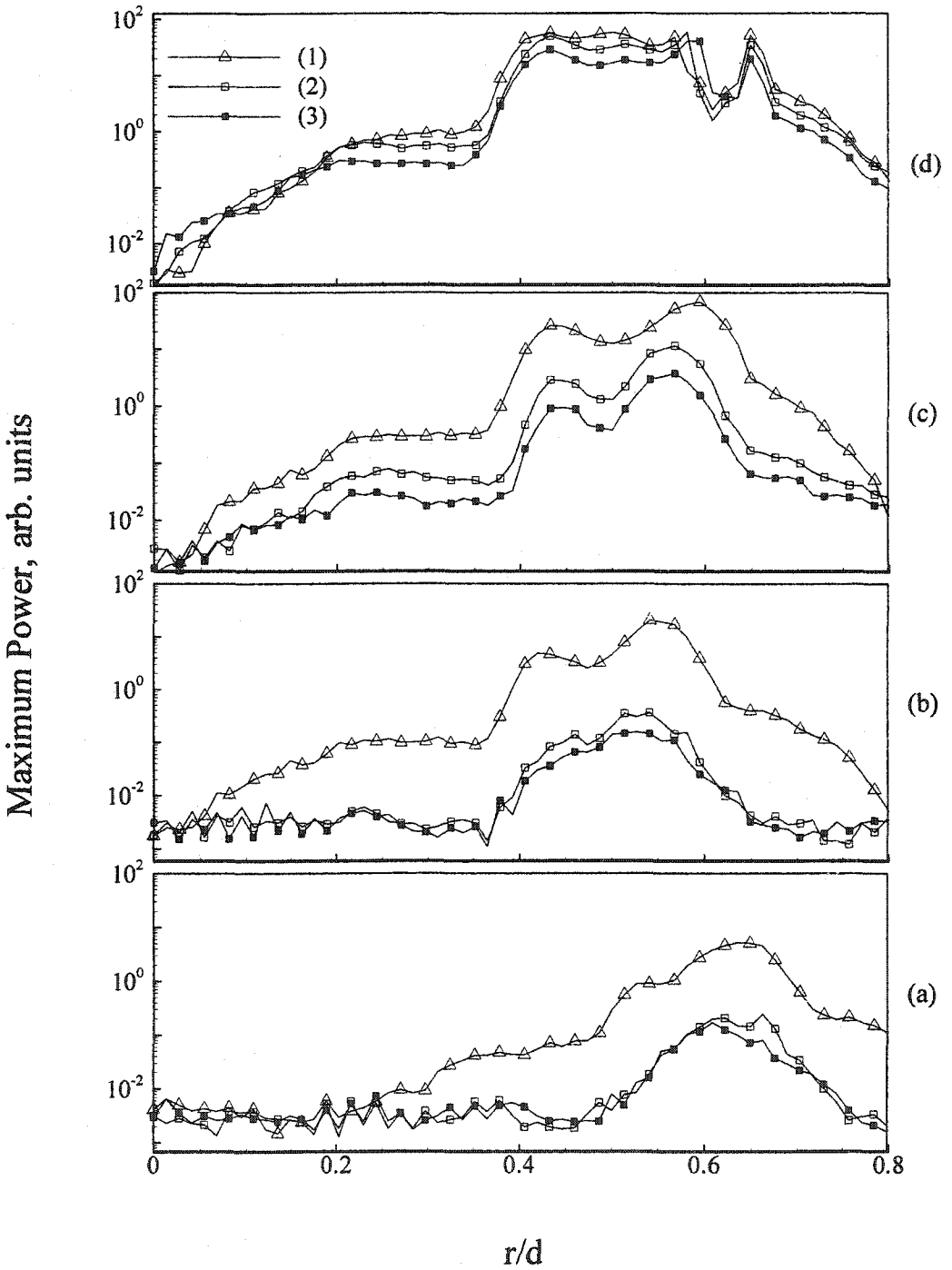


Figure 4.40: Peak power (Logscales) plots for varying Richardson number in Earth gravity and microgravity, at (1) Earth gravity (T=-0.1s), (2) Microgravity (T=1.1-1.35s), (3) Microgravity (T=1.9-2.15s) for, (a) Re = 600, Ri = 0.04, (b) Re =800, Ri = 0.02, (c) Re = 1000, Ri = 0.02 and (d) Re = 1200, Ri = 0.008.

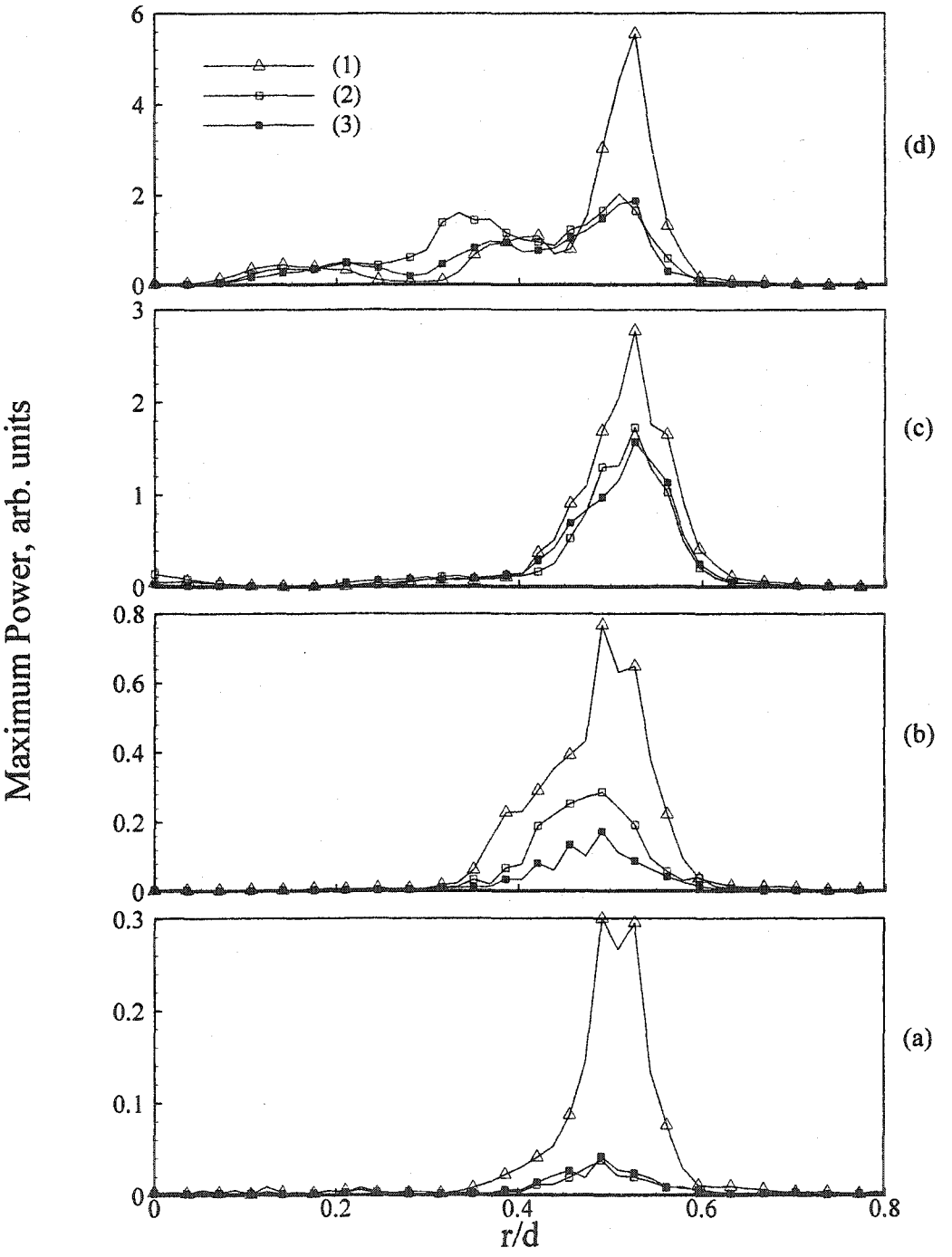


Figure 4.41: Peak power plots for varying Richardson number in Earth gravity and microgravity, at (1) Earth gravity (T=-0.1s), (2) Microgravity (T=1.1-1.35s), (3) Microgravity (T=1.9-2.15s) for, (a) Re = 800, Ri = 0.008, (b) Re = 1000, Ri = 0.005, (c) Re =1200, Ri = 0.003 and (d) Re = 1500, Ri = 0.002.

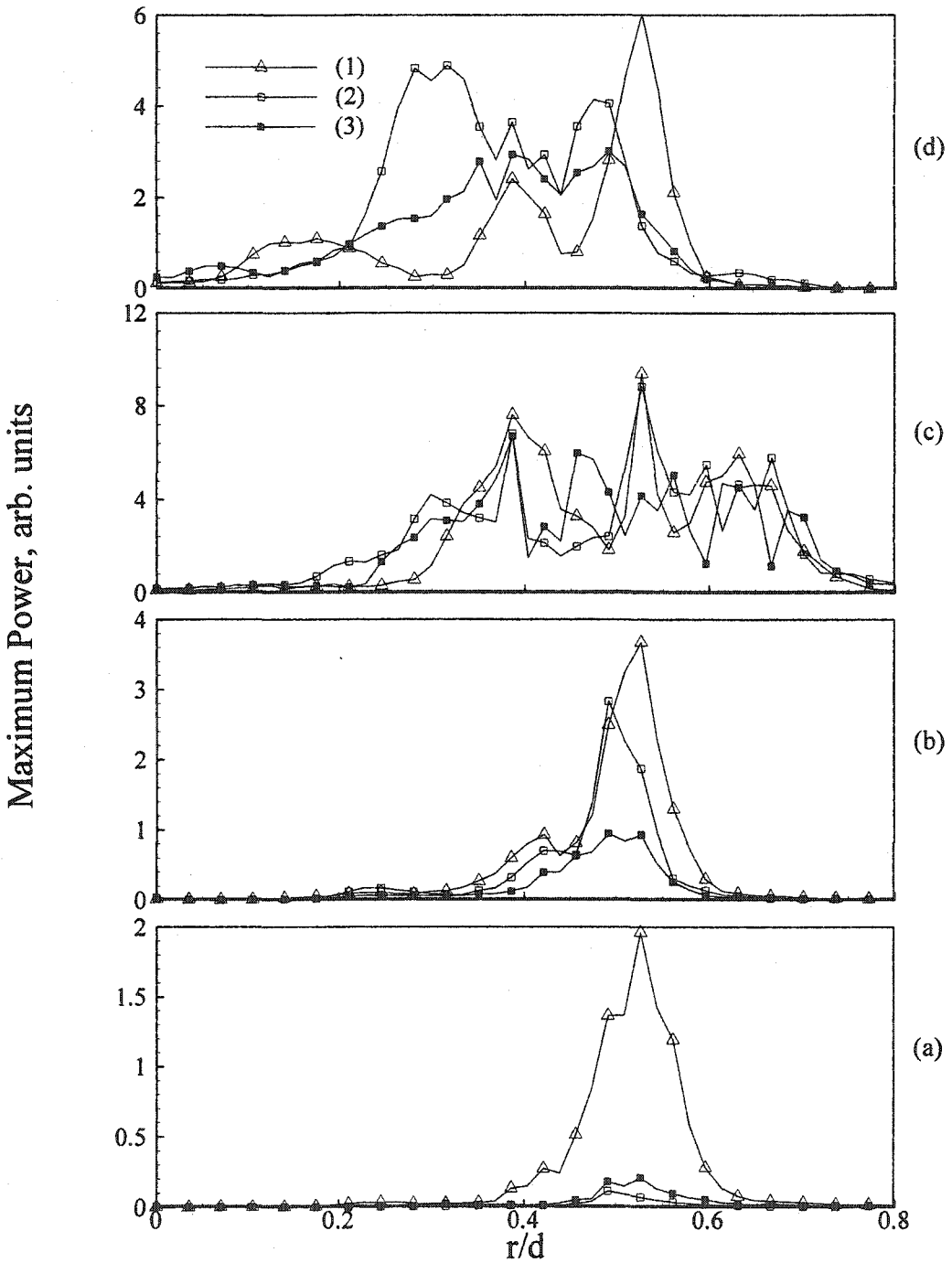


Figure 4.42: Peak power plots for varying Richardson number in Earth gravity and microgravity, at (1) Earth gravity (T=-0.1s), (2) Microgravity (T=1.1-1.35s), (3) Microgravity (T=1.9-2.15s) for, (a) Re = 800, Ri = 0.008, (b) Re = 1000, Ri = 0.005, (c) Re =1200, Ri = 0.003 and (d) Re = 1500, Ri = 0.002.

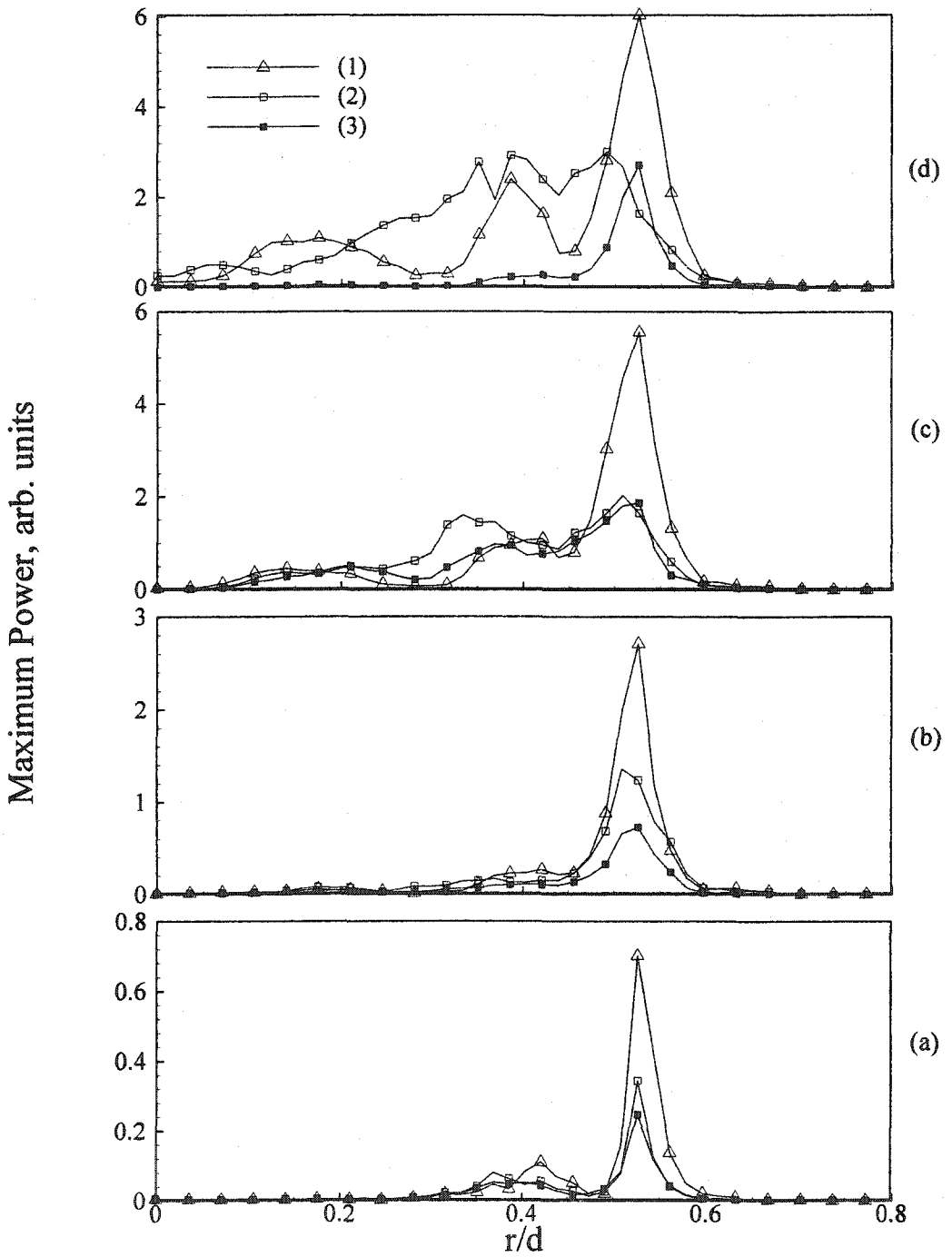


Figure 4.43: Spatial evolution of peak power in Earth gravity and microgravity, Re = 1500, Ri = 0.002 at (a) z/d = 0.5, (b) z/d = 1.0, (c) z/d = 1.5, (d) z/d = 1.7 for (1) Earth gravity (T=-0.1s), (2) Microgravity (T=1.1-1.35s) and (3) Microgravity (T=1.9-2.15s).

4.3 Buoyancy Effects in the Transitional Region of Low-Density Jets

In addition to the variation in near-field flow structure, visible changes were observed in the jet flow transition to turbulence in microgravity. Experimental results of buoyancy effects in the transitional flow regime are presented for two test cases at a fixed jet Reynolds number of 800 in Earth gravity and microgravity conditions. Injector tubes with d = 14.5mm (Case 9) and 10.5mm (Case 6) were used to obtain jet Richardson numbers of 0.02 and 0.008, respectively, in Earth gravity.

4.3.1Flow Visualization

Figure 4.44 shows rainbow schlieren images for the two test cases in Earth gravity and microgravity. The microgravity images were obtained at the end of the drop. The injector wall and exit are visible as a black region in the upstream portion of images. All of the images exhibit good symmetry about the centerline in the laminar region of the jet. For Case 6, the flow transition in Earth gravity, indicated by the appearance of smaller scale structures at the jet center, is evident in Figure 4.44.1(a), approximately at z/d = 3.8. According to Figure 4.44.1(b), the transition is not visible in the field-of-view in microgravity. The jet remains laminar in the absence of gravitational forcing, providing direct evidence of buoyancy effects in an inertial jet. Figures 4.44.2(a) and (b) for Case 9 show that transition occurs approximately at z/d = 4.8 in Earth gravity and at z/d = 5.5 in microgravity. Again, the lack of buoyancy has extended the laminar coherent region in microgravity. Comparing Earth gravity images in Figure 4.44.1, an increase in transition length at the lower jet Richardson number is observed. Results clearly show that buoyancy is important in low-density gas jets at low Richardson numbers.

4.3.2 Space-Time Images

The transient flow behavior is visualized from space-time images in Figure 4.45, developed by concatenating 0.1 second of schlieren data at specified axial planes from a sequence of 100 images. Images are shown for Case 6 at z/d = 4.4 and Case 9 at z/d = 4.4 to represent the transitional/turbulent regions in Earth gravity. For case 6, the periodicity of the flow and breakdown of the potential core in Earth gravity is evident in Figure 4.45.1(a). Note that the smaller scale structures have reached the jet center. In microgravity, Figure 4.45.1(b), the jet center is uncontaminated although periodic oscillations are observed for $0.4 < r/d < 0.8$. Evidently, the transition is absent since the jet is laminar at this axial location in microgravity. For Case 9, the Earth gravity image in Figure 4.45.2(a) shows repeatable structures contaminating the jet center. The structures in microgravity are significantly different as shown by the images in Figure 4.45.2(b). Overall, the images in Figure 4.45 reveal differences in the transient behavior of Earth gravity and microgravity jet flows to highlight the underlying effects of buoyancy.

4.3.3 Oscillating Flow Characteristics

A quantitative assessment of buoyancy effects on jet oscillations was conducted using fast Fourier transform analysis of the angular deflection data obtained from an ensemble of 256 images each in Earth gravity and microgravity. For each case, the power spectra are presented to show buoyancy effects in different regions of the jet. Figure 4.46.1(a) shows a dominant peak at a flow oscillation frequency (f) of 120 Hz for case 1 at z/d = 2.0 and r/d = 0.5, a location upstream of the transition plane in Earth gravity. In microgravity, the oscillatory mode still persists at this location but the spectral

power has decreased by two orders of magnitude as seen from Figure 4.46.1(b). The remarkable decrease in spectral power indicates that the flow oscillations subside in the absence of buoyancy. Results suggest that the formation and growth of toroidal vortices causing periodic oscillations is Earth gravity is inhibited in microgravity.

Figure 4.46.2(a) shows the power spectra in the transition region (z/d = 4.4, r/d = 0.5) for Case 6 in Earth gravity. The dominant frequency of 120Hz is the same as that in the upstream laminar regime, although the peak power has decreased by nearly an order of magnitude. Two smaller peaks representing sub-harmonics at 240Hz and 360Hz are also present, signifying the breakdown of large-scale structures in the transition region. Results show that the oscillating mode in Earth gravity is preserved in the transition region. In microgravity, Figure 4.46.2(b), the oscillation frequency is the same (i.e., 120Hz). The decrease of spectral power in microgravity is moderate at this downstream location (z/d = 4.4), suggesting that the flow has not fully adjusted to the microgravity environment within the limited drop period. For Case 9, the power spectra in Earth gravity, Figure 4.46.3(a), shows a dominant peak at a frequency of 215 Hz in the laminar region at z/d = 3.0 and r/d = 0.5. Note that the oscillation frequency in Earth gravity has increased with a decrease in the jet Richardson number. In microgravity, the oscillation frequency is the same although the spectral power has decreased by nearly two orders of magnitude, Figure 4.46.4(b). Figures 4.46.4(a)-(b) show the power spectra in the transition region (z/d = 5.4, r/d = 0.5) for Case 9. Again, a dominant frequency of 215 Hz is observed both in Earth gravity and microgravity. In Earth gravity, the spectral power in the transition region has decreased by more than an order of magnitude compared to that in the upstream location. Sub-harmonics at higher frequencies were not captured

because of the temporal resolution limitation. The spectral power has diminished in microgravity, signifying the importance of buoyancy on flow transition.

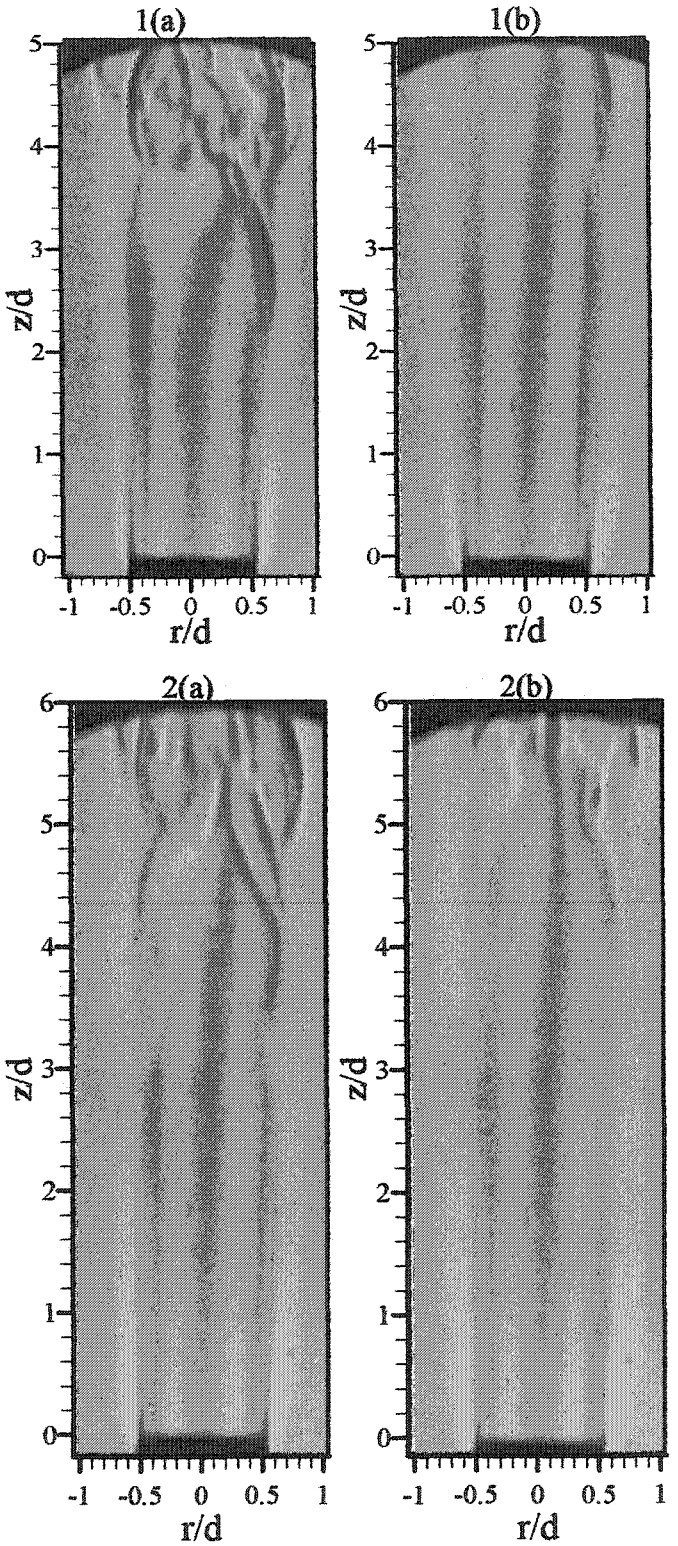


Figure 4.44: Rainbow schlieren images in Earth gravity (left) and microgravity (right). 1(a)-(b): Case 9 (Ri=0.02); 2(a)-(b): Case 6 (Ri=0.008)

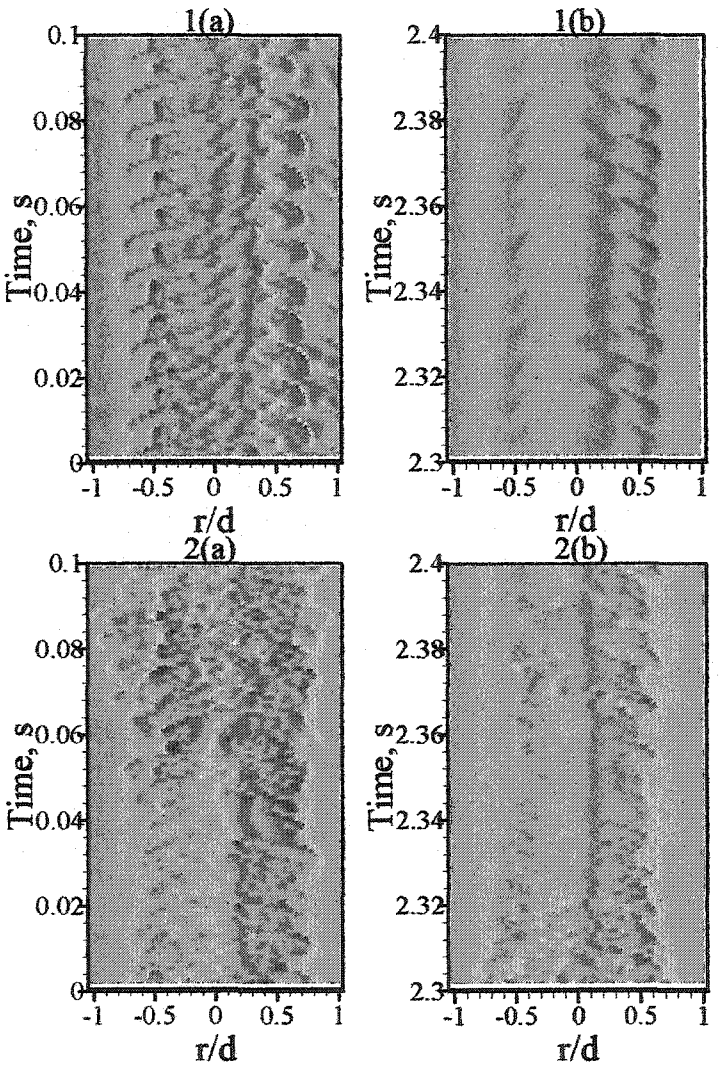


Figure 4.45: Spatio-temporal images in Earth gravity (left) and microgravity (right).
1(a)-(b): Case 9 (Ri=0.02), z/d=4.4; 2(a)-(b): Case 6, z/d=5.4(Ri=0.008)

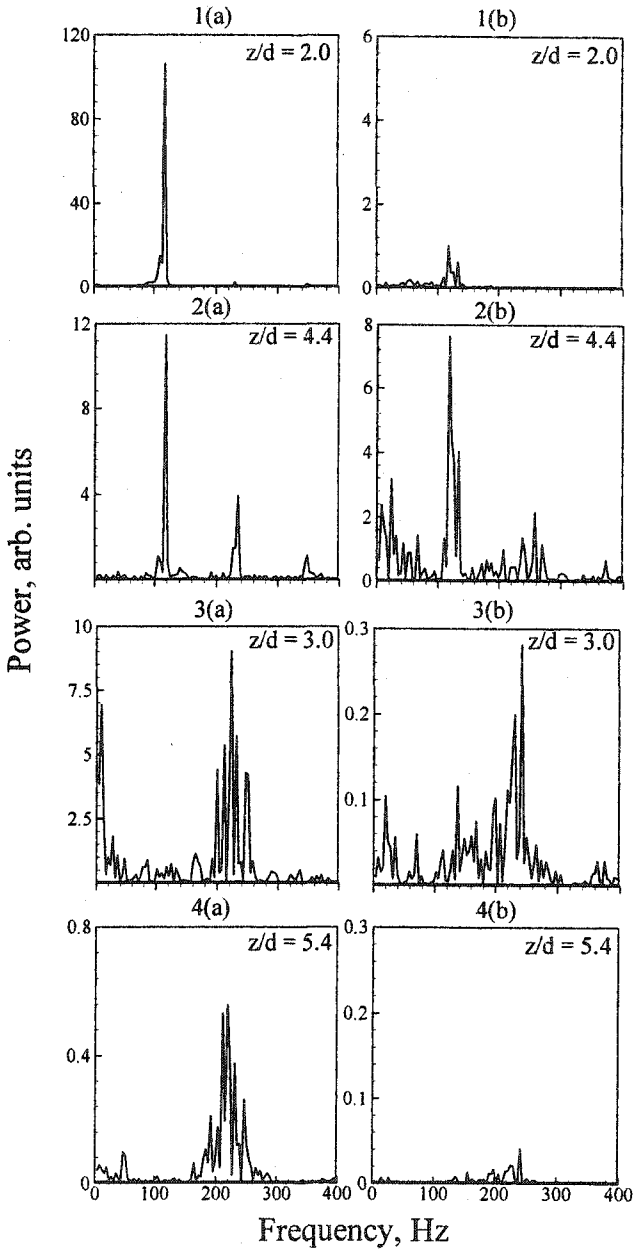


Figure 4.46: Power spectra of angular deflection data in Earth gravity (left) and microgravity (right) for r/d=0.5. 1-2: Case 9 (Ri=0.02); 3-4: Case 6 (Ri=0.008)

CHAPTER 5: LINEAR STABILITY ANALYSIS

5.1 Theory

Linear stability analysis was used to investigate the instability characteristics of a nonparallel axisymmetric jet with mean velocity and density profiles evolving slowly in the axial direction. The normal mode assumption ($p' = \hat{p}(r)e^{i(\tilde{k}\bar{z}-\tilde{\Omega}t)}$ where $\tilde{k}$ is the wavenumber and $\tilde{\Omega}$ is the frequency) was made for the disturbances and their radial dependence was then determined by a set of ordinary differential equations derived from the conservation equations coupled with the boundary conditions at the jet axis and a radial location far away from the jet centerline. An eigenvalue problem was posed with frequency, $\tilde{\Omega}$ as the eigenvalue. The eigenvalue solution of the problem depending on the mean flow velocity and density profiles, along with other relevant flow parameters and fluid properties, at any axial location can then be determined. For temporal stability analysis, the complex frequency eigenvalues were determined for specified real wavenumbers. For spatio-temporal stability analysis, both the frequency and wavenumber were considered complex. From spatio-temporal stability analysis, instability characteristics were determined along with the Briggs-Bers criterion (Briggs, 1964; Bers, 1975, 1983). The jet is said to be absolutely unstable when the complex frequency eigenvalue is a saddle point and its imaginary part is greater than zero. If its imaginary part is less than zero, the jet is convectively unstable.

5.2 Formulation

Consider a round jet (radius R) of a low-density gas (density ρ_j) injected vertically upward with velocity U_j into an ambient quiescent gas of density ρ_∞ at atmospheric

pressure. Representing the velocity components by $(\tilde{u},\tilde{v},\tilde{w})$, in cylindrical coordinates $(\tilde{z},\tilde{r},\phi)$ centered at the origin of the jet, and the conservation equations governing the flow are:

$$\frac{\partial\tilde{\rho}}{\partial t}+\frac{\partial(\tilde{\rho}\tilde{u})}{\partial\tilde{z}}+\frac{1}{\tilde{r}}\frac{\partial(\tilde{r}\tilde{\rho}\tilde{v})}{\partial\tilde{r}}+\frac{1}{\tilde{r}}\frac{\partial(\tilde{\rho}\tilde{w})}{\partial\phi}=0 \tag{5.2.1}$$

$$\tilde{\rho}\left[\frac{\partial\vec{v}}{\partial t}+\vec{v}\bullet\nabla\vec{v}\right]=-\nabla p+g(\rho_{\infty}-\tilde{\rho})\delta_{i1}+\nabla\bullet(\mu\nabla\vec{u}) \tag{5.2.2}$$

where g is the acceleration due to gravity, p is the pressure, and δ_{i1} is the Kronecker delta function with i = 1 representing the axial direction. The diffusion of the injected gas in the ambient gas medium is given in terms of the local mass fraction of the injected gas, Y_j (Gebhart, 1993):

$$\tilde{\rho}\left[\frac{\partial Y_j}{\partial t}+\vec{v}\bullet\nabla Y_j\right]=\nabla\bullet\left[\tilde{\rho}D_b\nabla Y_j\right] \tag{5.2.3}$$

where D_b is the binary diffusivity coefficient.

The flow is assumed locally non-parallel, and the variables are represented as the sum of the base state value and a fluctuation:

$$\begin{aligned}\tilde{u}&=\bar{u}(\tilde{r},\tilde{z})+u'\\ \tilde{v}&=v'\\ \tilde{p}&=p'\\ \tilde{\rho}&=\bar{\rho}(\tilde{r},\tilde{z})+\rho'\end{aligned} \tag{5.2.4}$$

The effects of viscosity on the large-scale structures in the near-injector region are negligible (Crow and Champagne, 1971). Substitution of equations (5.2.4) into equations (5.2.1) and (5.2.2), linearization, and the neglect of viscous and diffusive terms yields

$$\frac{\partial \rho'}{\partial t}+\frac{\partial(\bar{u}\rho')}{\partial \tilde{z}}+\frac{\partial(\bar{\rho}u')}{\partial \tilde{z}}+\frac{1}{\tilde{r}}\frac{\partial\left(\tilde{r}\bar{\rho}v'\right)}{\partial \tilde{r}}+\frac{\partial(\bar{u}\bar{\rho})}{\partial \tilde{z}}=0 \tag{5.2.5}$$

$$\bar{\rho}\left[\frac{\partial u'}{\partial t}+\bar{u}\frac{\partial u'}{\partial \tilde{z}}+v'\frac{d\bar{u}}{d\tilde{r}}+u'\frac{\partial \bar{u}}{\partial \tilde{z}}\right]+\rho'\bar{u}\frac{\partial \bar{u}}{\partial \tilde{z}}=-\frac{\partial p'}{\partial \tilde{z}}-g\rho' \tag{5.2.6}$$

$$\bar{\rho}\left[\frac{\partial v'}{\partial t}+\bar{u}\frac{\partial v'}{\partial \tilde{z}}\right]=-\frac{\partial p'}{\partial \tilde{r}} \tag{5.2.7}$$

The density of the mixture is related to the mass fraction by

$$\tilde{\rho}=\frac{\rho_j}{Y_j+\left(1-Y_j\right)S}$$

Rewriting Y_j in terms of ρ, we have

$$Y_j=\frac{1}{1-S}\left(\frac{\rho_j}{\tilde{\rho}}-S\right)$$

Therefore,

$$\frac{\partial Y_j}{\partial t}=-\frac{\rho_j}{\tilde{\rho}^2\left(1-S\right)}\frac{\partial \tilde{\rho}}{\partial t}$$

$$\frac{\partial Y_j}{\partial \tilde{z}}=-\frac{\rho_j}{\tilde{\rho}^2\left(1-S\right)}\frac{\partial \tilde{\rho}}{\partial \tilde{z}}$$

$$\frac{\partial Y_j}{\partial \tilde{r}}=-\frac{\rho_j}{\tilde{\rho}^2\left(1-S\right)}\frac{\partial \tilde{\rho}}{\partial \tilde{r}}$$

Substituting the above expressions in equation (5.2.3), we obtain

$$-\frac{\rho_j}{\tilde{\rho}\left(1-S\right)}\left(\frac{\partial \tilde{\rho}}{\partial t}+\vec{v}\bullet\nabla\tilde{\rho}\right)=\nabla\bullet\left[\left(-\frac{\rho_j}{\tilde{\rho}\left(1-S\right)}\right)D_b\nabla\tilde{\rho}\right] \tag{5.2.8}$$

The effects of viscosity and diffusivity on the large-scale structures in the near-injector region are negligible (Crow and Champagne, 1971). Neglecting the diffusive term, and linearizing equation (5.2.8), we obtain

$$\frac{\partial \rho'}{\partial t}+\bar{u}\frac{\partial \rho'}{\partial \tilde{z}}+v'\frac{\partial \bar{\rho}}{\partial \tilde{r}}+u'\frac{\partial \bar{\rho}}{\partial \tilde{z}}=0 \tag{5.2.9}$$

Normal mode disturbances are assumed given by

$$(u',v',p',\rho')=\left[\hat{u}(\tilde{r}),\hat{v}(\tilde{r}),\hat{p}(\tilde{r}),\hat{\rho}(\tilde{r})\right]e^{i\left(\tilde{k}\tilde{z}-\tilde{\Omega}t\right)} \tag{5.2.10}$$

where $i=\sqrt{-1}$; $\hat{u},\hat{v},\hat{p},\hat{\rho}$ are the amplitudes of the disturbances; $\tilde{k}$ is the wavenumber and $\tilde{\Omega}$ is the frequency. For temporal linear stability analysis, the wavenumber $\tilde{k}$ is real while the frequency $\tilde{\Omega}=\tilde{\Omega}_r+i\tilde{\Omega}_i$ is complex. The real part $\tilde{\Omega}_r$ is proportional to the disturbance frequency and the imaginary part $\tilde{\Omega}_i$ is the temporal growth rate of the disturbance. The disturbance gets amplified if $\tilde{\Omega}_i$ is positive. The ratio of $\tilde{\Omega}_r$ to k represents the wave speed, c_{ph} of the disturbance.

Substituting the expressions (5.2.10) in equations (5.2.5), (5.2.6), (5.2.7) and (5.2.9), we obtain

$$\hat{\rho}\left(i\left(\tilde{k}\bar{u}-\tilde{\Omega}\right)+\frac{\partial \bar{u}}{\partial \tilde{z}}\right)+\hat{u}\left(i\tilde{k}\bar{\rho}+\frac{\partial \bar{\rho}}{\partial \tilde{z}}\right)+\bar{\rho}\frac{\partial \hat{v}}{\partial \tilde{r}}+\frac{\bar{\rho}\hat{v}}{\tilde{r}}+\hat{v}\frac{\partial \bar{\rho}}{\partial \tilde{r}}=0 \tag{5.2.11}$$

$$\bar{\rho}\left[\hat{u}\left(i\left(\tilde{k}\bar{u}-\tilde{\Omega}\right)+\frac{\partial \bar{u}}{\partial \tilde{z}}\right)+\hat{v}\frac{\partial \bar{u}}{\partial \tilde{r}}\right]=-i\tilde{k}\hat{p}-\hat{\rho}\left(g+\bar{u}\frac{\partial \bar{u}}{\partial \tilde{z}}\right) \tag{5.2.12}$$

$$i\bar{\rho}\left(\tilde{k}\bar{u}-\tilde{\Omega}\right)\hat{v}=-\frac{\partial \hat{p}}{\partial \tilde{r}} \tag{5.2.13}$$

$$\hat{\rho}\left(i\left(\tilde{k}\bar{u}-\tilde{\Omega}\right)\right)+\hat{v}\frac{\partial \bar{\rho}}{\partial \tilde{r}}+\hat{u}\frac{\partial \bar{\rho}}{\partial \tilde{z}}=0 \tag{5.2.14}$$

Let,

$$C_1=i\bar{\rho}\left(\tilde{k}\bar{u}-\tilde{\Omega}\right)$$

$$C_2=\frac{C_1}{\bar{\rho}}+\frac{\partial \bar{u}}{\partial \tilde{z}}=i\left(\tilde{k}\bar{u}-\tilde{\Omega}\right)+\frac{\partial \bar{u}}{\partial \tilde{z}}$$

$$C_3 = i\bar{\rho}\tilde{k} + \frac{\partial \bar{\rho}}{\partial \tilde{z}}$$

$$C_4 = C_1 + \bar{\rho}\frac{\partial \bar{u}}{\partial \tilde{z}} = i\bar{\rho}\left(\tilde{k}\bar{u} - \tilde{\Omega}\right) + \bar{\rho}\frac{\partial \bar{u}}{\partial \tilde{z}}$$

$$C_5 = \bar{u}\frac{\partial \bar{u}}{\partial \tilde{z}} + g$$

$$C_6 = \frac{C_1}{\bar{\rho}} = i\left(\tilde{k}\bar{u} - \tilde{\Omega}\right)$$

$$C_7 = C_4 - \frac{C_5}{C_6}\bar{\rho}\frac{\partial \bar{\rho}}{\partial \tilde{z}} = i\bar{\rho}\left(\tilde{k}\bar{u} - \tilde{\Omega}\right) + \bar{\rho}\frac{\partial \bar{u}}{\partial \tilde{z}} - \frac{\bar{u}\dfrac{\partial \bar{u}}{\partial \tilde{z}} - g}{i\left(\tilde{k}\bar{u} - \tilde{\Omega}\right)}\frac{\partial \bar{\rho}}{\partial \tilde{z}}$$

Substituting the above in the equations (5.2.11 – 5.2.14), we obtain

$$\hat{v} = -\frac{1}{C_1}\frac{\partial \hat{p}}{\partial \tilde{r}} \tag{5.2.15}$$

$$\frac{\partial \hat{v}}{\partial \tilde{r}} = \frac{1}{C_1^{\,2}}\frac{\partial C_1}{\partial \tilde{r}}\frac{d\hat{p}}{d\tilde{r}} - \frac{1}{C_1}\frac{\partial^2 \hat{p}}{\partial \tilde{r}^2} \tag{5.2.16}$$

$$\hat{\rho}C_2 + \hat{v}\left(\frac{\bar{\rho}}{\tilde{r}} + \frac{\partial \bar{\rho}}{\partial \tilde{r}}\right) + \hat{u}C_3 + \bar{\rho}\frac{\partial \hat{v}}{\partial \tilde{r}} = 0 \tag{5.2.17}$$

$$-\hat{\rho}C_5 + \hat{v}\bar{\rho}\frac{\partial \bar{u}}{\partial \tilde{r}} + \hat{u}C_4 = -i\tilde{k}\hat{p} \tag{5.2.18}$$

$$\hat{\rho}C_6 + \hat{v}\frac{\partial \bar{\rho}}{\partial \tilde{r}} + \hat{u}\frac{\partial \bar{\rho}}{\partial \tilde{z}} = 0 \tag{5.2.19}$$

From equation (5.2.19)

$$\hat{\rho} = -\frac{1}{C_6}\left(\hat{v}\frac{\partial \bar{\rho}}{\partial \tilde{r}} + \hat{u}\frac{\partial \bar{\rho}}{\partial \tilde{z}}\right) \tag{5.2.20}$$

Substituting equations (5.2.15) and (5.2.20) in equation (5.2.18) and rearranging, we obtain

$$\hat{u} = -\frac{1}{C_7}\left(i\tilde{k}\hat{p} - \frac{1}{C_1}\frac{\partial \hat{p}}{\partial \tilde{r}}\left[\bar{\rho}\frac{\partial \bar{u}}{\partial \tilde{r}} - \frac{C_5}{C_6}\frac{\partial \bar{\rho}}{\partial \tilde{r}} \right] \right)$$

$$= -\frac{\left(i\tilde{k}\hat{p} - \frac{1}{i\bar{\rho}\left(\tilde{k}\bar{u} - \tilde{\Omega}\right)}\frac{\partial \hat{p}}{\partial \tilde{r}}\left[\bar{\rho}\frac{\partial \bar{u}}{\partial \tilde{r}} - \frac{\bar{u}\frac{\partial \bar{u}}{\partial \tilde{z}} + g}{i\left(\tilde{k}\bar{u} - \tilde{\Omega}\right)}\frac{\partial \bar{\rho}}{\partial \tilde{r}} \right] \right)}{i\bar{\rho}\left(\tilde{k}\bar{u} - \tilde{\Omega}\right) + \bar{\rho}\frac{\partial \bar{u}}{\partial \tilde{z}} - \frac{\bar{u}\frac{\partial \bar{u}}{\partial \tilde{z}} + g}{i\left(\tilde{k}\bar{u} - \tilde{\Omega}\right)}\frac{\partial \bar{\rho}}{\partial \tilde{z}}} \qquad (5.2.21)$$

Let

$$C_8 = \left[\bar{\rho}\frac{\partial \bar{u}}{\partial \tilde{r}} - \frac{C_5}{C_6}\frac{\partial \bar{\rho}}{\partial \tilde{r}} \right] = \left[\bar{\rho}\frac{\partial \bar{u}}{\partial \tilde{r}} - \frac{\bar{u}\frac{\partial \bar{u}}{\partial \tilde{z}} + g}{i\left(\tilde{k}\bar{u} - \tilde{\Omega}\right)}\frac{\partial \bar{\rho}}{\partial \tilde{r}} \right] \qquad (5.2.22)$$

Substituting in equation (5.2.20), we obtain

$$\hat{\rho} = -\frac{1}{C_6}\left(\hat{v}\frac{\partial \bar{\rho}}{\partial \tilde{r}} + \hat{u}\frac{\partial \bar{\rho}}{\partial \tilde{z}} \right)$$

$$= \frac{\frac{1}{i\bar{\rho}\left(\tilde{k}\bar{u} - \tilde{\Omega}\right)}\frac{\partial \hat{p}}{\partial \tilde{r}}\frac{\partial \bar{\rho}}{\partial \tilde{r}}}{i\left(\tilde{k}\bar{u} - \tilde{\Omega}\right)}$$

$$+ \frac{\left(i\tilde{k}\hat{p} - \frac{1}{i\bar{\rho}\left(\tilde{k}\bar{u} - \tilde{\Omega}\right)}\frac{\partial \hat{p}}{\partial \tilde{r}}\left[\bar{\rho}\frac{\partial \bar{u}}{\partial \tilde{r}} - \frac{\bar{u}\frac{\partial \bar{u}}{\partial \tilde{z}} + g}{i\left(\tilde{k}\bar{u} - \tilde{\Omega}\right)}\frac{\partial \bar{\rho}}{\partial \tilde{r}} \right] \right)}{\left(i\left(\tilde{k}\bar{u} - \tilde{\Omega}\right) \right)\left(i\bar{\rho}\left(\tilde{k}\bar{u} - \tilde{\Omega}\right) + \bar{\rho}\frac{\partial \bar{u}}{\partial \tilde{z}} - \frac{\bar{u}\frac{\partial \bar{u}}{\partial \tilde{z}} + g}{i\left(\tilde{k}\bar{u} - \tilde{\Omega}\right)}\frac{\partial \bar{\rho}}{\partial \tilde{z}} \right)}\frac{\partial \bar{\rho}}{\partial \tilde{z}}$$

$$= \frac{i\tilde{k}\bar{\rho}\dfrac{\partial\bar{\rho}}{\partial\tilde{z}}}{\left(i\left(\tilde{k}\bar{u}-\tilde{\Omega}\right)\right)\left(i\bar{\rho}\left(\tilde{k}\bar{u}-\tilde{\Omega}\right)+\bar{\rho}\dfrac{\partial\bar{u}}{\partial\tilde{z}}-\dfrac{\bar{u}\dfrac{\partial\bar{u}}{\partial\tilde{z}}+g}{i\left(\tilde{k}\bar{u}-\tilde{\Omega}\right)}\dfrac{\partial\bar{\rho}}{\partial\tilde{z}}\right)}\hat{p}$$

$$+\frac{\left[\dfrac{\partial\bar{\rho}}{\partial\tilde{r}}+\dfrac{\partial\bar{\rho}}{\partial\tilde{z}}\dfrac{\left[\bar{\rho}\dfrac{\partial\bar{u}}{\partial\tilde{r}}-\dfrac{\bar{u}\dfrac{\partial\bar{u}}{\partial\tilde{z}}+g}{i\left(\tilde{k}\bar{u}-\tilde{\Omega}\right)}\dfrac{\partial\bar{\rho}}{\partial\tilde{r}}\right]}{\left(i\bar{\rho}\left(\tilde{k}\bar{u}-\tilde{\Omega}\right)+\bar{\rho}\dfrac{\partial\bar{u}}{\partial\tilde{z}}-\dfrac{\bar{u}\dfrac{\partial\bar{u}}{\partial\tilde{z}}+g}{i\left(\tilde{k}\bar{u}-\tilde{\Omega}\right)}\dfrac{\partial\bar{\rho}}{\partial\tilde{z}}\right)}\right]}{\left(i\bar{\rho}\left(\tilde{k}\bar{u}-\tilde{\Omega}\right)\right)\left(i\left(\tilde{k}\bar{u}-\tilde{\Omega}\right)\right)}\frac{\partial\hat{p}}{\partial\tilde{r}}$$

$$= \frac{i\tilde{k}\dfrac{\partial\bar{\rho}}{\partial\tilde{z}}}{C_6C_7}\hat{p}+\frac{1}{C_1C_6}\left[\frac{\partial\bar{\rho}}{\partial\tilde{r}}-\frac{C_8}{C_7}\frac{\partial\bar{\rho}}{\partial\tilde{z}}\right]\frac{\partial\hat{p}}{\partial\tilde{r}}$$

Substituting for $\hat{u},\hat{v},\hat{\rho}$ in equation (5.2.17) and rearranging, we obtain the pressure-disturbance equation as

$$-\frac{\bar{\rho}}{C_1}\frac{\partial^2\hat{p}}{\partial\tilde{r}^2}+\frac{i\tilde{k}}{C_7}\left(-C_3+\frac{C_2}{C_6}\frac{\partial\bar{\rho}}{\partial\tilde{z}}\right)\hat{p}$$
$$+\left(-\frac{1}{C_1}\left[\frac{\bar{\rho}}{\tilde{r}}+\frac{\partial\bar{\rho}}{\partial\tilde{r}}\right]+\frac{1}{C_1}\frac{C_2}{C_6}\frac{\partial\bar{\rho}}{\partial\tilde{r}}+\frac{\bar{\rho}}{C_1^{\,2}}\frac{\partial C_1}{\partial\tilde{r}}+\frac{C_8}{C_1C_7}\left[C_3-\frac{C_2}{C_6}\frac{\partial\bar{\rho}}{\partial\tilde{z}}\right]\right)\frac{d\hat{p}}{d\tilde{r}}=0 \qquad (5.2.24)$$

For locally radial jet flow,

$$\frac{\partial\bar{\rho}}{\partial\tilde{z}}=0,\frac{\partial\bar{u}}{\partial\tilde{z}}=0$$

The disturbance equation reduces to

$$\bar{\rho}\frac{\partial^2\hat{p}}{\partial\tilde{r}^2}-\bar{\rho}\tilde{k}^2\hat{p}$$
$$-\left(-\frac{\bar{\rho}}{\tilde{r}}+\left[1+\frac{ig\tilde{k}}{\left(\tilde{k}\bar{u}-\tilde{\Omega}\right)^2}\right]\frac{\partial\bar{\rho}}{\partial\tilde{r}}+\frac{2\bar{\rho}\tilde{k}}{\left(\tilde{k}\bar{u}-\tilde{\Omega}\right)}\frac{\partial\bar{u}}{\partial\tilde{r}}\right)\frac{d\hat{p}}{d\tilde{r}}=0$$

This was the equation obtained by Lawson (2000). In addition, if the density gradient is zero in the equation (5.2.24), then it reduces to the equation used by Michalke and Hermann (1982) for investigating the instability of constant-density jets. Further, if $r\to\infty$ and the effect of gravity is neglected, equation (5.2.24) turns into the equation used by Yu and Monkewitz (1990) for the instability analysis of inertial jets. The present analysis differs from that of Michalke (1982) and Monkewitz (1990) by considering buoyancy and non-parallel effects in the disturbance equation.

The variables are nondimensionalized as follows

$$P=\frac{\hat{p}}{\rho_\infty U_j^2} \qquad Fr^2=\frac{U_j^2}{gR}\frac{\rho_j}{\rho_\infty-\rho_j}$$

$$r=\frac{\tilde{r}}{R} \qquad z=\frac{\tilde{z}}{2R}$$

$$\Omega=\frac{\tilde{\Omega}R}{U_j} \qquad k=\tilde{k}R$$

$$U=\frac{\bar{u}}{U_j} \qquad \rho=\frac{\bar{\rho}}{\rho_\infty}$$

The boundary condition that had to be satisfied by the disturbance is,

$$\hat{p}(0) \text{ is finite} \quad \text{when } m=0; \tag{5.2.25}$$

By specifying the mean velocity and density profiles, equation (5.2.24) was solved for the eigenvalues that satisfied the boundary conditions given by equation

(5.2.25). Since $\frac{\partial \bar{u}}{\partial r}$, $\frac{\partial \bar{u}}{\partial z}$, $\frac{\partial \bar{\rho}}{\partial r}$ and $\frac{\partial \bar{\rho}}{\partial z}$ vanish as $r \to 0$ and $r \to \infty$, asymptotic solutions for the equation (5.2.24) were sought. The asymptotic solutions that satisfy the boundary conditions (5.2.25) are,

$$\hat{p}^{(i)} = C_1 I_m(kr) \tag{5.2.26}$$

$$\hat{p}^{(o)} = C_2 K_m(kr) \tag{5.2.27}$$

where the superscripts i and o represent the inner and outer solutions respectively. The inner solution is valid close to the jet centerline and the outer solution is valid in the far field. Here I_m and K_m are the modified Bessel functions of order m and C_1 and C_2 are the arbitrary constants.

The basic jet velocity profile, U(r,z), was obtained by combining the mean velocity profile given by Michalke and Hermann (1982) and relation between the jet momentum shear layer thickness and the axial distance from the jet exit given by Crighton and Gaster (1976),

$$U(r,z) = 0.5\left\{1 - \tanh\left[0.25\left(\frac{100}{3z+4}\right)\left(r - \frac{1}{r}\right)\right]\right\} \tag{5.2.28}$$

The values of the jet parameter used in this study are z = 0, 1 and 2.67. This is within the potential core of the jet and allows for the effects of buoyancy to manifest as the jet proceeds downstream. A hyperbolic tangent profile was assumed for the basic density profile in the shear layer,

$$\rho = 1 + (S-1)\left\{0.5\left(1 - \tanh\left[0.25\left(\frac{100}{3z+4}\right)\left(r - \frac{1}{r}\right)\right]\right)\right\} \tag{5.2.29}$$

5.3 Method of Solution

To solve the disturbance equation (5.2.24), a fourth-order Runge-Kutta scheme

with automatic step-size control was used to integrate the equation. The infinite integration domain, $0 < r < \infty$ was divided into two finite domains: an inner domain $R \geq r \geq 0$ and an outer domain $r_\infty \geq r \geq R$, where R is the jet radius and r_∞ is a specified large radius where the gradients of the velocity and density are small. A shooting method was used to determine $\Omega(k)$ such that both P and $\frac{dP}{dr}$ are continuous at r = R. A parabolic complex zero-search procedure was used to vary Ω for a specified k until the matching conditions were satisfied to a minimum accuracy within 10^{-10}. Fortran 90/95 computer programs were used to solve the eigenvalue problem. The Briggs-Bers criterion (Briggs, 1964; Bers, 1975, 1983) was used to determine the nature of the instability (whether absolute or convective) by determining the saddle points in the complex (Ω, k) domain and verifying the satisfaction of the pinching requirements. This was accomplished using the mesh-searching technique described by Li and Shen (1996). For axisymmetric jet flows, Lawson (2000) and Vedantam (2003) have applied this method of solution extensively for different test conditions. The steps involved in this technique are explained in the next sections.

To select the appropriate ranges, the temporal stability solution was first determined. If there is a pinch point, $k^o = k_r^o + ik_i^o$ within the region selected, the corresponding growth rate, Ω_i^o of the absolute instability will be less than or equal to the maximum temporal disturbance growth rate, $\Omega_{i,max}^t$ (Bers, 1983) and the real part of the pinch point, k_r^o will be less than or equal to the wavenumber corresponding to neutral stability, $k_{r,c}^t$ (Li and Shen, 1996). Thus, the estimates for the k region were determined using the wavenumber corresponding to neutral stability, $k_{r,c}^t$ and the maximum temporal

disturbance growth rate, $\Omega_{i,max}^{t}$. Therefore, Ω^{o} will lie in either the first or fourth quadrants of the Ω-plane, while k^{o} will lie in the fourth quadrant of the k-plane .

The disturbance equation (5.2.24) was solved numerically within the appropriate search region in the k-plane. Complex wavenumbers were specified and the corresponding complex frequency eigenvalue solutions were determined. This was done by starting at wavenumbers with $k_i^t = 0$ (the temporal stability solution) and decreasing the value k_i for several k_r within the search region. A contour plot of various constant Ω_r or Ω_i on the k-plane was used to determine the saddle point, Ω^{o}. The saddle point is the point within the Ω_r or Ω_i domain, which is a minimum along the k_r-axis and a maximum along the k_i-axis, or vice versa. Mathematically, the saddle point can be obtained from

$$\frac{D\Omega}{Dk} = \frac{\partial \Omega_r}{\partial k_r} - i\frac{\partial \Omega_r}{\partial k_i} = 0 \tag{5.2.30}$$

or

$$\frac{D\Omega}{Dk} = \frac{\partial \Omega_i}{\partial k_r} + i\frac{\partial \Omega_i}{\partial k_i} = 0 \tag{5.2.31}$$

In this study, the saddle points were determined by inspection of the contour plots. The same contour plot of various constant Ω_r on the k-plane from the previous step was used to determine the pinch point, k^{o}. The pinch points are double roots in k. If two k-roots merge to k^{o} from opposite sides of the k_r-axis or k_i-axis as Ω tends to Ω^{o} from above $\Omega_{i,max}^{t}$, k^{o} is a pinch point. For normal mode disturbance, any disturbance variable q' is represented as given in equation (5.2.10) by

$$q' = \hat{q}(r)e^{i\left[(k_r+ik_i)z-(\Omega_r+i\Omega_i)t\right]}$$

$$\therefore q' = \left[\hat{q}(r)e^{(\Omega_i t-k_i z)}\right]e^{i[k_r z-\Omega_r t]} \tag{5.2.33}$$

Thus, for negative k_i the flow system is said to be absolutely unstable if $\Omega_i^o > 0$ (since the amplitude of the disturbance will grow with time and space), otherwise it is convectively unstable.

5.4 Results of Stability Analysis

The results of spatio-temporal linear stability analysis of buoyancy effects on low-density jets are presented. Qualitative comparison between the experimental and stability analysis results is made. It is customary to use the parallel flow approximation to describe the linear instability of jet flows to small amplitude disturbances. In spite of the qualitative success of this assumption, parallel stability theory does not explain some important systematic differences with experiments. The velocity profile used in the stability analysis is shown in Figure 5.1 for helium jet (S = 0.14) at z/2R = 1. The hyper-tan or "top-hat" profile is one of the more commonly used velocity profiles in the stability analyses. The density hyper-tan profile is shown at various axial locations in Figure 5.2. Experimental density profiles of steady helium jet obtained from RSD are shown at different axial locations in Figure 5.3 along with the hyper-tan profile at z/d = 2.0. The signal-to-noise ratio is poor at the center leading to poor sensitivity. The hyper-tan density profiles compare qualititatively well with the experimental profiles.

In this section, the results of linear temporal and absolute stability analysis of simple non-parallel flows are discussed. The effects of buoyancy, density ratio and streamwise location on the nature of the varicose instability mode (convective or absolute) are presented for the assumed hyperbolic tangent velocity and density profiles. The focus of the stability analysis was to remove the flow parallelism and analyze the

stability characteristics of low-density jets on the lines of Lawson (2001) and Vedantam (2003). Comparison with the experimental results will be provided at the end.

5.4.1 Temporal Stability Analysis

Temporal stability analysis was carried out to investigate the effects of the inhomogeneous shear-layer and buoyancy on the evolution of the disturbances with time and to determine the limits in the complex wavenumber k-plane for the mesh-searching process used to determine the saddle points for the absolute stability analysis.

The near-injector region was investigated at two axial locations $\frac{z}{2R}=1$ and $\frac{z}{2R}=2.67$. The density ratio, $S=\frac{\rho_j}{\rho_\infty}$, was varied from 0.7 to 0.14 (helium jet discharged into air), while varying the Richardson number from zero to 1. The imaginary part of the complex frequency, Ω_i, is the temporal growth rate of the amplitude of the disturbance wave. The wavenumber k is the reciprocal of the wavelength. The temporal growth rate, Ω_i, the phase velocity, c_{ph}, and the wavenumber k were normalized using the jet radius R and the jet exit velocity U_j.

5.4.1.1 Effect of Density Ratio

In order to investigate the effect of an inhomogeneous shear layer only on the evolution of the jet instabilities with time, the Richardson number was fixed at zero (negligible gravity effect) and the density ratio (S) was varied from 0.7 to 0.14.

The variation of the normalized temporal growth rate of the instabilities with the normalized wavenumber at $\frac{z}{2R}=1$ and $\frac{z}{2R}=2.67$ is presented in Figures 5.4-5.7 at Ri = 0.01 and Ri = 0. Note that the normalized wavenumber is equal to the ratio of the

circumference of a jet of radius equal to the shear-layer momentum thickness to the disturbance wavelength. At $\frac{z}{2R}=1$, as the density ratio is reduced from 0.7 to 0.14, the range of unstable temporal growth rates has increased by about 20%. A decrease in the jet density results in the steep density gradients in the jet shear layer, which leads to additional generation of vorticity and enhanced mixing levels, thus causing an increase in the disturbance growth rate. In addition, the maximum growth rate occurs at a higher wavenumber with a decrease in the density ratio. Lower temporal growth rates at higher density ratios indicate diminished mixing levels due to absence of steep density gradients.

As the jet proceeds downstream from $\frac{z}{2R}=1$ to $\frac{z}{2R}=2.67$, the disturbance growth rates for the constant density jet decrease by more than 50% as seen from Figures 5.6 and 5.7. This significant drop in temporal growth rates is much higher that that reported by Lawson (2001) and might be due to the non-parallel flow assumption, which accounts for additional mixing and jet widening. This result implies that the growth rate of the disturbance wave is a function of both the density ratio and the downstream location.

5.4.1.2 Effect of Buoyancy

The effects of buoyancy on the jet temporal instability were determined by considering non-zero values of the Ri in the analysis. To study the effect of buoyancy on the jet temporal instability the density ratio was fixed at 0.14 (corresponding to a helium jet injected into air), while the Ri was varied from zero to 1. Figures 5.8 and 5.9 display the variation of the temporal growth rates with wavenumber at the two axial locations $\frac{z}{2R}=1$ and $\frac{z}{2R}=2.67$ respectively, as the Ri is varied from zero to 1. When

the effect of changing the Richardson number alone is considered, no significant change in the wavenumber corresponding to the maximum growth rate is observed, except for Ri = 1 at $\frac{z}{2R} = 2.67$ where the temporal growth rate registers an increase of about 50%. For all values of Ri < 1, the temporal growth curves fall on the same curve.

In Figure 5.9, at $\frac{z}{2R} = 2.67$, there is a significant drop in growth rates when compared to those in Figure 5.1.3 at $\frac{z}{2R} = 1$. In addition, the enhanced growth rates observed at Ri = 1 is due to the buoyancy-induced acceleration as discussed in buoyancy-dominated jets previously. Even though the gravitational acceleration is not a component of the assumed mean profiles, the jump observed in temporal growth rates at Ri = 1 can be attributed to buoyancy based on experimental data.

5.4.2 Absolute Stability Analysis

Spatio-temporal stability analysis was carried out to determine the absolute instability of the jet. The effects of the inhomogeneous shear-layer and buoyancy on the nature of the absolute instability (whether absolutely or convectively unstable) of the jet were investigated. This was done by first studying the effect of varying the density ratio from 0.7 to 0.14, while varying the Richardson number from zero to 1. Previous results of two-dimensional jets (Raynal et al., 1996; Lawson, 2001; Vedantam, 2003) indicate that the shift in the velocity and density profiles may have a significant effect on the instabilities. In addition, all those previous stability studies have assumed parallel flow. The effects of non-parallel flow on instability growth rates have already been seen in temporal stability analysis. The effects of the non-parallel flow assumption, density ratio

and buoyancy on the nature of the instability (convective or absolute) were investigated and finally, the results of the spatio-temporal stability analysis were compared to the RSD experimental findings reported earlier. The complex frequency Ω and the complex wavenumber k are normalized using the jet radius R and the velocity difference U_j.

5.4.2.1 Effect of Density Ratio

In the absolute stability analysis, the imaginary parts Ω_i^o and k_i^o of the complex absolute frequency and wavenumber denote the absolute temporal and spatial growth rates of the disturbances. When Ω_i^o is positive (and the Briggs-Bers criterion is satisfied) the jet is absolutely unstable while for a negative Ω_i^o the jet may be convectively unstable. A constant-density jet (such as an air-in-air jet) may be convectively unstable; as the density ratio is reduced (a low-density jet injected into a high-density gas medium), the nature of instability of the jet is changed from convective instability to absolute instability. A negative k_i^o indicates the absolute spatial growth rate of the disturbances while a positive k_i^o denotes the absolute spatial decaying rate of the disturbances. It should be noted that the word "absolute" when used in conjunction with the disturbance wavenumber or growth rate in this study is synonymous with the phenomenon of global oscillating absolute instability used by Subbarao and Cantwell (1991), Richards et al. (1995) and by Kyle and Sreenivasan (1993).

Figure 5.10 depicts the variation of the absolute temporal growth rate of the disturbances with the density ratio at $\frac{z}{2R} = 1$ for Ri = 1 and 10. For both the cases, a positive value of absolute instability was detected, confirming the existence of oscillatory instability at all density ratios. For the buoyancy-dominated case Ri = 1, the growth rate

remains unchanged with density ratio. However, at Ri = 0.01, a monotonic decrease is observed in the absolute temporal growth rate. The absolute spatial growth rates shown in Figure 5.11 for Ri = 1 and 10 follow similar progression with varying density ratio.

5.4.2.2 Effect of Buoyancy

Figures 5.12 and 5.13 illustrate the variation of the absolute temporal and spatial growth rate of the disturbances at Ri = 0 at two downstream locations. At both locations, a negative absolute temporal growth rate was observed indicating a possibility of existence of convective instability and absence of absolute instability observed for Ri = 1 and 0.01. As buoyancy is removed, the instability is no more of the absolute type indicating the existing instability is buoyancy-driven. The stability growth rates remain unchanged with density ratio. In the near-injector region, at $\frac{z}{2R}=1$, high spatial growth rates are observed than at the downstream location $\frac{z}{2R}=2.67$ even upon removal of buoyancy forces.

5.5 Comparisons with Experimental Data

Figures 5.14 and 5.15 show the variation of absolute temporal growth rate with varying Ri and at Ri = 0 respectively for the case of S = 0.14 (helium jet in air). For Ri = 10^{-6}, a positive absolute temporal instability growth rate is observed at $\frac{z}{2R}=1$ and $\frac{z}{2R}=2.67$ respectively. This case corresponds to the momentum-dominated regime, similar to the work of Kyle and Sreenivasan (1991). But, no absolute instability is seen in Figure 5.15 at both locations, at Ri = 0. Damping of oscillations in microgravity was observed at Ri = 0.002 and all other cases. Similarly, the pattern remains same for all

other Fr in Figures 5.14 and 5.15 conclusively establishing the fact that the instability in low-density gas jets is indeed buoyancy driven.

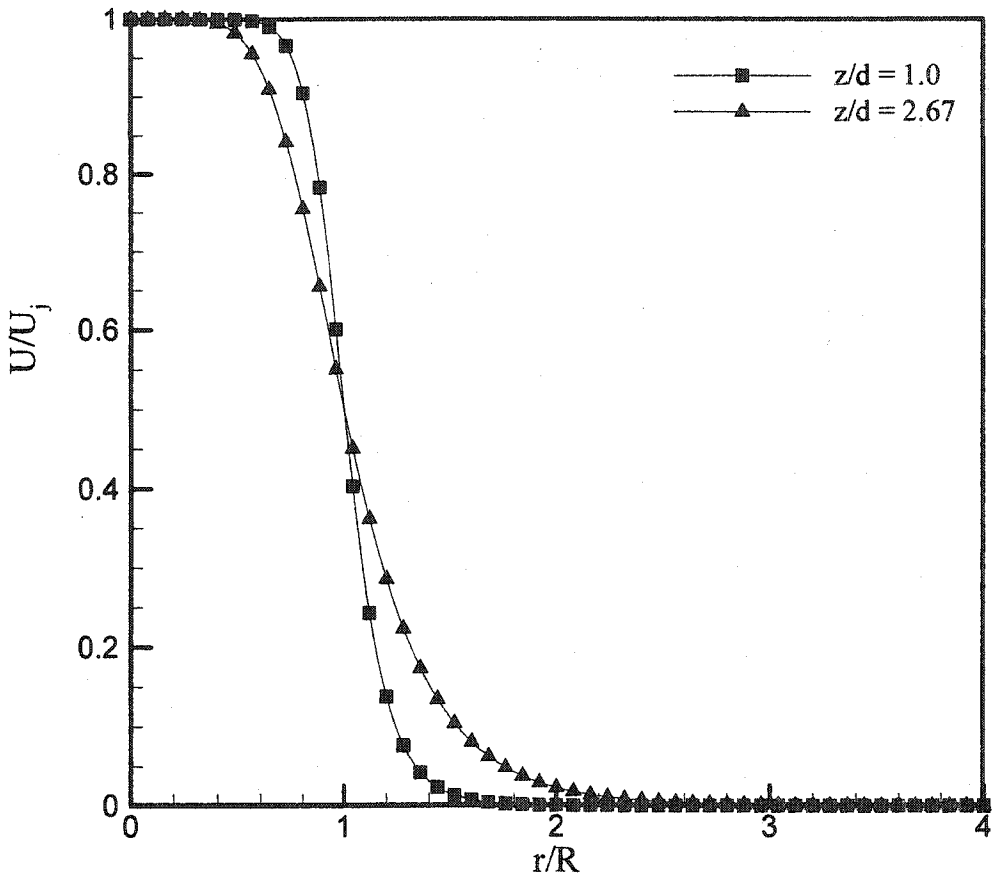


Figure 5.1: Nondimensionalized basic jet velocity profile for S = 1 at z/d = 1 and 2.67. (Adapted from Lawson (2001)). Here d = 2R.

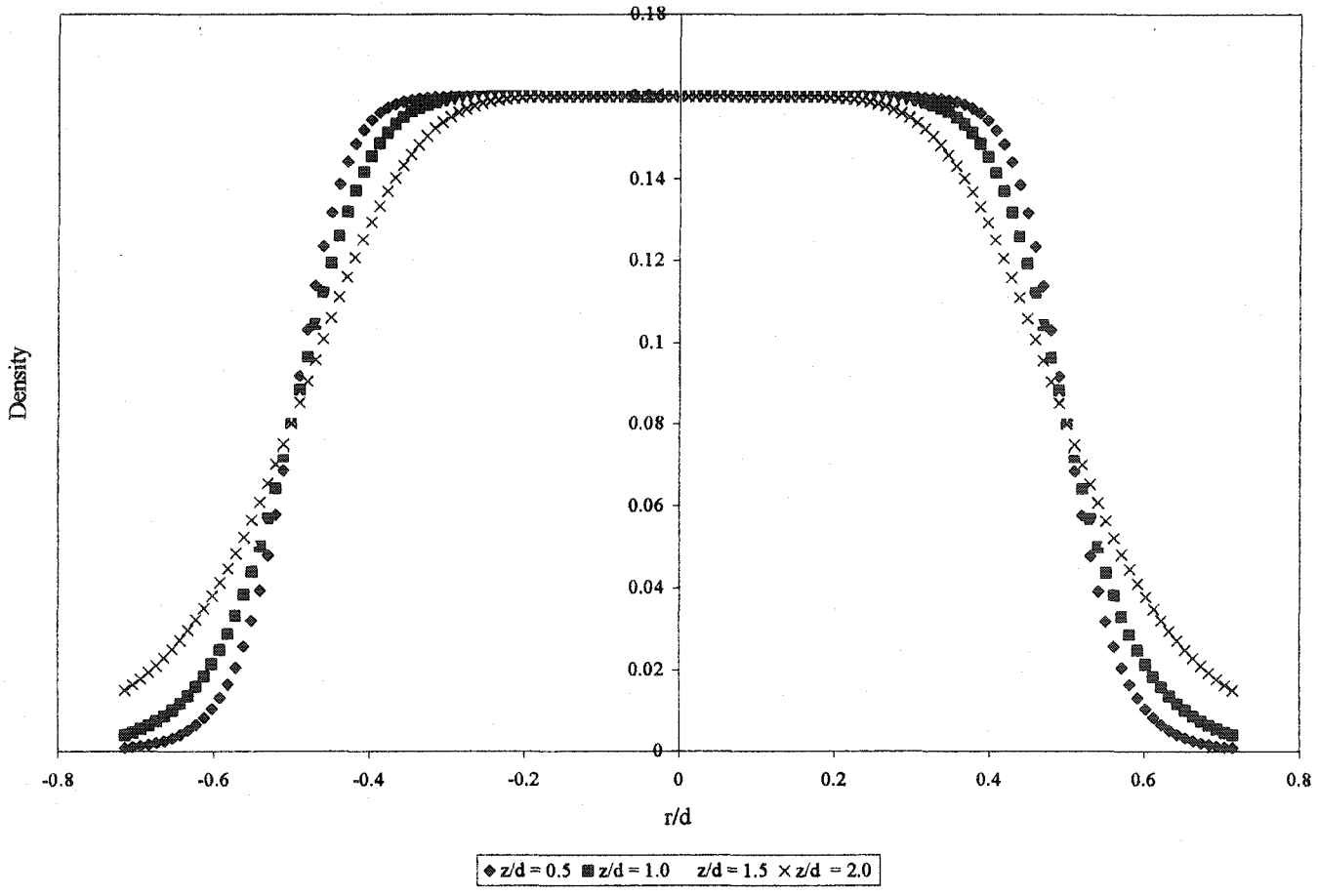


Figure 5.2: Nondimensionalized basic jet density profile for S = 0.14 at different axial locations. z/d represents the non-dimensionlized axial distance from jet exit where z is the axial distance from jet exit and d = 2R, R is the jet radius at z.

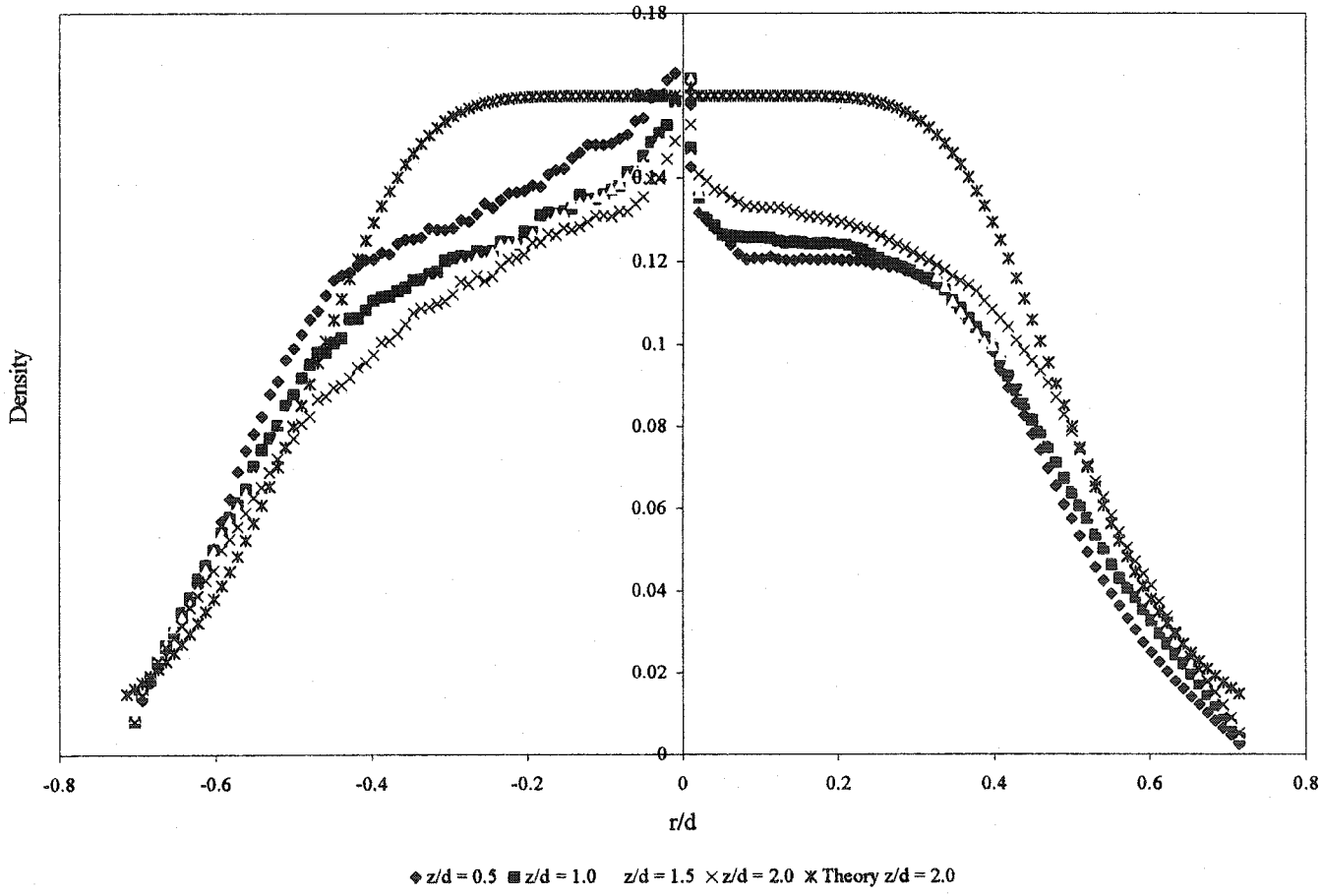


Figure 5.3: Comparison of experimental and assumed hyper-tan jet density profiles for S = 0.14 at z/d =2.0. Experimental profiles are shown for a steady jet at different axial locations.

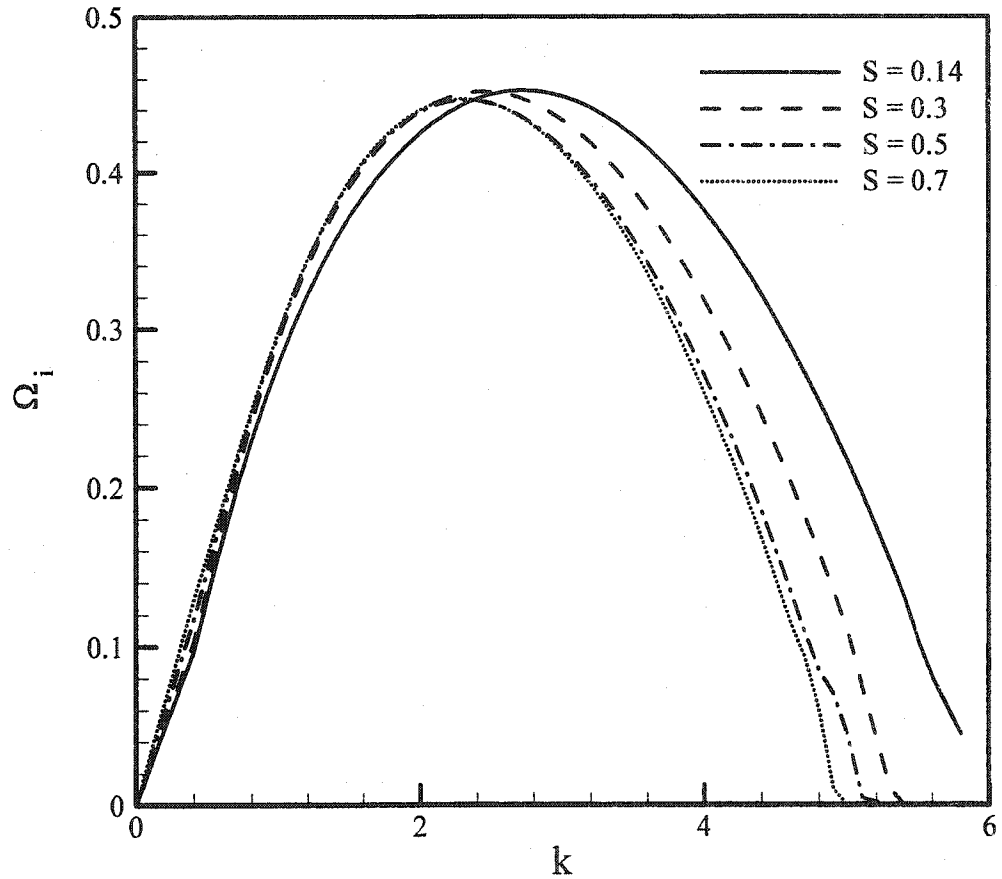


Figure 5.4: Variation of temporal growth rate Ω_i with the wavenumber k for different density ratios at z/2R=1, Ri = 0.01.

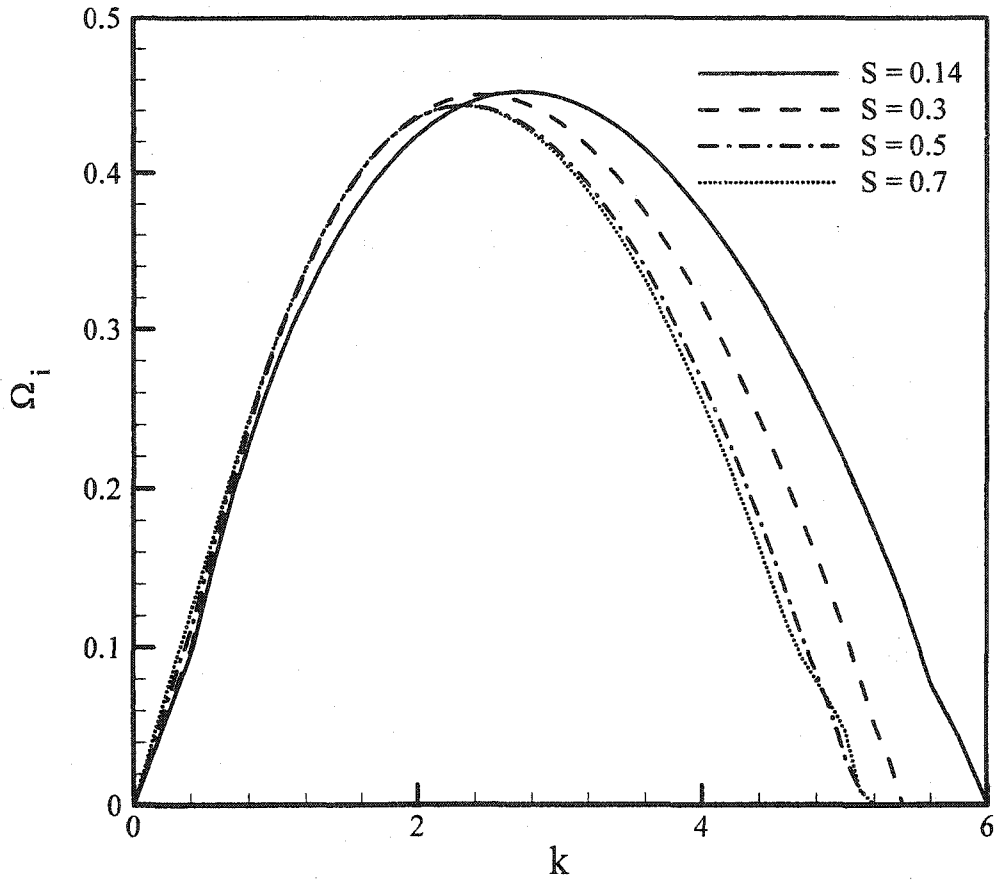


Figure 5.5: Variation of temporal growth rate Ω_i with the wavenumber k for different density ratios at z/2R=1, Ri = 0.0.

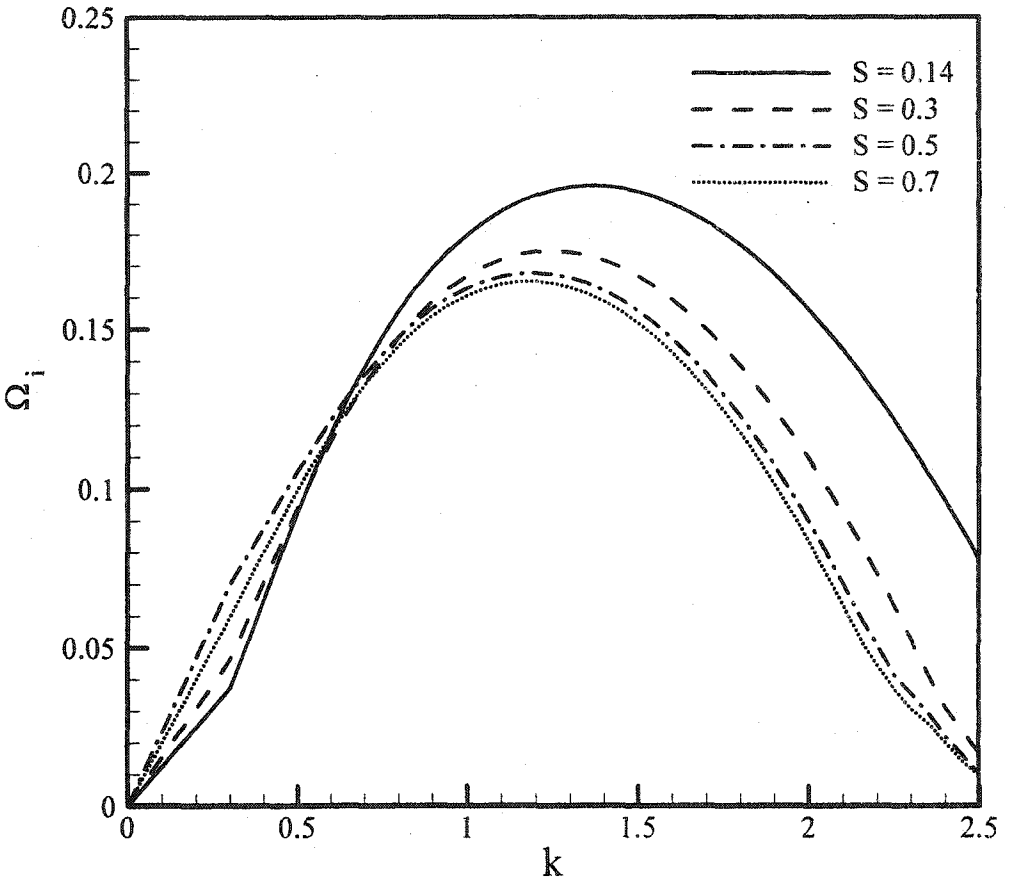


Figure 5.6: Variation of temporal growth rate Ω_i with the wavenumber k for different density ratios at z/2R=2.67, Ri = 0.01.

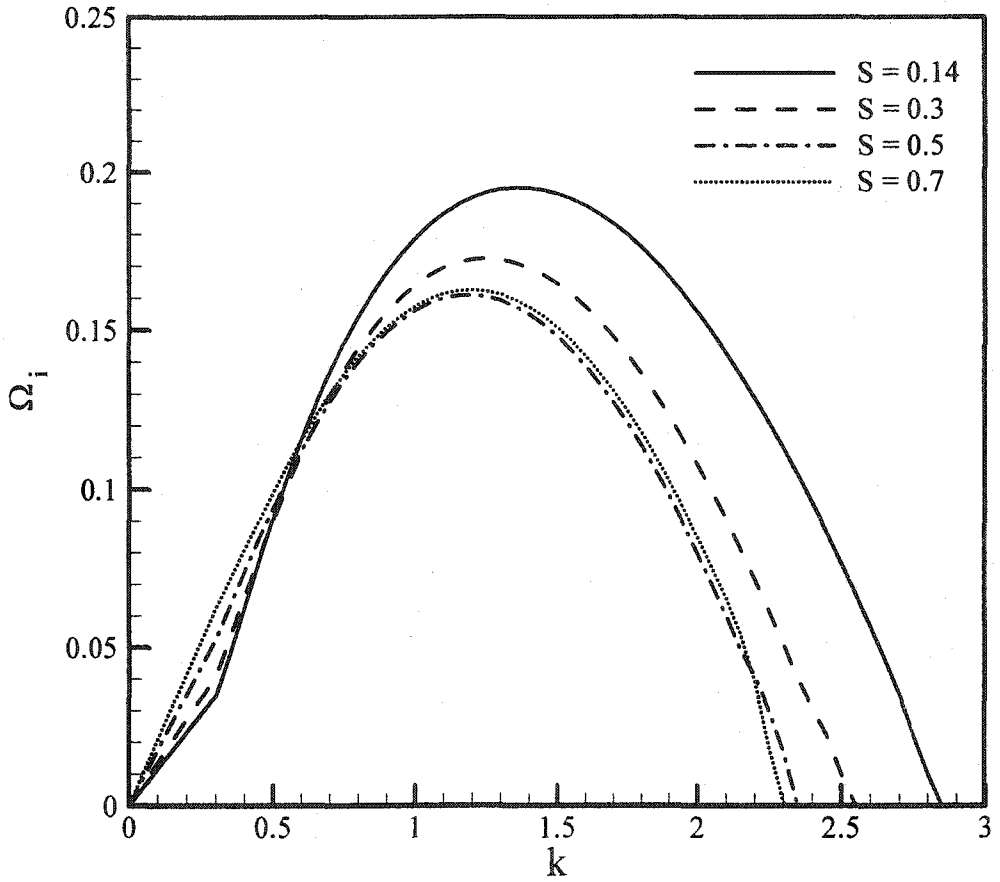


Figure 5.7: Variation of temporal growth rate Ω_i with the wavenumber k for different density ratios at z/2R=2.67, Ri = 0.0.

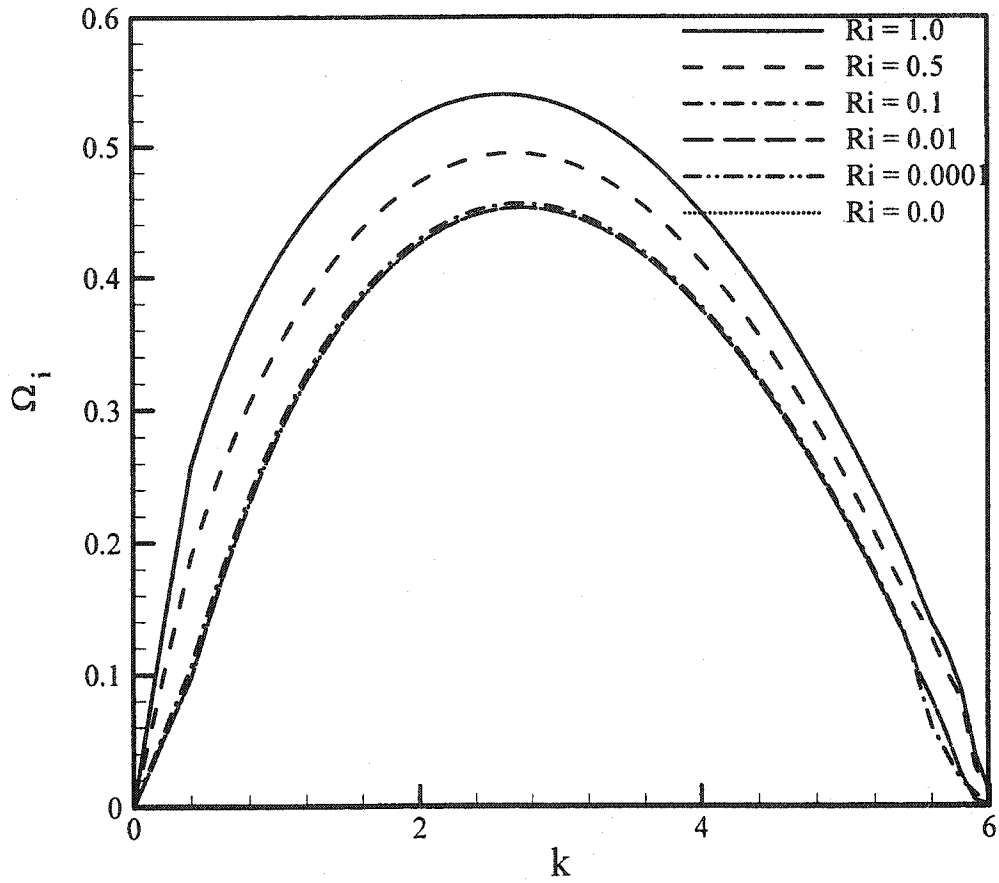


Figure 5.8: Variation of temporal growth rate Ω_i with the wavenumber k for different Ri at z/2R=1.0, S = 0.14.

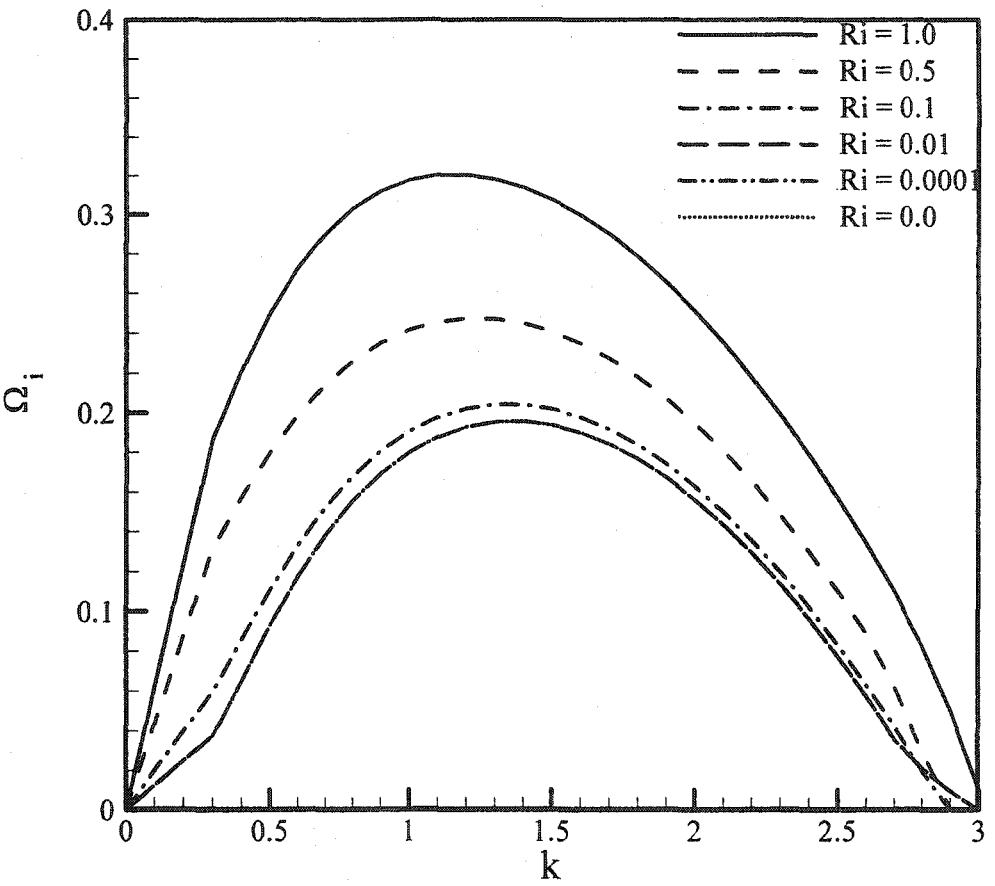


Figure 5.9: Variation of temporal growth rate Ω_i with the wavenumber k for different Ri at z/2R=2.67, S = 0.14.

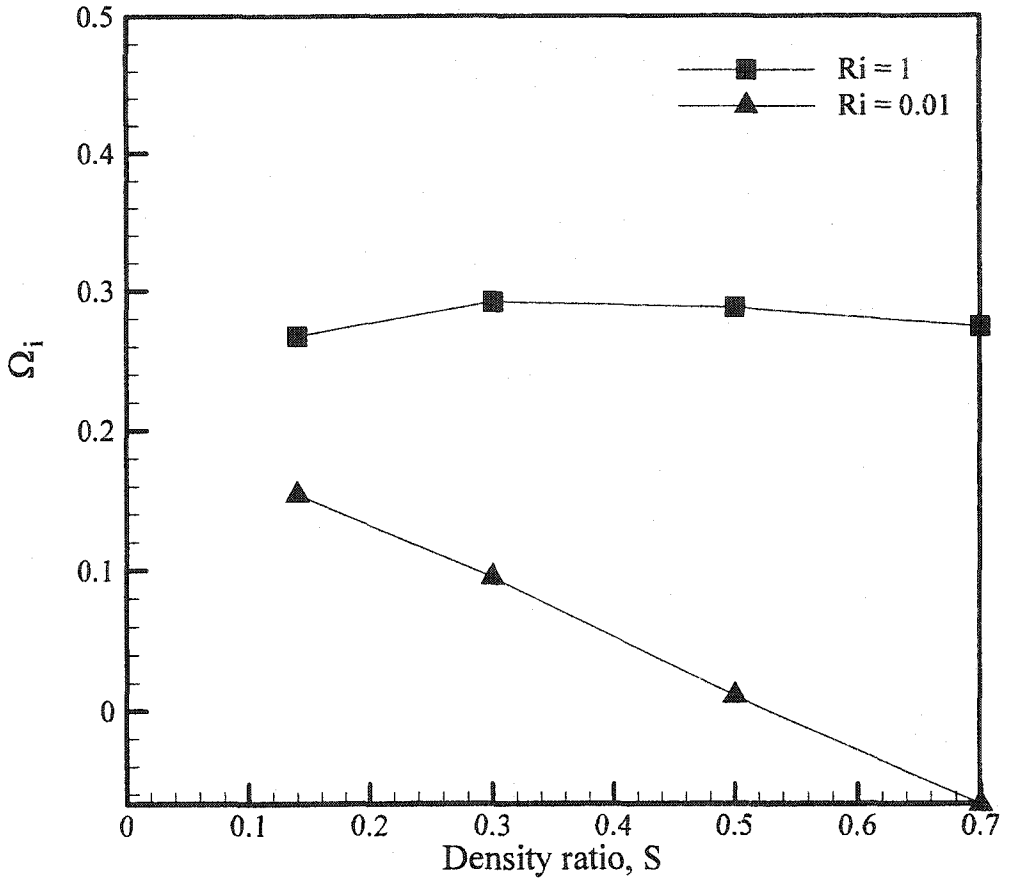


Figure 5.10: Variation of absolute temporal growth rate Ω_i with the density ratio for different Ri at z/2R=1.0.

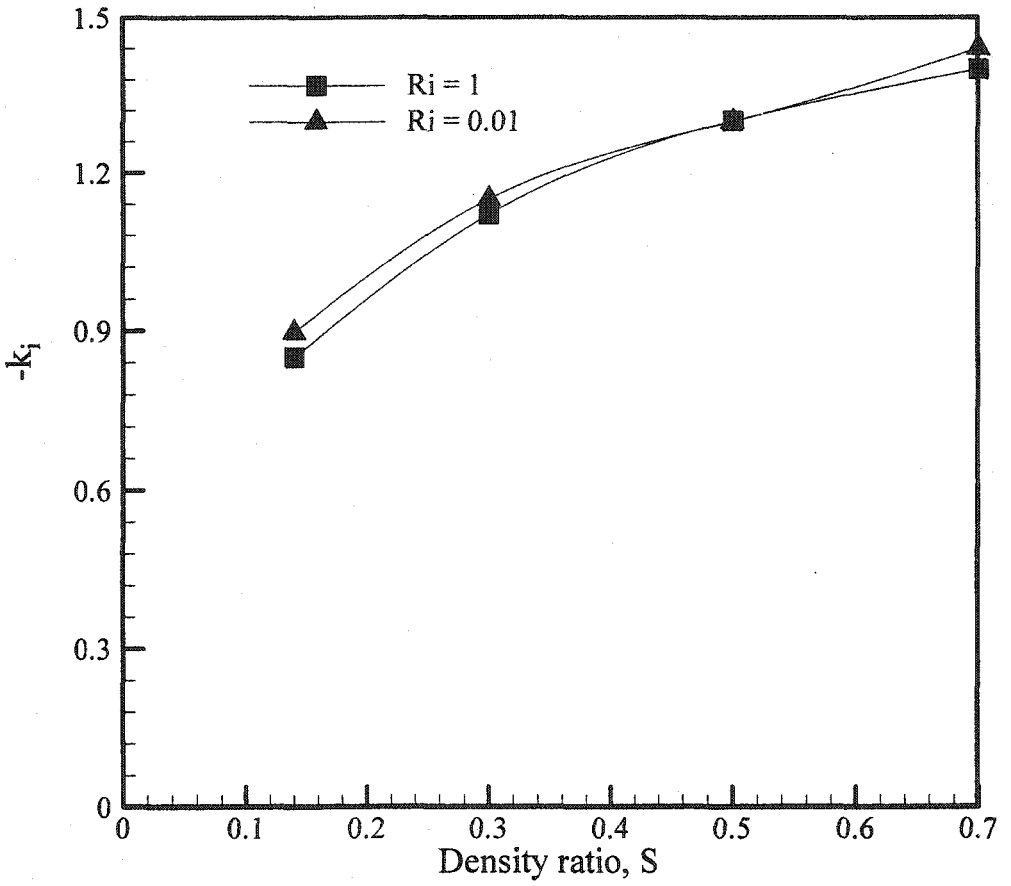


Figure 5.11: Variation of absolute spatial growth rate Ω_i with the density ratio for different Ri at z/2R=1.0.

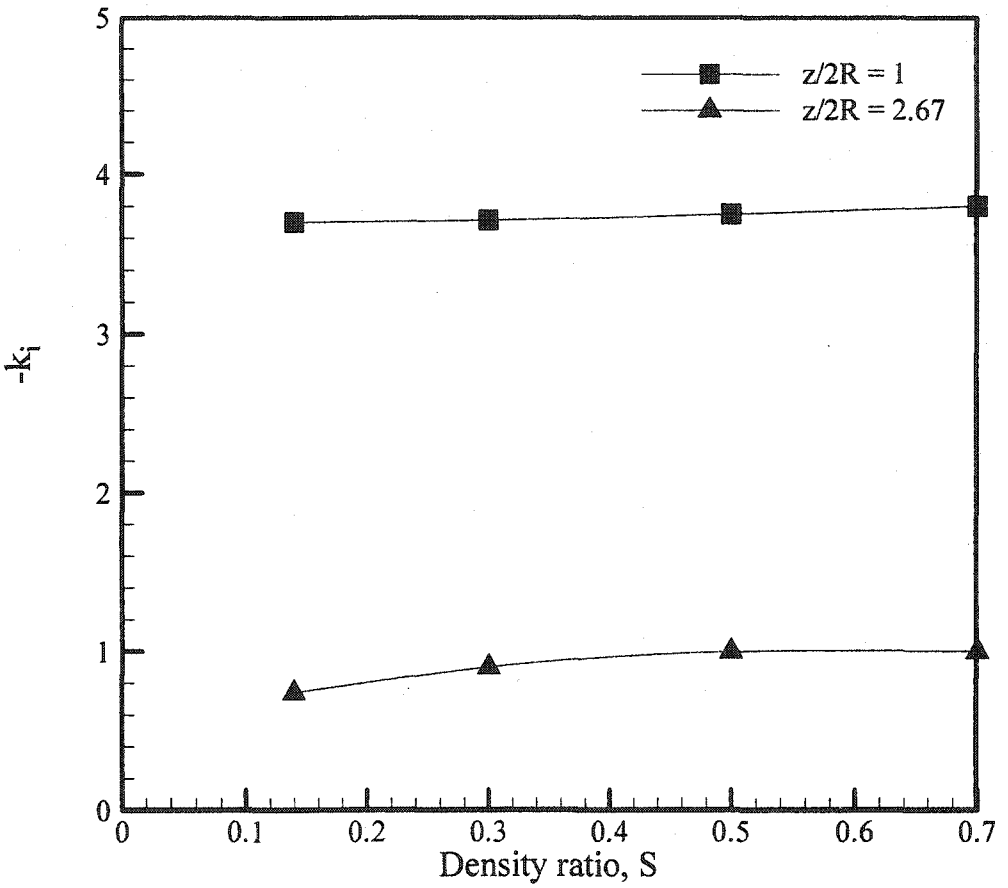


Figure 5.12: Variation of absolute spatial growth rate Ω_i with the density ratio for Ri = 0.0 at z/2R=1.0 and 2.67.

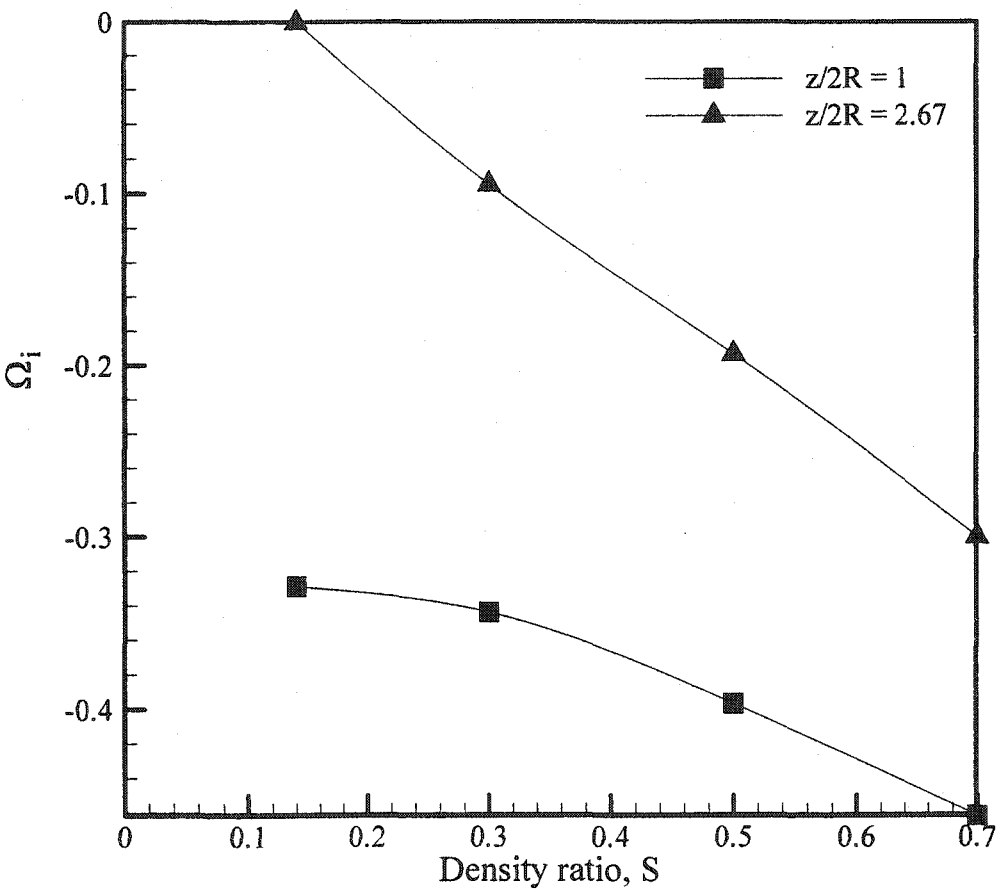


Figure 5.13: Variation of absolute temporal growth rate Ω_i with the density ratio for Ri = 0.0 at z/2R=1.0 and 2.67.

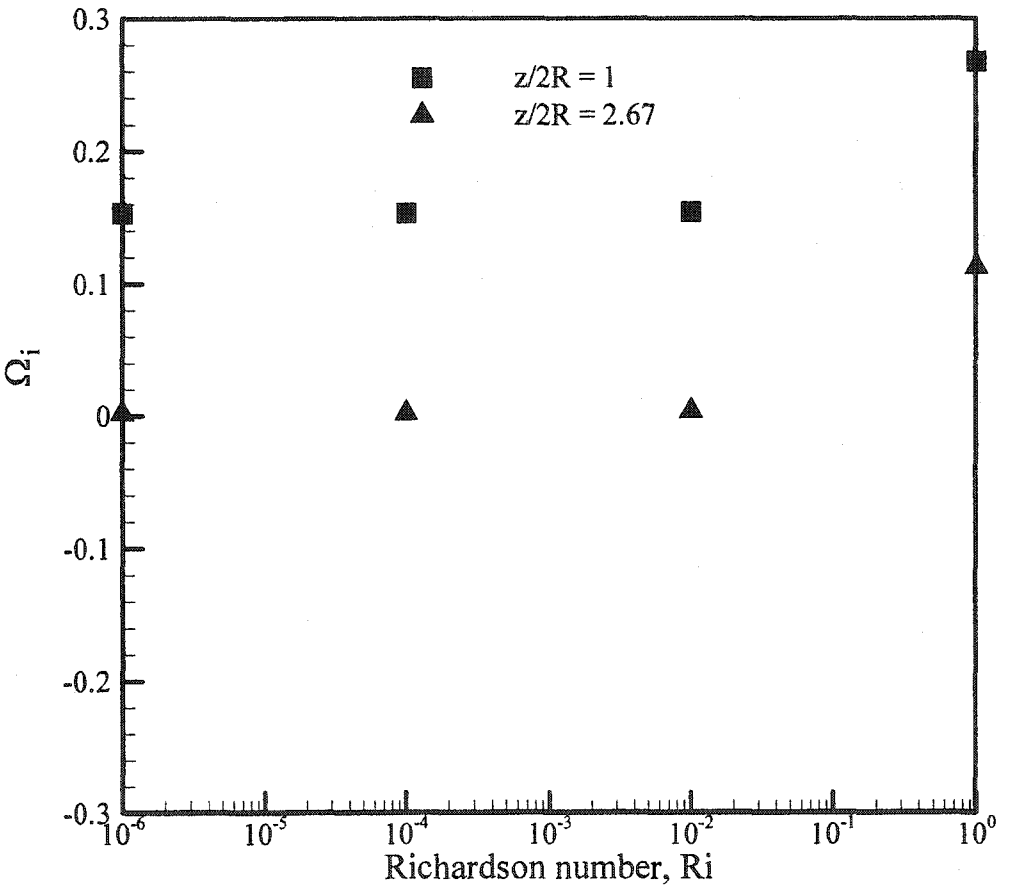


Figure 5.14: Variation of absolute temporal growth rate Ω_i with Ri for S = 0.14 at z/2R=1.0 and 2.67.

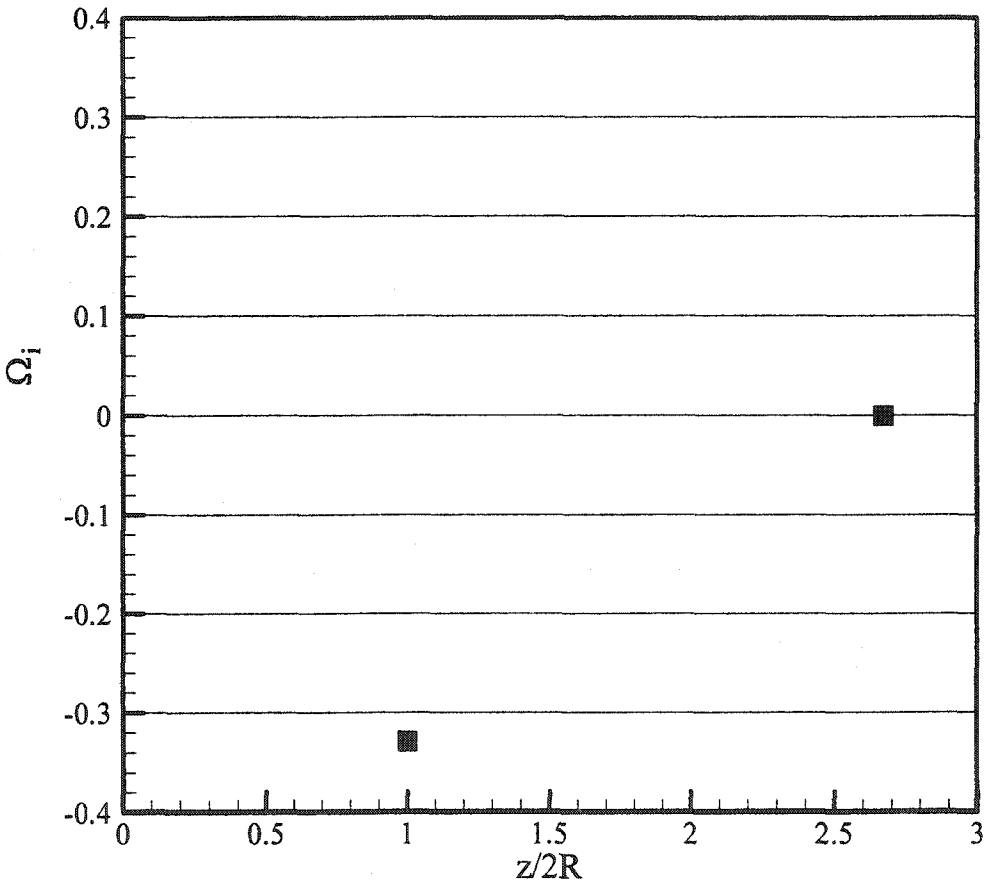


Figure 5.15: Variation of absolute temporal growth rate with axial location as Ri = 0, for S = 0.14 and at z/2R=1.0 and 2.67.

CHAPTER 6: CONCLUSIONS

Quantitative rainbow schlieren deflectometry technique was successfully applied to study the scalar flow structure of self-excited buoyant helium jets discharged vertically in air. The data were analyzed to identify the shape, structure, and evolutionary path of the high-vorticity entrainment region (referred to as the vortex), and to understand interactions between vortex and the oscillating flow field. Results show matching scalar structure inside the entrainment region as the vortex passed through the flow field. During the formative stage, the vortex accelerated and quickly grew in size. Peak oscillations occurred in the flow surrounding the vortex.

Quantitative RSD flow visualization and measurements in self-excited momentum-dominated helium jets in Earth gravity and microgravity have provided direct physical evidence of buoyancy effects on oscillation instability and jet flow structure. Time-resolved concentration measurements were obtained at temporal resolution of 1ms and spatial resolution of 0.2 mm for axial locations extending from tube exit to about 2.0d. FFT analysis of angular deflection data in Earth gravity revealed self-excited global oscillations. The oscillation amplitude decreased considerably in microgravity highlighting the buoyancy effects on the oscillating instability. Peak power variations along radial direction and at specific axial locations during the entire drop process revealed the gradual damping of oscillation amplitude in microgravity conditions in the momentum-dominated regime. The gradual damping of spectral power proved that the time required by the jet structure to adapt to removal of buoyancy forces and attain steady state conditions was more than the available 2.2s in drop tower. In the absence of

buoyancy, the jet transition length was extended indicating laminarization of the jet in microgravity.

Temporal and Spatio-temporal stability analyses were performed in low-density jets using non-parallel flow assumption. The effects of density ratio and buoyancy on the instability growth rates were determined. Temporal growth rates diminished with downstream progression and with decrease in Ri. Spatial growth rates remained unchanged with density ratio in the absence of buoyancy. Absolute instability was observed for all cases with finite Ri (as low as 0.0001). In the absence of buoyancy forces (at Ri = 0.0), the previously existing absolute instability disappeared at all locations establishing buoyancy as the primary instability mechanism in self-excited low-density jets.

CHAPTER 8: RECOMMENDATIONS

The current investigation on low-density jets needs further development in several areas. Some recommendations are listed below.

1. The analysis could be extended to time-averaged transitional and turbulent flows if the sampling time is sufficiently large.
2. The characteristics of the evolution of the low-density jet from the injector exit are relatively unknown. RSD could be effectively used to study the evolution process under a wide range of operating conditions.
3. Two-dimensional mapping would provide further insight into the vorticity dynamics of the flow structure.
4. The mean radial component of the velocity could be considered in linear stability analysis. To delineate individual constituent effects, swirl, viscosity and diffusion could be introduced separately to formulate the pressure disturbance equation. In addition, vorticity calculations could also be undertaken.
5. The CFD model could be extended to perform simulations in a variety of operating conditions. The geometry of the injector could be varied and a nozzle can be considered. Effect of lip angle and premixing on the evolution of the jet flow can be evaluated. Just as buoyancy can be removed, shear and diffusion could be removed and corresponding changes in oscillating flow could be evaluated.

REFERENCES

Agrawal, A.K., Albers, B.W., and Griffin, D.W. (1999) "Abel Inversion of Deflectometric Measurements in Dynamic Flows," *Applied Optics*, vol.38, pp. 3394-3398.

Al-Ammar, K., Agrawal, A. K., Gollahalli, S. R., and Griffin, D. (1998) "Application of Rainbow Schlieren Deflectometry for Concentration Measurements in an Axisymmetric Helium Jet," *Experiments in Fluids,* Vol. 25, pp. 89-95.

Al-Ammar, K. (1998). "Scalar Measurements and Analysis of Hydrogen Gas-Jet Diffusion Flames in Normal Gravity and Microgravity," Ph.D. Dissertation, University of Oklahoma.

Batchelor, G. K. and Gill, A. E. (1962) "Analysis of the Stability of Axisymmetric Jets," *Journal of Fluid Mechanics*, Vol. 14, pp. 529-551.

Becker, H.A. and Massaro, T.A. (1968) "Vortex Evolution in a Round Jet," *Journal of Fluid Mechanics*, Vol. 31, pp. 435-448.

Bers, A. (1975) "Linear Waves and Instabilities," *Plasma Physics*, edited by C. DeWitt and J. Peyraud, Gordon and Breach, New York, pp. 117-213.

Bers, A. (1983) "Space-time Evolution of Plasma Instabilities," *Handbook of Plasma Physics*, Vol. I, pp. 452-517.

Briggs, R. J. (1964) *Electron Stream Interaction with Plasmas*, MIT Press, Cambridge, Massachusetts.

Cetegen, B. M. and Kasper, K. D. (1996) "Experiments on the Oscillatory Behavior of Buoyant Plumes of Helium and Helium-Air Mixtures," *Physics of Fluids*, Vol. 8, No 11, pp. 2974-2984.

Cetegen, B. M. (1997) "Behavior of Naturally Unstable and Periodically Forced Axisymmetric Buoyant Plumes of Helium and Helium-Air Mixtures," *Physics of Fluids*, Vol. 9, No 12, pp. 3742-3752.

Crighton, D. G. and Gaster, M. (1976) "Stability of Slowly Diverging Jet Flow" *Journal of Fluid Mechanics*, Vol. 77, pp. 397-413.

Crow, S. C. (1972) "Acoustic Gain of a Turbulent Jet," *Paper IE6, Annual Meeting of the Division of Fluid Dynamics of the American Physics Society, Boulder, CO, Nov. 20-22, 1972.*

Crowe, S. C. and Champagne, F. H. (1971) "Orderly Structure in Jet Turbulence," *Journal of Fluid Mechanics*, Vol. 48, pp. 547-591.

Dasch, C.O. (1992). "One-Dimensional Tomography:A Comparison of Abel, Onion-peeling, and Filtered Backprojection methods," *Applied Optics*, vol. 31, pp. 1146-1152.

Ffowcs-Williams, J. E. and Kempton, A. J. (1978) "The Noise from the Large-Scale Structure of a Jet," *Journal of Fluid Mechanics*, Vol. 84, Pt. 4, pp. 673-694.

Goldstein, R. J., and Kuehn, T. H. (1996) "Optical systems for flow measurement: shadowgraph, schlieren, and Interferometric techniques." *Fluid mechanics measurements*, Chapter 7, Taylor and Francis, Washington DC, 451-502.

Gouldin, F.C., Schefer, R.W., Johnson, S.C., and Kollmann, W. (1986) "Nonreacting turbulent mixing flows," Prog. Energy Combust. Sci. **12**, 257.

Greenberg, P.S., Klimek, R.B. and Buchele, D.R.(1995). "Quantitative Rainbow Schlieren Deflectometry," *Applied Optics,* vol. 34, pp. 3819-3822.

Hamins, A., Yang, J.C., and Kashiwagi, T. (1992). "An Experimental Investigation of Pulsation Frequency of Flames," *Twenty-Fourth Symposium (International) on Combustion,* The Combustion Institute, pp. 1695-1702.

Jendoubi, S. and Strykowski, P.J. (1994) "Absolute and Convective Instability of Axisymmetric Jets with External Flow," *Physics of Fluids*, Vol. 6, No. 9, pp. 3000-3009.

Kyle, D. M. and Sreenivasan, K. R. (1993) "The Instability and Breakdown of a Round Variable-Density Jet," *Journal of Fluid Mechanics*, Vol. 249, pp. 619-664.

Laskey. K. J., Ellzey, J. L., and Oran, E. S., (1989) "A numerical study of unsteady diffusion flame," *27thAerospace Sciences Meeting*, AIAA-89-0572, Reno, NV.

Lawson, A.L. (2001) "Instability Analysis of a Low-Density Gas Jet Injected into a High-Density Gas," *PhD Dissertation*, School of Aerospace and Mechanical Engineering, University of Oklahoma, Norman, OK.

Leptuch, P. (2002) "A Quantitative Rainbow Schlieren Deflectometry Analysis of the Characteristics of Helium Jets Flowing into Air upon Removal of Gravitational Forcing," *Masters Thesis*, School of Aerospace and Mechanical Engineering, University of Oklahoma, Norman, OK.

Li, X. and Shen, J. (1996) "Breakup of Cylindrical Liquid Jets in Co-Flowing Gas Streams," *ASME*, pp. 22-31.

Mell, W. E., McGrattan, W. B., Baum, H. R., (1996) "Numerical simulation of combustion in fire plumes," *Proceedings of Combustion Institute*, Vol. 26, pp. 1523-1530.

Michalke, A. (1971) "English Translation: Instability of Compressible Circular Free Jet with Consideration of the Influence of the Jet Boundary Layer Thickness," *N.A.S.A. Tech. Memo*. 75190.

Michalke, A. (1984) "Survey on Jet Instability Theory," *Progress in Aerospace Sciences*, Vol. 21, pp. 159-199.

Michalke, A. and Hermann, G. (1982) "On the Inviscid Instability of a Circular Jet with External Flow," *Journal of Fluid Mechanics*, Vol. 114, pp. 343-359.

Monkewitz, P. A., Bechert, D. W., Barsikow, B. and Lehmann, B. (1990) "Self-excited Oscillations and Mixing in a Heated Round Jet," *Journal of Fluid Mechanics*, Vol. 213, pp. 611-639.

Monkewitz, P. A. and Sohn, K. D. (1988) "Absolute Instability in Hot Jets," *AIAA Journal*, Vol. 26, pp. 911-916.

Moore, C. J. (1977) "The Role of Shear-Layer Instability Waves in Jet Exhaust Noise," *Journal of Fluid Mechanics*, Vol. 80, Pt. 2, pp. 321-367.

Murray, J. D., and VanRyper, W. (1994) *encyclopedia of Graphic File Formats* O'Reilly & Associates, Inc., Sebatopol, CA.

Panchapakesan, N.R., and Lumley, J.L. (1993) "Turbulence measurements in axisymmetric jets of air and helium. Part 2. Helium jet," *Journal of Fluid Mechanics*, Vol 246, 225.

Pasumarthi, K. S. (2000) "Full Field Scalar Measurements in a Pulsating Helium Jet Using Rainbow Schlieren Deflectometry," *MS Thesis,* University of Oklahoma, Norman, Oklahoma.

Raynal, L., Harion, J.L., Favre-Marinet, M. and Binder, G. (1996) "The Oscillatory Instability of Plane Variable-Density Jets," *Physics of Fluids*, Vol. 8, No. 4, pp. 993-1006.

Richards, C.D., Breuel, B.D., Clark, R.P., and Troutt, T.R. (1995). "Concentration Measurements in a Self-Excited Jet," *Experiments in Fluids*, Vol. 21, pp. 103-109.

Rubinstein, R., and Greenberg, P. S. (1994) "Rapid inversion of angular deflection data for certain axisymmetric refractive index distributions." *Applied Optics,* Vol. 33, pp.1141-1144.

Sreenivasan, K.R., Raghu, S., and Kyle, D. (1989). "Absolute Instability in Variable Density Round Jets," *Experiments in Fluids*, vol. 7, pp. 309-317.

Schmid, P.J. and Henningson, D.S. (2001) "Stability and Transition in Shear Flows," *Applied Mathematical Sciences*, Vol. 142, *Springer-Verlag*, New York.

Sohn, K. D. (1986) "Absolute Instability in Hot Jets," *MS Thesis*, University of California, Los Angeles.

Soteriou, M. C., Dong, Y., Cetegen, B. M., (2002) "Lagrangian simulation of the unsteady near field dynamics of planar buoyant plumes," *Phys. Fluids*, Vol. 14, pp. 3118-3140.

Subbarao, E. R. and Cantwell, B. J. (1992) "Investigation of a Co-Flowing Buoyant Jet: Experiments on the Effects of Reynolds Number and Richardson Number," *Journal of Fluid Mechanics*, Vol. 245, pp. 69-90.

Teukolsky, S. A., Vetterling, W. T., and Flannery, B. P. (1992) *Numerical Recipies in Fortran*, 2nd Edition, Cambridge University press, New York, NY.

Vedantam N. K. (2003) "Effect of Mean Flow Profiles on Instability of a Low-Density Jet Injected Into a High-Density Gas," *Masters Thesis*, School of Aerospace and Mechanical Engineering, University of Oklahoma, Norman, OK.

Yates, L. a. (1993) "Constructed Interferograms, Schlieren and Shadowgraph: A User's Manual," NASA-CR=194530.

Yep, T. W, Agrawal, A. K, and Griffin, D. V. (2003) "Gravitational Effects on Near-Field Flow Structure of Low-Density Gas Jets," *AIAA Journal*, Vol. 41, No. 10, pp 1973-1979.

Yildrim, B. S, and Agrawal, A. K, (2004) "Full Field Measurements of self-excited oscillations in momentum-dominated helium jets," *Exp. Fluids*, in review.

Yu, M.H. and Monkewitz, P. A. (1990) "The Effect of NonUniform Density on the Absolute Instability of Two-Dimensional Inertial Jets and Wakes," *Physics of Fluids A*, Vol. 2, No. 7, pp. 1175-1181.

APPENDIX A

EXPERIMENTAL DATA

Kinematic viscosity of helium, $\upsilon = 122 \times 10^{-6}\ m^2/s.$

Binary diffusion coefficient of helium in air, $D_b = 7.44 \times 10^{-6}\ m^2/s.$

Density of helium gas, $\rho_j = 0.1625\ Kg/m^3$ at 300K.

Density of surrounding air, $\rho_\infty = 1.1025\ Kg/m^3$ at 300K.

Dale-Gladstone Constants

Helium, $\kappa_{He} = 201 \times 10^{-6}$

Oxygen, $\kappa_{O2} = 193 \times 10^{-6}$

Nitrogen, $\kappa_{N2} = 237 \times 10^{-6}$

APPENDIX B

UNCERTAINTY ANALYSIS

Background Hue of a rainbow schlieren image $H_b = 30$

For a given hue value H,

Calculate the transverse displacement from the filter calibration curve

$D_i = y(H) - y(H_b)$

Where y(H) = projected location at given hue value

$y(H_b)$ = projected location at background hue

$\delta y(H_b) = 0$ (assumed)

$\delta y(H) = \delta y(H + \sigma(H)) - \delta y(H)$

where $\sigma(H)$ is the standard deviation corresponding to that projected location, obtained from the filter calibration curve.

Focal length, f = 1000mm

ωf_c = 0mm

Calculate deflection angle

Deflection angle, $\varepsilon = \frac{D_i}{f}$

$$\varepsilon = \frac{y(H) - y(H_b)}{f}$$

Uncertainty in deflection angle

$$\omega\varepsilon = \sqrt{\left(\omega D_i \frac{1}{f_c}\right)^2}$$

Calculate refractive index difference

$$\delta_i = \sum_{j=1}^{N} D_{(i,j)} \varepsilon_j$$

Uncertainty in refractive index

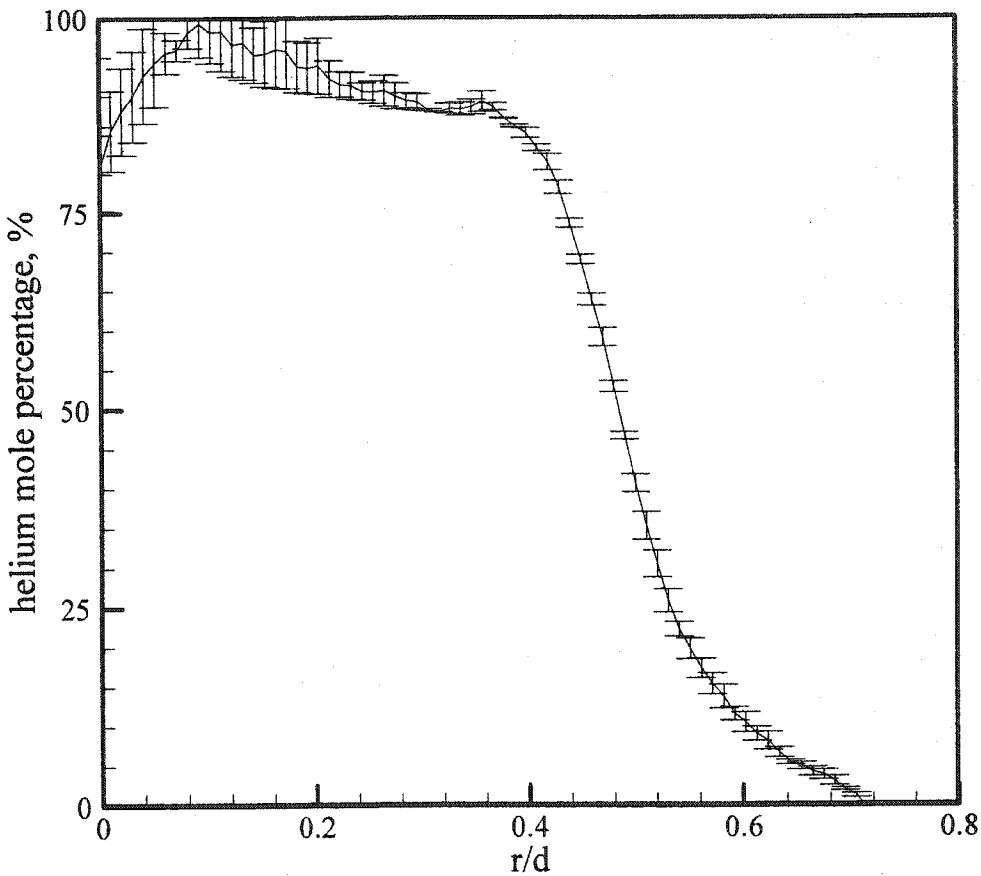
$$\omega\delta_i = \sqrt{\left(\sum_{j=1}^{N} D_{(i,j)} \omega\varepsilon_j \right)^2}$$

Calculate helium mole fraction

$$X_{He} = \frac{\frac{\bar{R} \cdot T}{P} \cdot \delta - \kappa_{N_2} X_{N_2} M_{N_2} - \kappa_{O_2} X_{O_2} M_{O_2}}{\kappa_{He} M_{He}}$$

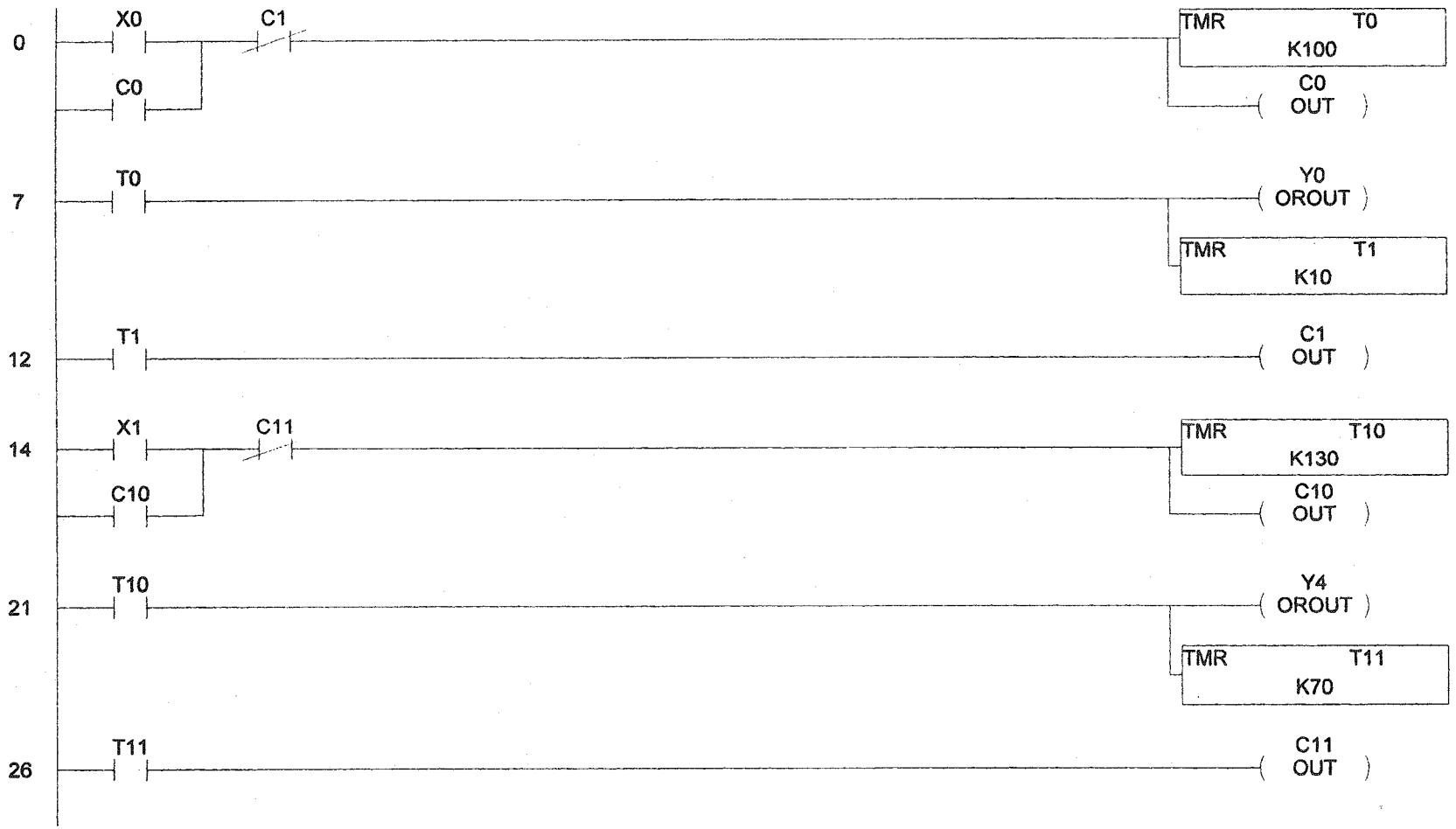
Calculate uncertainty in helium mole fraction

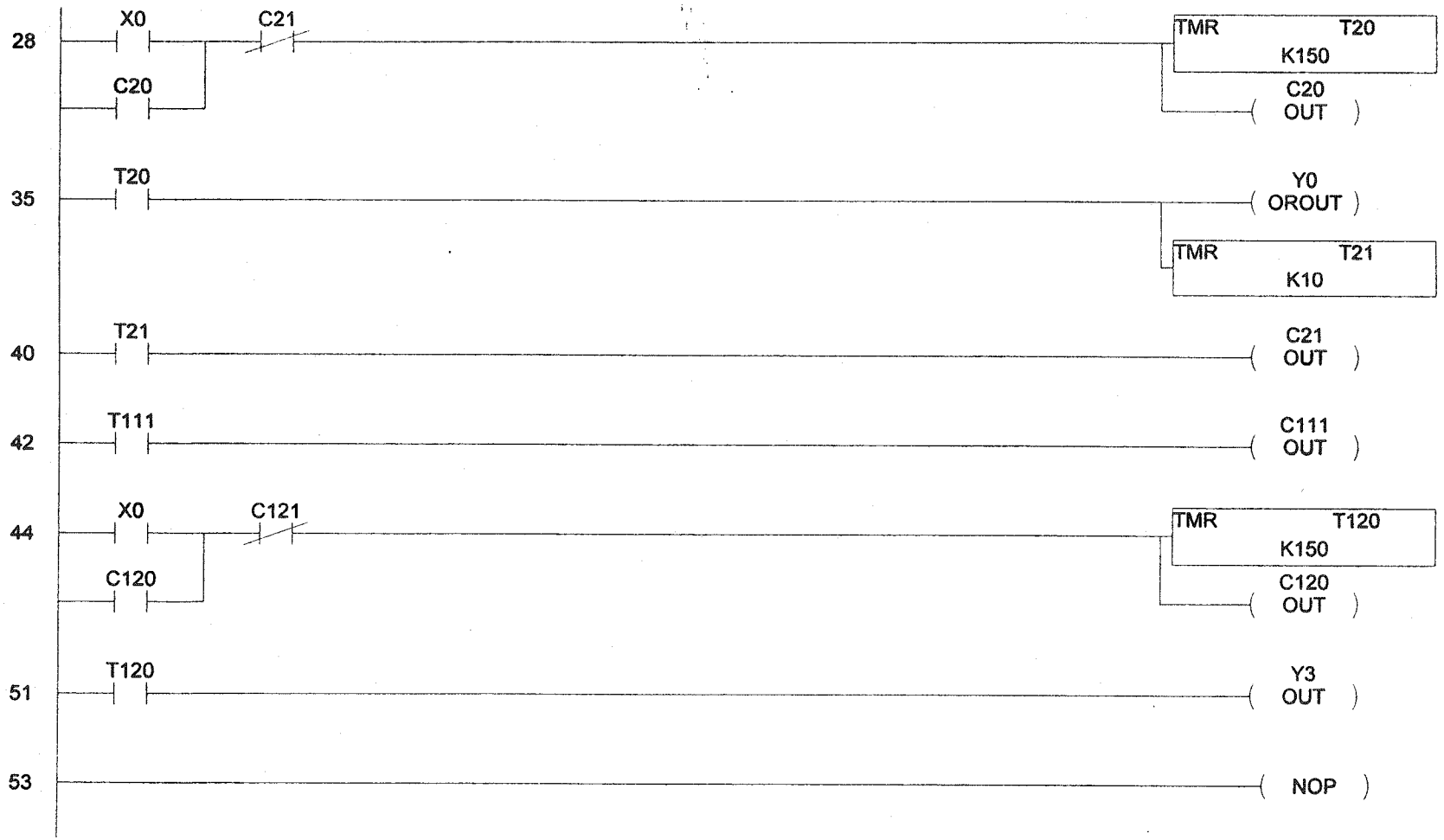
$$\omega X_{He} = \frac{\bar{R} \cdot T}{P \cdot \kappa_{He} \cdot M_{He}} \cdot \omega\delta$$

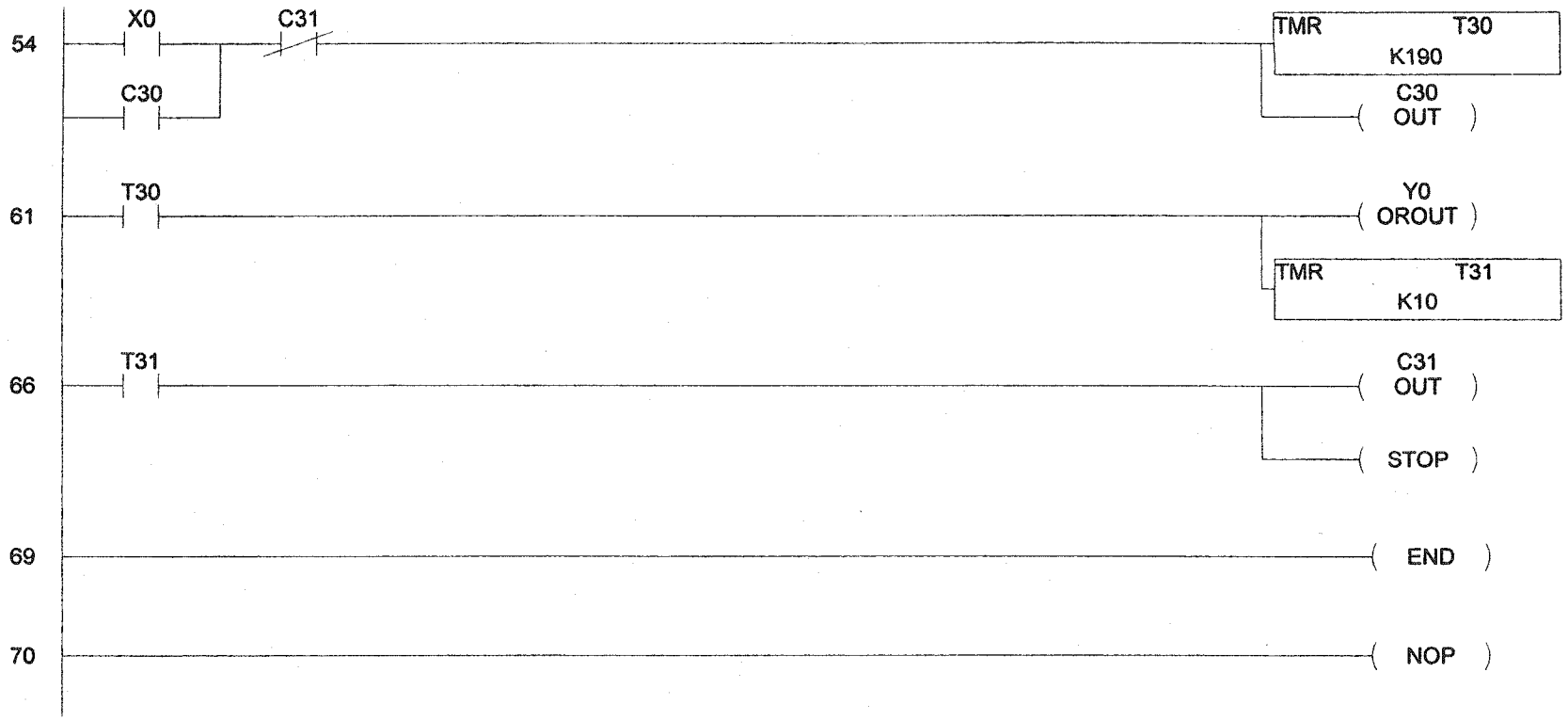

100
75
50
25
0
helium mole percentage, %
0
0.2
0.4
0.6
0.8
r/d

APPENDIX C

PLC LADDER LOGIC PROGRAM


0
X0
C1
C0
TMR T0
K100
C0
OUT
7
T0
Y0
OROUT
TMR T1
K10
12
T1
C1
OUT
14
X1
C11
C10
TMR T10
K130
C10
OUT
21
T10
Y4
OROUT
TMR T11
K70
26
T11
C11
OUT


28
X0
C21
C20
TMR T20
K150
C20
OUT
35
T20
Y0
OROUT
TMR T21
K10
40
T21
C21
OUT
42
T111
C111
OUT
44
X0
C121
C120
TMR T120
K150
C120
OUT
51
T120
Y3
OUT
53
NOP


54
X0
C31
C30
TMR T30
K190
C30
OUT
61
T30
Y0
OROUT
TMR T31
K10
66
T31
C31
OUT
STOP
69
END
70
NOP